Ida Saxrud

The Effect of Noble Metal Promoters on Hydrotalcite-Based Nickel-Cobalt Catalysts for Syngas Conditioning for Advanced Biofuels

Master's thesis in Sustainable Chemistry and Biochemical Engineering
Supervisor: Edd A. Blekkan
Co-supervisor: Ask Lysne

May 2023

NTNU
Norwegian University of
Science and Technology

Ida Saxrud

The Effect of Noble Metal Promoters on Hydrotalcite-Based Nickel-Cobalt Catalysts for Syngas Conditioning for Advanced Biofuels

Master's thesis in Sustainable Chemistry and Biochemical Engineering
Supervisor: Edd A. Blekkan
Co-supervisor: Ask Lysne
May 2023

Norwegian University of Science and Technology
Faculty of Natural Sciences
Department of Chemical Engineering

NTNU
Norwegian University of
Science and Technology

Preface

This thesis presents the work completed as a part of the course TKP4901 - Chemical Process Technology, Master's Thesis writen for the Catalysis group in the Department of Chemical Engineering at the Norwegian University of Science and Technology.

I would like to thank my supervisor Professor Edd A. Blekkan for his guidance and support. A spesial thanks is given to co-supervior Ph.D candidate Ask Lysne for his guidance, mentoring and for making himself available for questions on short notice. I also want to thank Estelle Marie M. Vanhaecke for instrument training and helping with problems in the instrument lab. The support of the Norwegian Micro- and Nano-Fabrication Facility, NorFab (no. 295864), and SINTEF is also acknowledged.

Finally, I would like to thank my family and friends, for their unconditional support throughout my time as a master student at NTNU.

Declaration of Compliance

I, Ida Saxrud, declare that this is an independent work according to the exam regulations of the Norwegian University of Science and Technology.

<div align="right">Trondheim, Norway May 29, 2023</div>

Ida Saxrud

Ida Saxrud

Abstract

Converting biomass to fuel with gasification and Fischer-Tropsch hydrocarbon synthesis is a prominent and sustainable alternative to fuel production from fossil sources. However, the generation of tars during the gasification process poses a significant challenge. Gas conditioning techniques are employed to convert tars into syngas components suitable for Fischer-Tropsch synthesis. This thesis aims to enhance the gas conditioning process by synthesizing a series of noble metal-promoted Ni-Co catalysts derived from hydrotalcite-like materials, mainly focusing on steam reforming. The base catalyst composed of 20-20 wt% Ni-Co on hydrotalcite-like support was synthesized through co-precipitation, while noble metal promotions (1.0 wt% Pt, Pd, and Rh) were achieved via incipient wetness impregnation. The physicochemical properties of the catalysts were evaluated using techniques such as N_2 physisorption, H_2 chemisorption, temperature programmed reduction, X-ray diffraction, and inductively coupled plasma mass spectrometry. Subsequently, steam reforming experiments were conducted on the noble metal promoted catalysts, both with and without a tar model consisting of 75% toluene and 25% 1-methylnaphthalene, and compared with the unpromoted catalyst. The catalysts' surfaces were analyzed after steam reforming to identify deactivation mechanisms using scanning electron microscopy (SEM) and energy dispersive X-ray spectroscopy (EDS).

Characterization results revealed increased surface area and dispersion with noble metal promotion, accompanied by a shift towards lower temperatures in reduction profiles. The steam reforming experiments in the absence of the tar model exhibited minor deactivation, while the 1.0 wt% rhodium promoted catalyst exhibited high activity. The platinum and palladium-promoted catalysts displayed slight improvements in catalytic activity compared to the unpromoted catalyst. The introduction of the tar model during steam reforming experiments substantially impacted the catalysts' activity, selectivity, and stability. The presence of the tar model led to reduced activity and catalyst deactivation due to tar adsorption on active sites and coke formation. The main observed deactivation mechanism was attributed to the encapsulating carbon, as evidenced by the absence of sintered particles and the diameter of carbon filaments observed in the scanning electron microscopy and energy-dispersive X-ray spectroscopy analysis.

Furthermore, a SEM and EDS analysis was conducted on unpromoted 20-20 wt% Ni-Co catalysts derived from hydrotalcite-like precursors operated under different conditions during steam reforming experiments with toluene as the tar model. The objective of the analysis was to provide information on the deactivation mechanisms present, determine Ni-Co particle size, and estimate carbon filament diameters.

Continued investigations are needed to confirm which deactivation mechanisms are present in the catalysts precisely. The 1.0 wt% Rh 20-20 wt% Ni-Co catalyst exhibited high initial activity but rapid deactivation in the presence of the tar model, making it suitable for steam reforming with in situ regeneration.

Sammendrag

Konvertering av biomasse til drivstoff ved hjelp av gassifisering og Fischer-Tropsch hydrokarbonsyntese er et fremtredende og bærekraftig alternativ til drivstoffproduksjon fra fossile kilder. Imidlertid utgjør dannelse av tjære under gassifiseringsprosessen en betydelig utfordring. Gasskondisjoneringsteknikker benyttes for å omdanne tjære til syngaskomponenter som egner seg for Fischer-Tropsch syntese. Denne avhandlingen har som mål å forbedre gasskondisjoneringsprosessen ved å syntetisere en serie edelmetall-promoterte Ni-Co-katalysatorer derivert fra hydrotalkittlignende materialer, med spesiell vekt på dampreformering. Basiskatalysatoren bestående av 20-20 vekt% Ni-Co på en hydrotalkittlignende støtte ble syntetisert ved samutfelling, mens edelmetallpromoteringene (1.0 vekt% Pt, Pd, og Rh) ble oppnådd ved «insipient wettness impregiation». De fysikalske og kjemiske egenskapene til katalysatorene ble evaluert ved bruk av teknikker som N_2-fysisorpsjon, H_2-kjemisorpsjon, temperaturprogrammert reduksjon, røntgendiffraksjon og induktivt koblet plasma massespektrometri. Deretter ble dampreformeringseksperimenter utført på de edelmetall-promoterte katalysatorene, både med og uten en tjæremodell bestående av 75% toluen og 25% 1-metyl-naftalen, og sammenlignet med den upromoterte katalysatoren. Overflatene til katalysatorene ble analysert etter dampreformering for å identifisere deaktiveringsmekanismer ved hjelp av skannende elektronmikroskopi (SEM) og energidispersiv røntgenspektroskopi (EDS).

Karakteriseringsresultatene viste økning i overflateareal og spredning med edelmetall-promotering, i tillegg til en forskyvning mot lavere temperaturer i reduksjonsprofilene. Dampreformeringseksperimentene uten tjæremodellen viste mindre deaktivering, mens den 1.0 vekt% rhodiumpromoterte katalysatoren viste høy aktivitet. Platina- og palladiumpromoterte katalysatorer viste en svak forbedring i katalytisk aktivitet sammenlignet med den upromoterte katalysatoren. Innføringen av tjæremodellen under dampreformeringseksperimentene hadde en betydelig innvirkning på katalysatorenes aktivitet, selektivitet og stabilitet. Tilstedeværelsen av tjæremodellen førte til redusert aktivitet og deaktivering av katalysatoren på grunn av tjæreabsorpsjon på aktive områder og dannelse av koks. Den viktigste observerte deaktiveringsmekanismen ble tildelt innkapsulerende karbon, som ble påvist gjennom fravær av sinterpartikler og diameteren på karbon filamentene som ble observert i analysen ved skannende elektronmikroskopi og energidispersiv røntgenspektroskopi.

Videre ble det utført en SEM- og EDS-analyse på de upromoterte 20-20 vekt% Ni-Co-katalysatorene derivert fra hydrotalkittlignende forløpere, som ble testet under ulike forhold i dampreformerings-eksperimenter med toluen som tjæremodell. Målet med analysen var å finne informasjon om deaktiveringsmekanismer som er til stede i katalysatorene, bestemme Ni-Co-partikkelstørrelse og estimere diameteren på karbon filamentene.

Det er behov for ytterligere undersøkelser for å bekrefte hvilke deaktiveringsmekanismer som er til stede i katalysatorene. Den 1.0 vekt% Rh 20-20 vekt% Ni-Co-katalysatoren viste høy innledende aktivitet, men rask deaktivering når tjæremodellen ble brukt, noe som gjør den egnet for dampreformering med in situ-regenerering.

Table of Contents

List of Tables

List of Figures

Abbreviations

Abbreviation	Description
BET	Brunauer, Emmett and Teller
BJH	Barrett, Joyner and Halenda
BtL	Biomass to Liquid
EDS	Energy Dispersive X-ray Spectroscopy
FID	Flame Ionization detector
FT	Fischer-Tropsch
GC	Gas Chromatography
GHSV	Gas Hourly Space Velocity
HT	Hydrotalcite
ICP-MS	Inductively Coupled Plasma Mass Spectroscopy
MFC	Mass Flow Controller
MS	Mass Spectrometry
SEM	Scanning Electron Microscope
SMR	Steam Methane Reforming
STEM	Scanning Transmission Electron Microscope
STY	Site Time Yield
TCD	Thermal Conductivity Detector
TGA	Thermo Gravimetric Analysis
TOF	Turnover Frequency
TPO	Temperature Programmed Oxidation
TPR	Temperature Programmed Reduction
WGS	Water Gas Shift
XRD	X-ray Diffraction

1

Introduction

The increasing energy demand and greenhouse gas emissions have resulted in a pressing need for sustainable energy sources to mitigate climate challenges. To address this, several international agreements and treaties have been established, including the UN Framework Convention on Climate Change (UNFCCC) in 1992, which was the first agreement explicitly (specifically aimed at) addressing climate change [30]. The Kyoto Protocol, adopted in 1997, obligated developed countries to reduce their greenhouse gas emissions, while the Paris Agreement, signed in 2015, aims to limit global warming to well below 2 °C above pre-industrial levels by reducing greenhouse gas emissions and fostering climate-resilient development. These agreements and treaties have played a crucial role in setting international climate goals and promoting sustainable energy development. To meet these treaties, sustainable energy sources such as solar, wind, hydroelectric, and geothermal energy have been developed rapidly to meet the growing populations' energy demands. However, the energy demand still surpasses the advancements in sustainable energy sources.

Solar, wind, hydroelectric and geothermal energy are primary sources of renewable energy that can be converted into electric energy. These sources have several advantages over fossil fuels, including their abundance and renewability. They also have the added benefit of producing little to no greenhouse gas emissions during energy production, reducing their environmental impact. However, one challenge with using electric energy for transportation is the lower energy density of electricity compared to liquid fuels such as gasoline and diesel. Electric vehicles require larger and heavier batteries to achieve similar ranges than vehicles fueled by liquid fuels, which can limit their practicality for long-distance transport, shipping, and aviation.

The transportation sector is a major contributor to global carbon dioxide emissions, accounting for 37% of end-use sector emissions in 2021 [63]. The transportation industry's use of high energy-density fossil fuels, such as gasoline and diesel, significantly contributes to these emissions. To mitigate the impact of transportation emissions on the environment, there is a growing need to transition towards alternative and renewable fuels.

Biofuels produced from biomass have emerged as a promising alternative, offering several advantages over traditional fossil fuels.

Biofuels are renewable and sustainable energy sources that can be produced from a wide range of feedstocks, including crops, waste materials, and algae. They are considered carbon-neutral, as the CO_2 emitted during their combustion is offset by the CO_2 absorbed by the crops during their growth. They have a higher energy density than electricity, making them a more practical option for long-distance transport, shipping, and aviation. Furthermore, biofuels can be used in existing machinery without significant modification to be easily integrated into the existing transportation infrastructure. The urgent need to address climate change and reduce greenhouse gas emissions has led to a new era of renewable energy sources, and biofuels play an increasingly important role in this transition.

Biofuels, also known as synthetic fuels, are an attractive alternative to traditional fossil fuels, as they offer a renewable and sustainable energy source. These fuels can be produced through various methods, including natural gas reforming, coal gasification, or the more environmentally friendly biomass option. The latter involves the thermochemical gasification of biomass, which can then be combined with Fischer-Tropsch (FT) hydrocarbon synthesis to produce biofuels. This process, known as biomass to Liqiud (BtL), has the potential to significantly reduce greenhouse gas emissions and mitigate the negative impacts of climate change caused by the burning of fossil fuels. However, there are some challenges associated with the BtL process. For instance, tar production is a well-known bi-product gas conditioning that must be addressed during the gasification step. One solution is the use of catalytic steam reforming to reform the tars and undesired hydrocarbons down to their gaseous products. This increases the downstream yield of synthetic fuel and adjusts the H_2/CO-ratio in the synthesis gas, which is important for the quality of the final product.

Unfortunately, catalysts containing nickel, commonly used in steam reforming, are known to undergo deactivation over time. As a result, researchers have sought to increase the stability of these catalysts by developing alloys of nickel and other metals. One of the key challenges in this area is finding support material suitable for the catalysts. Ideally, the support should have a high surface area, basic properties, and thermal stability.

In attempts to increase the stability of the catalyst, promoters are often added to the catalyst system. Promoters are secondary metals or metal oxides that can improve the catalytic performance, activity, and selectivity of the catalyst. The choice of promoter and its concentration in the catalyst system is crucial in determining the catalyst performance.

1.1   Problem Description

This master thesis aims to further develop catalyst promoter technology aiding sustainable biofuel production. The research is a continuation of the specialization project TKP4580 and builds on the results obtained in this course. The research is a part of the Norwegian Centre for Sustainable Bio-based Fuels and Energy (Bio4Fuels) under the Centre for Environment-Friendly Energy Research.

The primary objective of this research is to produce a catalyst favorable for catalytic steam reforming of hydrocarbon impurities produced in biomass gasification. Bimetallic nickel-cobalt catalysts promoted with 1 wt% of platinum, palladium, and rhodium are synthesized and tested to analyze their effects on experimental steam reforming of methane. The research aims to determine the catalyst's activity, stability, and selectivity in varying conditions. The project will utilize various characterization techniques to determine the catalysts' structural, chemical, and elemental properties. The research was conducted in cooperation with Ask Lysne, the co-supervisor of this thesis, who performed some of the analyses, the results of which are included in this report.

1.2   Related Works

The scientific literature encompasses a broad range of articles dedicated to the study of nickel catalysts supported on hydrotalcite for applications in steam reforming and dry reforming processes. These investigations have explored various parameters, including nickel-metal ratios, total loading, and alloy compositions. The experimental parameters employed in this thesis are based on the findings and methodologies described in several of these articles. For instance, in a study conducted in 2009 by He et al. [28], Co-Ni catalysts derived from hydrotalcite-like materials were synthesized for hydrogen production through ethanol steam reforming. The catalyst employed a fixed total metal loading of 40 wt% and examined the impact of varying the nickel-cobalt ratio. The results indicated that the 30Co-10Ni catalyst exhibited the highest activity and stability over 44 hours of continuous operation. Another investigation was conducted in 2016 by Yousaf. [70] explored Ni-Co catalysts supported on a hydrotalcite-like structure for steam reforming of methane. In this particular study, the total metal loading ranged from 10 to 40 wt% while maintaining a fixed nickel-cobalt ratio of 3:7. The research findings concluded that catalysts with 40 wt% and 30 wt% metal loadings exhibited the highest reaction rates and selectivity for the desired transformation.

This research project was conducted in collaboration with Ph.D. student Ask Lysne, who played a role in planning the experimental aspects. While Lysne's Ph.D. thesis encompassing the previous experiments performed on Ni-Co catalysts is currently unpublished as of May 2023, a related study titled "Effects of Ni-Co Ratio on Deactivation and Coke Formation in Steam Reforming of Hydrocarbon Impurities from Biomass Gasification with Ni-Co/Mg(Al)O Catalysts" has been published [40]. Additionally, a former master's student at NTNU collaborated with Lysne as a co-supervisor for the thesis [41].

The experimental focus of the thesis by Øxnevad Madsen revolves around nickel cobalt catalysts supported on a hydrotalcite-like structure, with a fixed total metal loading of 40 wt% and varying nickel cobalt ratios. Specifically, the catalysts investigated included 40-0, 30-10, 20-20, 10-30, and 40-00 wt% Ni-Co compositions. Based on the findings reported [41], it was observed that the catalysts with higher nickel loadings exhibited superior activity and stability in steam reforming. However, when toluene was introduced into the system as an impurity, the 10-30 and 20-20 wt% Ni-Co catalysts demonstrated enhanced performance.

The thesis by Øxnevad Madsen explored the influence of varying temperatures and steam-to-carbon ratios on the reforming process. Specifically, temperatures of 675, 700, and 725 °C were investigated. Consistent with the existing literature, it was observed that higher temperatures led to increased methane conversion and reduced deactivation. In addition to temperature, the steam-to-carbon ratio was examined as a parameter affecting the reforming process. The study determined that a higher steam-to-carbon ratio resulted in a higher initial conversion. However, when tar was introduced into the system, this increase in conversion was only temporary. Specifically, steam-to-carbon ratios of 3 and 4 exhibited the same conversion, which was higher than that observed with a ratio of 2. Notably, the system with a steam-to-carbon ratio of 3 demonstrated the lowest deactivation, suggesting its favorable performance in terms of stability.

Drawing upon the insights gained from the aforementioned literature, the experimental design of this thesis incorporates a fixed total metal loading of 40 wt% with a nickel-to-cobalt ratio of 1. A 700°C temperature is selected to ensure optimal reaction kinetics and promote the efficient conversion of the reactants. Additionally, a steam-to-carbon ratio of 3 was employed to maintain an appropriate balance between steam availability and the carbon content of the feedstock.

2

Theory and Literature Review

This study represents a follow-up investigation to the specialization project conducted in 2022 with the title *Catalysts for Syngas Conditioning for Advanced Biofuels* [53]. Accordingly, the literature review relies upon research conducted during that period and is a repetition of this previous work with slight modifications.

2.1   Biomass to Liquid Technology

The utilization of biomass for biofuel production has gained popularity as a viable and sought-after alternative to conventional fossil fuels, driven by the growing demand for renewable energy sources and concerns surrounding global warming. Various conversion methods and feedstocks are available for biofuel production from biomass, encompassing chemical, biochemical, and thermochemical pathways [2]. Among these methods, biomass-to-liquid (BtL) technology stands out as a promising approach for the sustainable and efficient production of synthetic hydrocarbon fuels. BtL technology employs gasification and Fischer-Tropsch synthesis as key process steps. It has garnered significant attention due to its capability to convert lignocellulosic materials, classified as second-generation biomass feedstock, into biofuels using chemical, biochemical, and less commercially explored physiochemical routes [16]. Nonetheless, the thermochemical route for biofuel production remains an extensively researched field, with pyrolysis, gasification, liquefaction, and combustion being commonly utilized processes [2]. Notably, gasification has emerged as a promising and effective thermochemical route for biomass biofuel production, involving converting solid biomass into synthetic gas. The resulting syngas can be further processed to generate biofuels, including synthetic hydrocarbon fuels, methanol, and hydrogen. Gasification plays a pivotal role in the BtL process, and its extensive investigation has revealed significant potential for efficient and sustainable biofuel production.

2.1.1   Biomass Gasification

Gasification is a pivotal process that converts carbonaceous feedstocks into syngas. It involves two main categories of feedstocks: biomass and fossil fuel-based sources. While fossil fuels have historically dominated large-scale gasification plants, there is a growing interest in utilizing renewable biomass as a viable alternative or supplement to traditional fuels. Thermochemical gasification, also known as biomass gasification, serves as the initial stage in the production of liquid fuels from biomass. This process entails controlled reactions between biomass, a specific amount of oxygen and/or steam, and high temperatures. Biomass exhibits higher reactivity compared to fossil fuel feedstocks, allowing for gasification at lower temperatures than coal gasification. Lignocellulosic biomass necessitates a minimum operating temperature range of 800-900 °C [32]. Biomass gasification can utilize air at atmospheric pressure as the gasifying agent, unlike coal gasification, which requires pure oxygen under pressure.

The resulting gas, called producer gas or syngas, primarily consists of hydrogen, carbon monoxide, carbon dioxide, methane, and water. However, the gas composition during gasification varies significantly due to factors such as feedstock quality and type, gasification reactor technology, and operating conditions [45]. Trace amounts of NO_x, SO_x, higher hydrocarbons, tar, char, and particulate matter may also be present in the producer gas, depending on these factors. Various reactor technologies have been developed to address the challenges associated with gasification, including moving-bed gasifiers, fluidized-bed gasifiers, and entrained-flow gasifiers [10]. These reactors exhibit different levels of efficiency and tar yield, directly influencing the quality and value of the end product. A generalization of the tar production would place downdraft at 1 g/Nm^3, fluid beds at 10 g/Nm^3, and updraft at 100 g/Nm^3 [43]. Challenges in gasification include the removal of hydrocarbons referred to as tars, which can accumulate and cause blockages and corrosion [31]. Furthermore, impurities such as ash, nitrogen, sulfur, and chlorine-containing compounds, in the feedstock can cause the formation of undesirable NO_x and SO_x emissions and can deactivate catalysts, leading to decreased efficiency and productivity [65]. Therefore, conditioning processes are necessary to overcome these issues and enhance the efficiency and productivity of gasification systems.

2.1.2   Syngas Conditioning

Gas conditioning aims to eliminate undesired impurities from synthesis gas. Three main categories of techniques are employed: wet scrubbing, dry or dry-wet scrubbing, and hot gas conditioning [8]. Among these, hot gas conditioning is preferred due to its avoidance of tar disposal and higher conversion rates by converting tars into producer gas.

High-temperature catalyst conditioning is an efficient method to enhance gasification efficiency. This approach employs catalysts to convert unwanted tars in synthesis gas into carbon monoxide and hydrogen, either in situ, or downstream [31]. Catalysts also enable adjustment of the hydrogen-to-carbon ratio in the synthesis gas, which is crucial for downstream processing and product purity. Compared to traditional gas conditioning methods, high-temperature catalyst conversion offers advantages such as improved tar removal effi-

ciency and reduced capital and operating costs [31]. Gas conditioning plays a critical role in ensuring the production of high-quality synthesis gas for biofuel production.

2.2 Catalytic Steam Reforming

Catalytic steam reforming is a highly effective method for hot gas conditioning of synthesis gas, aiming to remove hydrocarbons from the gas stream. This process employs a catalyst to convert hydrocarbons into syngas through a series of reactions. The catalytic steam reforming method is commercially used to reform natural gas into syngas, offering several advantages over non-catalytic reforming. Notably, it operates at lower temperatures ranging from 600-900 °C, facilitating the reforming of hydrocarbons [31]. Moreover, the use of a catalyst can enhance the selectivity of the reforming process toward the production of syngas, leading to higher yields and reduced energy consumption. Catalytic steam reforming can adjust the hydrogen-to-carbon ratio in the synthesis gas, which is essential for downstream processing and product purity [51], [31].

2.2.1 Main Reactions

The steam-reforming reaction of hydrocarbons is a crucial step in the catalytic steam reforming process for hot gas conditioning of synthesis gas. This reaction involves the decomposition of hydrocarbons, typically methane, in the presence of steam to produce synthesis gas consisting of carbon monoxide and hydrogen [9]. The reactions are endothermic and can be represented by the following general chemical equation (2.1) or the methane-specific equation (2.2).

$$C_nH_m + nH_2O \Longleftrightarrow nCO + (n + m/2)H_2 \qquad \Delta H_{298}^{\circ} > 0$$
$$\text{"Steam-Reforming"} \tag{2.1}$$

$$CH_4 + H_2O \Longleftrightarrow CO + 3H_2 \qquad \Delta H_{298}^{\circ} = 206[kJ/mol]$$
$$\text{"Steam-Methane-Reforming"} \tag{2.2}$$
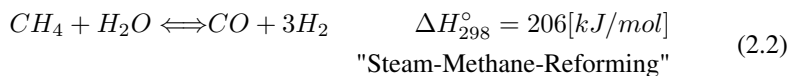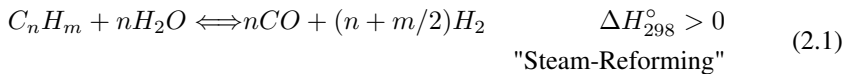
According to Le Châtelier's Principle, endothermic steam reforming reaction favors high temperature and low pressure. Le Châtelier's Principle also applies to the water-gas-shift reaction (2.3), often used with steam reforming. The water-gas-shift reaction is typically used to adjust the hydrogen-to-carbon monoxide ratio of the synthesis gas, which is essential for downstream processing and product purity [9]. Carbon monoxide reacts with excess steam to produce carbon dioxide and hydrogen gas in this reaction. However, the water-gas-shift reaction is exothermic, meaning it is favored at lower temperatures. This means that a balance must be struck between the two reactions to optimize the overall efficiency of the process.

$$CO + H_2O \Longleftrightarrow CO_2 + H_2 \qquad \Delta H_{298}^{\circ} = -41[kJ/mol]$$
$$\text{"Water Gas Shift reaction"} \tag{2.3}$$
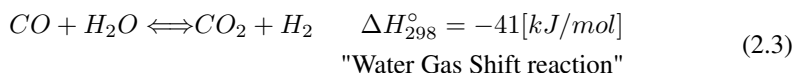
In the temperature range of 600-900 °C, commonly utilized for reforming processes, steam reforming reactions tend to shift towards the right [31]. However, it is important to note that these reactions are reversible. Consequently, the reversed reactions lead to the formation of hydrocarbons, and the left-shifted reaction (2.2) is commonly referred to as the methanation reaction.

The water gas shift process may lead to the formation of carbon dioxide, which can react with hydrocarbons instead of steam, resulting in an alternative reaction pathway known as dry reforming. The dry reforming process involves the conversion of carbon dioxide and methane into syngas through a series of chemical reactions. The chemical equations for the general and methane-specific reactions involved in dry reforming are represented by (2.4) and (2.5) [32].

$$C_n H_m + nCO_2 \Longleftrightarrow 2nCO + (m/2)H_2 \qquad \Delta H_{298}^\circ > 0$$
$$\text{"Dry-Reforming"} \tag{2.4}$$

$$CH_4 + CO_2 \Longleftrightarrow 2CO + 2H_2 \quad \Delta H_{298}^\circ = 247[kJ/mol]$$
$$\text{"Dry-Reforming"} \tag{2.5}$$
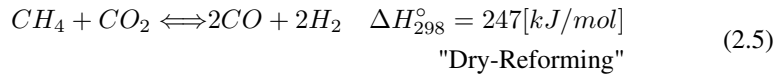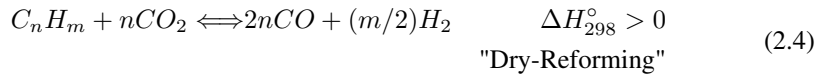
The amount of carbon dioxide produced decreases at higher temperatures, while there is an increase in the production of hydrogen and carbon monoxide as a result of the endothermic dry reforming and steam reforming reactions [9]. It should be noted that the dry reforming reactions are thermodynamically limited and require high temperatures and pressures to achieve significant conversion rates. Therefore, the use of catalysts is necessary to improve the efficiency and effectiveness of the process.

2.2.2   Steam to Carbon Ratio

The steam-to-carbon ratio is a crucial parameter in the production of synthesis gas that significantly influences the quality of the final product. This ratio refers to the ratio of steam to the carbon content of the feed gas, which in steam reforming refers to the methane in the synthesis gas and higher hydrocarbons, which can be implemented as tar models. A higher steam-to-carbon ratio facilitates the conversion of hydrocarbons and helps to suppress coke formation and thermal cracking [22]. These effects are critical to the overall efficiency and yield of the gasification process. Therefore, careful control of the steam-to-carbon ratio is necessary to optimize the production of high-quality synthesis gas for the production of biofuels [22].

Controlling the steam-to-carbon ratio can be achieved through various methods, including adjusting the steam flow rate, controlling the feedstock's carbon content, or changing the gasifier's operating conditions. However, the optimal steam-to-carbon ratio may vary depending on the type of feedstock and gasification technology employed. Therefore, a systematic approach is required to determine the optimal steam-to-carbon ratio for each specific gasification system to maximize the production of high-quality synthesis gas [22].

2.2.3 Tar

Tars are a class of condensable hydrocarbons known to cause downstream operation problems by blocking pipes and filters [23]. Tars in the gas stream can lead to reduced process efficiency and decreased yield. Therefore, it is crucial to identify and classify tars to understand their impact on the conversion process.

Tars can be categorized into primary, secondary, and tertiary tars based on their appearance, although the boundaries between these classes are not firmly established [27]. Primary tars consist of lower molecular weight oxygenated hydrocarbons, while secondary tars include phenolics and olefins. Complex and aromatic compounds are classified as tertiary tars.

Due to the complex nature of tars, tar models are often used to simplify models and experiments. The tars toluene and 1-methylnaphthalene undergo reactions according to the steam and dry-reforming equations (2.1) and (2.4)

The understanding of tars' impact on thermochemical conversion processes is essential for the optimization and development of efficient and cost-effective gasification technologies, considering catalyst activity and the necessity for regeneration of the catalyst.

2.2.4 Coke Formation

The formation of coke on the catalyst is a highly undesirable carbonaceous side product that can result from the decomposition of methane equation (2.6), the Boudouard reaction equation (2.7) [69], or decomposition of long-chained hydrocarbons and other tars during thermochemical conversion process.[32].

$$CH_4 \Longleftrightarrow C + 2H_2 \qquad \Delta H_{298}^\circ = 75[kJ/mol]$$
$$\text{"Methane Decomposition"}$$
(2.6)

$$2CO \Longleftrightarrow C + CO_2 \quad \Delta H_{298}^\circ = -173[kJ/mol]$$
$$\text{"Boudouard reaction"}$$
(2.7)
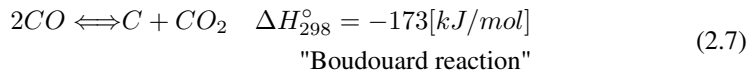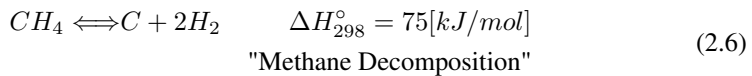
The formation of coke on the catalyst leads to decreased activity, and the degree of activity reduction depends on the type of carbon deposition. Several carbon formation mechanisms lead to catalyst deactivation, including the blockage of active sites, encapsulation, pore plugging, and whisker formation [55]. The two primary coke deposition structures in synthesis gas reforming are whisker and encapsulating carbon [69]. Carbon deposition on the catalyst's surface can result in blockage of active sites, limiting reactant accessibility and mass transport efficiency. Encapsulating carbon and whisker carbon can alter the chemical environment surrounding active sites, potentially affecting catalyst selectivity and activity and leading to deactivation. Carbon deposition can cause changes in the catalyst's morphology, reducing surface area and pore volume and leading to sintering of particles, further reducing active site availability.

The steam-to-carbon ratio is a parameter that can partially counteract coke formation. The ratio is typically between 2.5-4.5 in commercial operations to reduce the partial pressure of hydrocarbons [32]. However, a higher steam-to-carbon ratio means higher operating costs, although it reduces catalyst deactivation and hot spots. Thus, a compromise between production efficiency and economic feasibility must be established.

The minimization of coke is an essential process to maintain the catalyst's activity, selectivity, and stability, and it can be achieved through several methods. The coke-forming reactions, such as methane decomposition reaction (2.6) and the Boudouard reaction (2.7), are reversible. The coke-reforming (2.8) is promoted under the conditions found in syngas production, thus reversing coke formation.

$$C + H_2O \Longleftrightarrow CO + H_2 \qquad\qquad \Delta H_{298}^\circ = 136 [kJ/mol] \qquad\qquad (2.8)$$

In the coke removal process, the conditions of the reaction, including temperature, concentration, and resident time, play a crucial role in controlling the occurrence of carbon deposition or carbon removal. The rates of the coke-forming and coke-removal reactions depend on the gas mixture's temperature, pressure, and composition and the type of catalyst used. Several techniques for coke removal exist, including regenerative and non-regenerative methods. In regenerative methods, the spent catalyst is removed from the reactor and regenerated by burning off the coke. Non-regenerative methods involve the use of catalysts with high coke tolerance, such as metal-supported catalysts [32]. Therefore, optimal conditions for different reactor setups and catalysts are critical in achieving efficient coke removal.

2.3   Catalysts for Steam Reforming

Catalysts play a crucial role in enhancing the efficiency of the steam reforming process, especially in light of the high stability of methane. A typical catalyst comprises a support, an active material, and promoters, chosen based on their impact on activity, selectivity, and stability. In steam reforming for synthesis gas production, the desired effects of the catalyst include the ability to achieve suitable H_2/CO ratios, prevent tar formation, resist deactivation, such as coke formation and sintering, and the ability to regenerate and high methane reforming activity [31].

The material used for the catalyst should be inexpensive and readily available, and the two main types of catalyst used for steam reforming are nonmetallic mixed oxide catalysts and metal-based catalysts. Nickel is the preferred catalyst for industrial steam reforming because of its cost, high methane reforming ability, tar decomposition, and partial water gas shift activity. Noble metals have exhibited significant catalytic activity; however, their utilization in large-scale industrial applications is restricted due to their relatively high cost [31]. As such, noble metal catalyst promoters are a promising alternative.

2.3.1   Nickel

Steam reforming is a widely used process for producing synthesis gas in various industrial applications. Nickel-based catalysts have been extensively studied and are the standard for steam reforming reactions due to their high activity, selectivity, stability [29], and ability to rupture C-C bonds, which is essential for the conversion of tars [1]. Nickel-based catalysts for gas conditioning of biomass induce high methane activity and tar reforming, along with water gas shift activity. However, a significant complication with nickel-based catalysts is their propensity for deactivation, mainly due to coke formation and sintering.

Numerous studies have indicated that nickel catalysts possess exceptional performance in the steam reforming of methane. This is attributed to their high catalytic activity for methane reforming, tar decomposition, and some water-gas shift activity. However, nickel catalysts are prone to deactivation, and therefore, the effect of steam-to-carbon ratio and temperature on deactivation has been the subject of investigation. The studies have shown that lower steam-to-carbon ratios can promote coke formation, while higher ratios can lead to sintering [25], [56]. Thus, the precise control of the steam-to-carbon ratio and temperature is vital in reducing deactivation and enhancing the catalyst's lifespan.

The formation of coke on the catalyst surface during the steam reforming process can lead to the deactivation of the catalyst, which reduces its activity and stability. However, the ability to regenerate the catalyst is desirable because coke formation is likely to occur. This also makes in-situ catalyst regeneration an option to optimize syngas production. The material needed for the catalyst is preferred to be inexpensive and have high availability, which makes nickel a popular choice for industrial-scale steam reforming [56].

To address the deactivation issue, various strategies have been proposed, such as adding promoters to the nickel-based catalysts. Metals such as Mg, Ce, Co, or K have shown promising results in reducing coke formation and improving catalyst stability. However, the use of alternative catalysts such as noble metals (Pt, Pd, Rh, and Ru) has been limited due to their high cost, which makes them less applicable for industrial-scale steam reforming [25], [42], [21].

2.3.2   Cobalt

Cobalt-based catalysts have gathered significant attention for steam reforming due to their advantageous properties. Several studies have reported that cobalt-based catalysts exhibit greater stability than nickel-based catalysts, leading to a lower coke formation during the steam reforming process [19]. Cobalt-based catalysts have been found to have higher conversion rates, making them a promising alternative to conventional nickel catalysts [66].

In a study comparing the catalytic performance of cobalt and nickel catalysts supported on MgO in naphthalene reforming, cobalt was found to have the highest catalytic performance [24]. The authors attributed this finding to the high dispersion of cobalt particles on the MgO support, which promotes the active sites' accessibility, leading to higher activity and selectivity. Moreover, cobalt particles were found to have a lower tendency to sinter

and coke formation than nickel particles, leading to better catalyst stability [24].

Despite the advantages of cobalt catalysts, they are not commonly used in industrial steam reforming. One of the main reasons is the high cost of cobalt compared to nickel [24]. The properties of the support material and the reaction conditions can significantly affect the catalyst's performance, and optimizing these parameters for cobalt catalysts may require extensive research [19].

2.3.3   Bi-metallic

Bimetallic catalysts are composed of two different metals that work together to catalyze a chemical reaction. The idea behind using two metals is that each metal can contribute unique properties to the catalyst, leading to improved catalytic activity, selectivity, and stability. The improvement can be explained be due to several factors, including synergistic interactions between the two metals, improved dispersion and accessibility of the active sites, and changes in the electronic and geometric properties of the catalyst surface [35].

Mono-metallic nickel catalysts are prone to deactivation due to carbon formation, and cobalt-containing catalysts have shown an ability to reduce coke formation [24]. Therefore, the formation of nickel-cobalt alloys in bimetallic catalysts has been developed as a solution to reducing coke formation while increasing catalyst activity and stability. The resulting Ni-Co bimetallic catalysts have been reported to have higher surface area and dispersion, superior performance, and lower coke formation rates compared to their mono-metallic counterparts [41], [28]. Several studies have investigated the effect of different metal compositions on the performance of Ni-Co bimetallic catalysts [28], [70], [40], [41]. For instance, in the study by Øxnevad Madsen [41], the metal loading was kept at 40 wt% with varying nickel-cobalt ratios. It was reported that the 30-10 wt% Ni-Co and 40 wt% Ni catalysts had the best activity and stability, while the 10-30 wt% Ni-Co and 20-20 wt% Ni-Co catalysts showed the best performance with the presence of tar compounds in the system.

Overall, bimetallic catalysts offer a promising avenue for developing highly efficient and selective catalysts for various chemical processes. Further research is needed to understand the underlying mechanisms fully and to optimize the design and synthesis of these materials for specific applications.

2.3.4   Promoters

Catalyst promoters are compounds added to catalysts to enhance their activity, selectivity, and stability in a particular reaction. Promoters can change the catalyst depending on their mode of action, including structural, electronic, and chemical changes [62].

Noble metals, such as platinum (Pt), palladium (Pd), and rhodium (Rh), are known to have high activity and selectivity for many catalytic reactions [67], [48]. In steam reforming, noble metals have been shown to improve the catalytic performance by promoting the water gas shift reaction, which can increase the H_2/CO ratio in the product gas [26].

Noble metals are also known to reduce the reduction temperature needed by facilitating the hydrogen spillover effect [49]. A downside to the metallic catalysts is that they are prone to poising sulfur- and arsenic-containing compounds [60]. Overall, the exact mechanism of noble metal promoters in steam reforming is complex and multifaceted, and further research is needed to understand and optimize their use in catalysis fully.

2.3.5 Hydrotalcite

Hydrotalcites are a type of anionic and basic clay that is commonly used as support material for catalysts in various applications. The support is a layered double hydroxide material, with positively charged metal hydroxide of brucite layers and an interlayer region containing negatively charged anions and water molecules [58]. The standard formula for hydrotalcite can be seen in the following formula [39]. The interlayer region can be modified by incorporating different anions, which can alter the physical and chemical properties of the hydrotalcite [58].

$$\left[\left(M_{1-x}^{2+} M_x^{3+} (OH)_2 \right)^{x+} \left(A_{x/1}^{n-1} \cdot mH_2O \right)^{x-} \right] \tag{2.9}$$
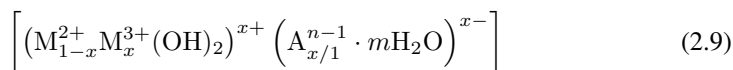
Where M^{2+} correspond to a range of metal ions including Mg^{2+}, Ni^{2+} and Mn^{2+}. M^{3+} is associated with Al^{3+}, Cr^{3+} and Fe^{3+}, while some examples of A^{n-} are OH^-, Cl^-, CO_3^{2-}, and SO_4^{2-}.
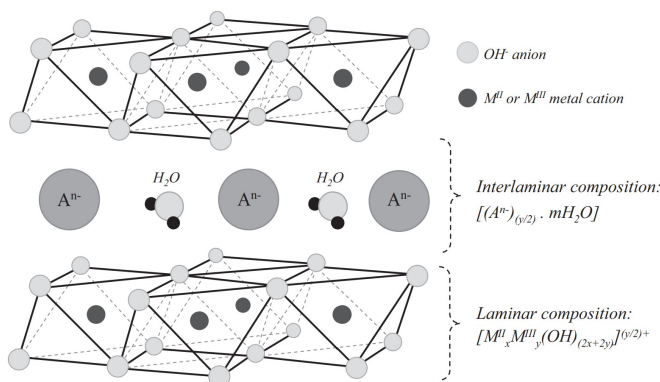
Figure 2.1: Schematic representation of the hydrotalcite structure, obtained from Salomão et al. [52].

Due to their unique porous structure and high surface area of 44.7 m^2/g, hydrotalcite can serve as excellent catalyst support. The positively charged brucite layer of the hydrotalcite attracts anionic species, which can be used as active sites for catalysis [58]. The anion and water layer of the hydrotalcite provides basicity, which can aid in various catalytic reactions.

The preparation of hydrotalcite catalyst precursors involves the co-precipitation of metal nitrates and sodium carbonate. This process leads to the formation of a hydrotalcite structure that undergoes collapse during subsequent calcination. Initially, the water molecules occupying the interstitial position are evaporated at low temperatures while preserving the structure. In the second step, the loss of hydroxyl groups and anions from the structure occurs as the temperature increases. This loss results in the collapse of the hydrotalcite and leads to an increase in its porosity [15]. The remaining metals in the hydrotalcite structure are transformed into metal oxides, further enhancing the catalyst's surface area and stability.

In the context of steam reforming, hydrotalcite has been studied as catalyst supports due to their basicity and high surface area [39]. One approach is to use hydrotalcite as a support for nickel-based catalysts, which are commonly used in steam reforming. One study evaluated the effect of various synthesis techniques, as outlined by [50]. The authors concluded that co-precipitation resulted in the most effective catalyst for methane reforming, thanks to the high specific surface area and dispersion of nickel particles. Another study, [61], reviewed the effect of nickel supported on hydrotalcite relative to nickel on alumina, particularly concerning coke deposition in steam reforming. The hydrotalcite support was found to mitigate coke formation and deposition. In conclusion, based on the studies and experimental results, it can be inferred that the hydrotalcite-like material is a suitable support for steam reforming applications. The unique properties of hydrotalcite, such as high surface area, high basicity, and excellent thermal stability, make it a favorable candidate for use in catalyst supports.

2.4   Catalyst Synthesis

Catalyst synthesis is a complex process that involves designing and producing catalyst materials with specific properties to enhance their effectiveness in catalyzing chemical reactions. The synthesis of catalysts involves the selection of appropriate precursors, synthesis methods, and conditions to achieve the desired physical and chemical properties. Precursors can be inorganic or organic, and various synthesis methods such as sol-gel, precipitation, impregnation, and hydrothermal synthesis can be employed to produce catalysts with different structures and morphologies [71]. The conditions such as temperature, pressure, and pH can also be adjusted to control the catalyst properties. Catalyst synthesis is a crucial step in the development of new and improved catalysts for various applications, including steam reforming.

2.4.1   Co-precipitation

Co-precipitation is a widely used method for synthesizing catalysts. The technique involves simultaneously precipitating two or more metal ions from a solution, resulting in the formation of a mixed metal hydroxide [5]. The process entails precipitation of the metal hydroxides, followed by the development of small elementary particles and subsequent growth or agglomeration of these particles, commonly referred to as nucleation [6].

Ultimately, this process culminates in the attainment of supersaturation of the liquid. Co-precipitation offers several advantages, including producing highly homogeneous catalysts with controlled metal composition and particle size. The method is also relatively simple and cost-effective, with the potential for scale-up to industrial levels [20]. However, co-precipitation has some limitations, including careful control of the precipitation conditions to ensure the reproducibility and consistency of the final catalyst material.

2.4.2   Calcination

Catalyst calcination is a crucial step in the synthesis of supported metal catalysts. Calcination involves high-temperature treatment of the catalyst in an atmosphere of air or oxygen, which removes any residual organic material and converts metal precursors to their active oxide forms [54]. The temperature and duration of the calcination step must be carefully controlled to prevent the catalyst from deactivating due to excessive sintering or metal oxidation. Calcination can also lead to changes in the catalyst's morphology, surface area, and chemical composition, which can affect its performance in catalytic reactions [54]. Therefore, optimizing the calcination step is crucial for developing highly efficient and stable catalysts.

2.4.3   Incipient Wetness Impregnation

Incipient wetness impregnation is a widely used method for synthesizing catalysts due to its simplicity, reproducibility, and versatility [57]. The impregnation process involves the addition of a precursor solution onto a solid support until the pores of the support are filled to the incipient point. The impregnated material is then dried and calcined to remove residual solvent and convert the precursor to the desired catalytic species. Incipient wetness impregnation enables the synthesis of highly dispersed and active catalysts with controlled metal loading and distribution on various supports. It is a prominent method used in the process of promoting catalysts.

2.4.4   Activation

Catalyst activation is a critical step in preparing catalysts for use in chemical reactions. The process involves heating the catalyst to a specific temperature in an oxidizing or reducing atmosphere to remove residual impurities and create the desired active sites on the catalyst surface [54]. The reduction of metal oxides as an activation method is ordinarily performed with H_2 and changes the catalyst precursor to catalyst.

The temperature and atmosphere used for activation depend on the type of catalyst and the desired reaction conditions. For example, some catalysts require a reduction step to create metal particles with the appropriate size and oxidation state. In contrast, others require an oxidation step to remove surface contaminants [54]. The activation process can also influence the stability and selectivity of the catalyst by controlling the degree of metal-support interaction and the dispersion of the active sites.

2.5   Catalyst Characterisation

Catalyst characterization refers to the process of determining the physical and chemical properties of a catalyst. This information is crucial for understanding a catalyst's structure and function relationship, optimizing the catalyst design and performance, and determining the effect of promotors. Catalyst characterization techniques can provide information on various properties, including the catalyst's chemical composition, surface area, porosity, crystalline structure, and particle size distribution. These characteristics are employed to gain insight into the activity, selectivity, and stability changes, which ultimately determine the catalytic performance.

2.5.1   Physisorption

The assessment of a catalyst's surface area and pore size is crucial to understand its catalytic activity, selectivity, and stability. The procedure commonly employed for this purpose is N_2 physisorption, which involves the physical adsorption of liquid nitrogen onto the pore walls and flat surfaces of the catalyst. The surface area is determined by applying the Brunauer, Emmett, and Tellers' (BET) model, while the BET plot can be used to assess the pore size distribution [14]. However, the BET model provides limited information about the pore size and other characteristics. The theory presented by Barrett, Joyner, and Halenda (BJH) can be utilized to obtain a more accurate pore size distribution value. The BET model is a generalization of Langmuir's theory of multilayer adsorption, where the amount of adsorbed nitrogen at monolayer coverage is used to calculate the internal surface area using the BET equation (2.10).

$$\frac{P}{V(P_0 - P)} = \frac{1}{V_m C} + \frac{C - 1}{V_m C} \frac{P}{P_0} \tag{2.10}$$

The BET (Brunauer-Emmett-Teller) equation involves the determination of the surface area of a solid material by nitrogen adsorption isotherms. Here, P and P_0 represent the partial pressure of nitrogen and the saturation pressure, respectively. V is the volume of nitrogen adsorbed at pressure P, while V_m is the monolayer coverage and the BET constant, denoted as C. The resulting graph also provides the slope (S) and intersection (I) values, which are needed to compute the BET constant and monolayer coverage 2.10.

$$C = 1 + \frac{S}{I} \qquad (2.11) \qquad\qquad V_m = \frac{1}{S + I} \qquad (2.12)$$

The utilization of the BET constant (C) and monolayer coverage (V_m) allows for the calculation of the total surface area (S_{tot}), which is an important parameter in determining the catalytic activity of a material. This can be achieved through the application of equation 2.13 [14]. The specific surface area (S_{BET}) can also be determined by using the aforementioned total surface area divided by the mass of the sample.

$$S_{tot} = \frac{V_m N_A s}{V} \qquad (2.13) \qquad\qquad S_{BET} = \frac{S_{tot}}{m} \qquad (2.14)$$

In this context, the symbol N_A represents Avogadro's number. The variable s denotes the cross-sectional area of the adsorbate, which is 16.2 Å for nitrogen. Lastly, the symbol m represents the mass of the sample.

The Brunauer-Emmett-Teller (BET) plot is a valuable tool for characterizing porous materials, enabling determination of the adsorption isotherm category to which a material belongs, which in turn provides insights into its pore size distribution and surface interactions [64]. The hysteresis loop, which appears in the multi-layer region of the BET plot where the adsorption and desorption curves do not overlap, is used to identify four types of hysteresis loops that were initially classified by the International Union of Pure and Applied Chemistry (IUPAC) in 1985. The hysteresis loops share a similar pore structure and adsorption mechanisms, and the identifying shapes of the isotherms are seen in figure 2.2.

(a) Types of physisorption isotherms   (b) Types of hysteresis loops
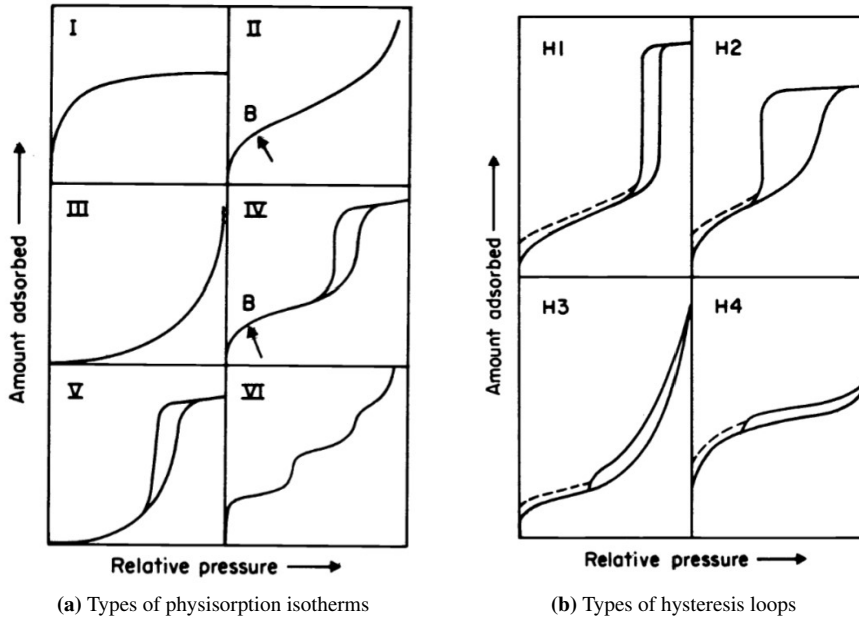
Figure 2.2: Clasification of adsorption isotherms obtained from Sing [59].

To obtain a precise pore size distribution, the BET method is combined with Barrett-Joyner-Halenda (BJH) theory, which employs the Kelvin equation for capillary condensation in pores, to calculate the adsorbed volume in the inclining or declining section of the BET plot [7]. The Kelvin equation is shown in equation (2.15).

$$ln\frac{P}{P_0} = -\frac{2\sigma V\cos\theta}{r_{pore}RT} \tag{2.15}$$

P and P_0 signify the measured pressure and saturation pressure, respectively. The variable

σ represents the system's surface tension under investigation, while V represents the molar volume of liquid nitrogen. The angle of contact between the surface of the sample and the nitrogen gas is denoted by the symbol θ. The radius of the pores, which plays a crucial role in the process of adsorption, is expressed as r_{pore}. The universal gas constant is denoted by the variable R, and the variable T represents the absolute temperature in units of Kelvin.

2.5.2 Chemisorption

Chemisorption is a widely recognized method used to determine metal dispersion and particle size in the catalyst's surface [12]. This method involves titration of probe molecules, with commonly chosen probe molecules being hydrogen or carbon monoxide. The creation of chemical bonds between the adsorbent and adsorbate selectively interacts with metals in the sample, and these bonds can be either associative or dissociative, depending on the adsorption process. The dissociative adsorption of hydrogen on metals is a typical example of this process. Using these chemical bonds, the percentage of dispersed metal particles on the catalyst surface and the particle size can be calculated. In these calculations, hydrogen-to-metal ratio, particle morphology, and uniform particle size are assumed [33].

To initiate the chemisorption experiment, the sample volume must be determined beforehand, and the stoichiometric reactions must be identified. The sample is then pre-treated and evacuated before dosing a specific amount of adsorbate gas onto the surface. The catalyst surface is repeatedly exposed to dosing to generate the adsorption isotherm, a function of the equilibrium pressure [12]. The chemisorbed monolayer uptake can be calculated by extrapolating the isotherm to zero pressure. The extrapolation is determined by a horizontal section of the isotherm fitted to Langmuir's isotherm to determine the adsorbed volume.

$$A_{specific} = \frac{V_m}{22414} N_A n \frac{1}{m} A_m \frac{100}{wt} [m^2 g^{-1} metal] \tag{2.16}$$

$$D = \frac{v_m n}{22414 m} \frac{100 m}{wt} \tag{2.17}$$

The volume of an adsorbed monolayer is denoted by V_m, while N_A represents Avogadro's number. The chemisorption stoichiometry is denoted by n, while m denotes the mass of the sample. Moreover, A_m represents the surface area occupied by a single metal atom. The metal loading of the sample is denoted by wt, while the molar volume given in cm^3/mol is equal to 22414. m denotes the atomic mass of the metal.

The hydrogen adsorption process on metals is characterized by dissociation, where a single hydrogen molecule occupies two metal sites. With the aid of previously calculated dispersion, it is possible to ascertain the particle size of the system [28]. In the case of a bimetallic system comprising nickel and cobalt, the average particle size can be determined using equation (2.18).

$$d_{(Ni-Co)}[nm] = [101/D][\%Ni/100] + [96/D][\%Co/100] \tag{2.18}$$

2.5.3 Temperature Programmed Reduction

Temperature programmed reduction (TPR) is a technique for characterizing powder cata-lysts in a reductive atmosphere. TPR provides the reduction profile of the catalyst through the observation of the chemical reaction between oxidized metals and hydrogen, repre-sented in equation (2.19), under linearly increasing temperature [44].

$$MO_n + nH_2 \Longrightarrow M + nH_2O \tag{2.19}$$
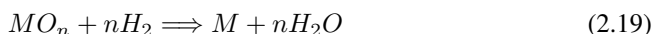
In this technique, metal oxides are reduced to their reduced metal form using hydrogen as the reducing gas in an argon atmosphere. The different oxidation states of the metal are reduced at varying temperatures, which can be used to identify the oxidation states present in the sample. It has been observed that the incorporation of noble metals into the catalyst leads to a significant shift in the reduction peaks to lower temperatures [3]. The presence of noble metals aids in initiating the reduction process. The hydrogen dissociation from the noble metal sites occurs at lower temperatures, leading to hydrogen spillover onto metal oxide sites and resulting in reduction. TPR analysis provides valuable information about a catalyst's reduction behavior, which can be utilized to optimize the catalyst's performance for a particular reaction.

2.5.4 X-Ray Diffraction

X-ray diffraction (XRD) is a widely employed analytical technique in materials science for characterizing crystalline phases and estimating their crystallite size. This method involves irradiating a crystalline material with X-rays and measuring the diffracted X-rays from its different planes [4]. The reflected X-rays form a characteristic pattern for the material, which can be used to identify its crystal structure. The constructive interference of the X-rays from parallel lattice planes is explained by Bragg's law (2.20), where the order of reflection n, the X-ray wavelength λ, and the spacing between the atomic planes d are related to the diffraction angle θ [4].

$$n\lambda = 2dsin\theta \tag{2.20}$$

The determination of particle size by X-ray diffraction involves the analysis of peak broad-ening, which is a consequence of the decrease in crystallite size [4]. The Scherrer equation (2.21) is employed to estimate the particle size, where D denotes the crystallite size, κ is the Scherrer constant, a dimensionless shape factor, λ is the X-ray wavelength, β is the full width at half of the maximum intensity after correcting for the instrumental line broaden-ing, and θ is the diffraction angle.

$$D = \frac{\kappa\lambda}{\beta cos\theta} \tag{2.21}$$

2.5.5 Inductively Coupled Plasma - Mass Spectrometry

Inductively Coupled Plasma Mass Spectrometry (ICP-MS) is an analytical technique that identifies and quantifies elements in a wide range of samples. The sample is introduced to high-temperature argon plasma generated by an inductively coupled coil [11]. The plasma ionizes the atoms of the sample, producing a stream of positively charged ions. These ions are then extracted from the plasma and directed into a mass spectrometer, where they are separated based on their mass-to-charge ratio (m/z) and detected. The intensity of the ion signal at each m/z corresponds to the abundance of the corresponding element or isotope in the sample. ICP-MS has several advantages over other analytical techniques, including high sensitivity, accuracy, and precision, as well as the ability to simultaneously measure a wide range of elements. The technique has been applied in the characterization of catalysts, where it provides valuable information about the catalyst's elemental composition and can confirm a successful synthesis with the desired values of active material and promoter percentages.

2.5.6 Scanning Transmission Electron Microscope

Scanning Transmission Electron Microscope (STEM) is a type of electron microscope that uses a focused electron beam to image the sample's surface. The STEM instrument can also detect the electrons that have passed through the sample, providing high-resolution images of the sample's internal structure. The possibility of a surface and internal structure analysis is the result of a combination of a scanning electron microscope (SEM) and a transmission electron microscope (TEM).

In SEM, a beam of high-energy electrons is focused onto a sample using electromagnetic lenses. When the electrons in the beam interact with the atoms in the sample, several different types of interactions can occur, including elastic scattering, inelastic scattering, and ionization [36]. One of the main signals used in SEM is the secondary electrons emitted from the sample surface due to the inelastic scattering process [38]. When the high-energy electrons in the primary beam collide with the atoms in the sample, some of them transfer enough energy to the atoms to knock one or more electrons out of their outer shells. These ejected electrons are known as secondary electrons. The secondary electrons emitted from the sample surface can be detected and used to form an image of the sample. This is done by scanning the beam across the sample surface and collecting the secondary electrons emitted at each point. The intensity of the secondary electron signal is proportional to the local topography and composition of the sample, allowing a detailed image of the surface to be obtained [38].

In addition to secondary electron emission, other signals can also be detected in SEM. Backscattered electrons are high-energy electrons scattered back toward the detector after interacting with the sample atoms [38]. These electrons can provide information about the composition and crystal structure of the sample. Consequently, backscattered electrons are primarily utilized to identify elemental contrasts within the sample, whereas secondary electrons are employed to investigate high-resolution morphological features.

2.5.7   Energy Dispersive X-ray Spectroscopy

Energy Dispersive X-ray Spectroscopy (EDS) is a technique that can be used with electron microscopes to analyze the chemical composition of a sample. EDS works by detecting the X-rays that are emitted when the electrons in the sample are excited by the electron beam [38]. The energy of these X-rays is characteristic of the element that emitted them, and by measuring their energy, the sample's elemental composition can be determined. EDS is often used to identify the presence of specific elements in a sample, to map the distribution of elements across a sample, and to quantify the elemental composition of a sample.

Despite its many advantages, EDS suffers from several notable limitations that can affect the accuracy and precision of the elemental quantification. One of the main drawbacks of EDS is its limited sensitivity to light elements such as carbon, nitrogen, and oxygen. This is because the X-rays emitted by these elements have lower frequencies and are harder to detect compared to X-rays emitted by heavier elements [38]. Consequently, EDS may not be able to accurately detect or quantify these light elements in a sample. Spectral overlap can also be problematic for EDS spectra, where X-rays from one element overlap with X-rays from another element, leading to inaccurate quantification. Moreover, EDS signals can be noisy due to background radiation, affecting the accuracy and precision of the elemental quantification [38]. These limitations must be carefully considered and addressed to ensure accurate and reliable results from EDS analysis.

For EDS, the depth of the interaction volume, also known as scattering depth, can limit the ability to accurately quantify the elemental composition of a sample, particularly for layered or composite materials [38]. This is because the X-rays emitted from the deeper layers of the sample may not reach the detector or be absorbed or scattered by the material before they reach the detector. As a result, the EDS signal may only reflect the elemental composition of the topmost layers of the sample, and the elemental quantification may not represent the whole sample.

2.6   Catalyst Performance

In the assessment of a catalyst and its promoter, key indicators of performance include activity, selectivity, and stability. To eliminate the influence of mass and heat transport phenomena, small catalyst particles may be employed and the catalyst bed may be diluted with inert particles to enable kinetic performance studies. High linear flow velocities and low conversion levels are critical factors in obtaining accurate kinetic data. By maintaining these conditions, the kinetic studies can achieve a high level of certainty. The evaluation of catalyst performance is essential in the development of efficient and cost-effective industrial processes.

2.6.1   Activity

Conversion is a key measure of catalyst activity and refers to the percentage of reactants that are transformed into products in a given reaction. It is calculated by comparing the

amount of reactants consumed to the amount of products formed, or reactants in the feed compared to the outlet flow (2.22). High conversion rates are desirable as they indicate that the catalyst is effectively promoting the desired reaction. However, excessively high conversion rates may result in undesired side reactions or catalyst deactivation. Thus, a balance must be struck between conversion and selectivity. Conversion can be affected by several factors, including the catalyst's surface area, active site density, and reaction conditions such as temperature and pressure.

$$X_{CH_4} = \frac{F_{0,CH_4}}{F_{CH_4} + F_{0,CH_4}} \tag{2.22}$$

Where F_{0,CH_4} is the molar methane flow in the feed and F_{CH_4} is the outlet molar flow.

Conversion can be combined with other catalytic activity measures, such as turn over frequency (TOF), site time yield (STY), reaction rate, and activation energy. TOF is a measure of the catalyst's efficiency and is calculated by dividing the number of product molecules formed per unit of time by the number of active sites on the catalyst surface, while STY is based on the assumption that each surface atom is an active site. The reaction rate measures the speed at which the reaction occurs and is typically expressed in terms of moles of product formed per unit of time. The activation energy is the energy barrier that must be overcome for the reaction to occur, and a lower activation energy generally indicates a more active catalyst. Together, these measures provide a comprehensive assessment of the catalytic activity and effectiveness of a given catalyst in promoting a particular reaction.

2.6.2 Selectivity

Catalyst selectivity refers to the ability of a catalyst to favor a specific reaction pathway, leading to the desired product. The CO/C ratio and H_2/CO ratio indicate selectivity in catalytic reactions, particularly in syngas processes. The equation used to calculate CO selectivity is seen in equation (2.23), and is based on the assumption that all carbon is converted into CO and CO_2. In the equation, S_{CO} represents the selectivity of CO. F_{CO} and F_{CO_2} represents the molar flow of CO and CO_2 out of the reactor respectively.

$$S_{CO} = \frac{F_{CO}}{F_{CO} + F_{CO_2}} \tag{2.23}$$

In the water-gas shift reaction, the CO/CO_2 ratio is adjusted to increase selectivity towards hydrogen production. The H_2/CO ratio is also crucial in determining the selectivity of catalysts in syngas processes, and downstream usage of the gas. Equation (2.24) represents shows the hydrogen to carbon ratio where F_{H_2} and F_{CO} represent the molar flow of H_2 and CO out of the reactor, respectively.

$$H_2/CO = \frac{F_{H_2}}{F_{CO}} \tag{2.24}$$

2.6.3 Stability

Catalyst stability is a critical factor affecting any catalytic process's economic feasibility and long-term viability. Deactivation is a major challenge that reduces the catalyst's stability and efficiency over time. Deactivation can occur due to various factors, such as thermal sintering, poisoning, and fouling [60]. Thermal sintering is the irreversible loss of active sites due to the coalescence of small particles at high temperatures, and poisoning occurs when the active sites are covered or blocked by adsorbed impurities, resulting in reduced catalytic activity. Fouling refers to the deposition of unwanted substances on the catalyst surface, which can block the active sites and reduce the surface area available for reaction. One example of this is coke formation.

The assessment of catalyst deactivation can be approximated by quantifying the percentage change in methane conversion. The deactivation percentage of an experiment can be determined by evaluating the average conversion at the start and a specific time, typically the end, denoted by $\overline{X}_{0,CH_4}$ and $\overline{X}_{CH_4}$, respectively, as expressed by equation (2.25). This method enables the quantification of the decrease in catalyst activity due to the development of inactive species on the catalyst surface, which leads to a reduction in reactant conversion.

$$Deactivation[\%] = \frac{\overline{X}_{0,CH_4} - \overline{X}_{CH_4}}{\overline{X}_{0,CH_4}} \tag{2.25}$$

Several characterization methods can be employed to identify the different mechanisms that lead to the deactivation of a catalyst. These methods include Scanning (Transmission) Electron Microscopy (S(T)EM), Temperature Programmed Oxidation (TPO) coupled with Thermogravimetric Analysis (TGA), and Raman spectroscopy. These techniques allow for the observation of the structural and morphological changes in the catalyst and the detection of carbonaceous deposits and other contaminants. Moreover, these techniques offer insights into the nature and distribution of metal particles, particle size, and the degree of sintering, which can impact the catalytic activity, selectivity, and stability of the catalyst.

To ensure the stability of a catalyst, various strategies are implemented, including the use of promoters or stabilizers, operating at lower temperatures, and periodic regeneration or replacement of the catalyst. These strategies can help to minimize the catalyst's deactivation and ensure its longevity in a reaction system.

2.7 Gas Chromatography

Gas chromatography (GC) is a technique used for separating and analyzing volatile compounds. The sample is first injected into a column containing a stationary phase that selectively interacts with the sample components [13]. Then, an inert gas, such as argon, is used as the mobile phase, which carries the sample components through the column. As the sample components interact with the stationary phase, they are separated based on their

unique chemical properties, such as weight, volatility, and polarity. The separated components are detected at the end of the column by a detector, such as a Thermal Conductivity Detection (TCD), which detects changes in thermal conductivity. The detector produces a signal proportional to the amount of each separated component, which is then used to create a chromatogram, a plot of signal intensity versus time. The resulting chromatogram can be used to identify the components in the sample and determine their relative quantities [13].

3

Experimental Methods

This study is a continuation of the research conducted in 2022 as part of the specialization project titled "Catalysts for Syngas Conditioning for Advanced Biofuels" [53]. Consequently, certain experimental methodologies employed in the present study were also utilized during that time frame, resulting in similarities in the description of the experimental methods applied.

The experimental methods will describe the experimental work implemented in this report, with risk assessment, catalyst synthesis, and characterization as well as the steam reforming experiments performed with the catalysts.

3.1 Risk Assessment

The hazards and corresponding safety measures related to the laboratory work and experiments carried out in this project were evaluated in accordance with the NTNU Risk Assessment protocol. A comprehensive record of the risk assessment can be located in Appendix E.

3.2 Catalyst Synthesis

The catalyst synthesis was accomplished through a sequence of co-precipitation, drying, and calcination steps. For the catalyst synthesis, an Excel solver was used in order to obtain the desired catalyst composition. The desired ratios of the catalyst composition included a total nickel-cobalt loading of 40 wt% of the oxide forms ($(Ni + Co)/(Ni + Co + Mg + Al_2O_3)$), a M^{2+}/M^{3+} ratio of 3, and a nickel-cobalt ratio of 1. Appendix A has a detailed list of the materials and weight added in the co-precipitation synthesis.

The nitrates were blended in a 3-necked round bottom flask comprising 400 mL of deionized water. In a separate round bottom flask, sodium carbonate and sodium hydroxide

were dissolved in 400 mL of deionized water. With continuous stirring of the round bottom flask containing the hydrate materials, the dissolved sodium carbonate and sodium hydroxide solution was gradually pumped over a period of 2 hours at 200mL/hour. The pH of the solution was regulated to fall within the range of 8-9 by adding nitric acid since the co-precipitation method required a consistent pH for the creation of hydrotalcite precursors. The solution was then heated to a temperature of 80 °C and allowed to age for 16 hours. The precipitate was subsequently cooled to ambient temperature and filtered. To ensure the absence of impurities, the precipitate was washed with 3 liters of deionized water. The remaining precipitate was dried overnight at 80 °C before being ground using a mortar. To ensure complete dryness, the calcination process was initiated at 80 °C for 2 hours, followed by an increase in temperature to 600 °C, where it was held for 6 hours. The catalyst was sieved into factions of $>150~\mu m$, 75-150 μm and $< 75~\mu m$.

The addition of promotors to the nickel-cobalt catalyst was achieved by incipient wetness impregnation, where three fractions of 1500.0 mg of 75-150 μm calcined catalyst were promoted with Pt, Pd, or Rh to obtain a 1.0 wt% promotion. The specific information on the materials and weight added can be found in a detailed list in Appendix A. The noble metals were weighed and separately dissolved in 2 mL of deionized water under constant stirring. The volume of deionized water corresponded to the pore volume for pre-testing with pure deionized water found in Appendix A. The concentration of each solution was calculated with the basis of a calcined sample ($NiO-CoO-MgO-Al_2O_3$) to ensure that the reduced catalyst would contain 1.0wt% of noble metal. The samples dried overnight at 80 °C and calcinated at 600 °C for 6 hours.

3.3   Characterization

3.3.1   Physisorption

Nitrogen adsorption measurements were conducted using the Micromeritics TriStar II 3020 Surface Area and Porosity Analyzer. Approximately 150 mg of the catalyst samples were loaded into specific glass reactors and subjected to a degassing process for one hour at ambient pressure, followed by an overnight degasification at 100 °C. The physisorption program was then conducted at a temperature of -196 °C, utilizing the BET (Brunauer-Emmett-Teller) and BJH (Barrett-Joyner-Halenda) theories to calculate surface area and pore size distribution.

3.3.2   Chemisorption

The Micrometrics ASAP 2020 instrument employed hydrogen as a probe molecule to determine the dispersion and particle size of the catalyst. A catalyst sample weighing approximately 100 mg was loaded into a dedicated reactor on a bed of quartz wool and covered with an additional layer of wool. The sample was evacuated for one hour prior to commencing the experiment to achieve a pressure below 0.003 mmHg, in addition to a leak test was conducted to ensure optimal conditions. The experiment was conducted according to the program detailed in table 3.1.

Table 3.1: Sequence used for hydrogen chemisorption.

Task	Temperature [°C]	Rate	Time
Evacuation	30	10	60
Automatic Leak Test	35	10	-
Hydrogen flow	670	2	960
Evacuation	670	2	30
Evacuation	35	10	90
Automatic Leak Test	35	10	-
Evacuation	35	10	30
Analysis	35	10	-

3.3.3 Temperature Programmed Reduction

The temperature profiles of the catalyst samples were determined using the Altamira BenchCat Hybrid 1000HP. Each catalyst sample weighing approximately 40 mg was loaded into a specially-designed quartz reactor, carefully arranged on a bed of quartz wool, and covered with an additional layer of the same wool. A gas mixture of 7% H_2 in Ar was introduced at a constant flow rate of 50 mL/min, and the samples were subjected to a controlled heating ramp of 10 °C/min, reacting a temperature of 670 °C and maintaining the same temperature for 5 hours. The heating is continued with a heating ramp of 10 °C/min until reaching a final temperature of 900 °C and held for 30 minutes. The hydrogen consumption was measured by the thermal conductivity detector (TCD) as a function of temperature, enabling the determination of the temperature profiles of the catalysts.

3.3.4 X-Ray Diffraction

In the X-ray diffraction analysis, Co-supervisor Ask Lysne utilized the Bruker D8 A25 DaVinci X-ray Diffractometer with CuKα radiation to obtain the X-ray diffractograms of the samples before and after calcination. The analysis of hydrotalcite was performed on the sample holders covered with Kapton film, while the metal oxide samples were transferred to a zero-diffraction Silicon cavity, placed in the sample holder, and covered with Kapton film. The background noise in the experiments was distinguished by including blank runs of the silicon cavity with Kapton film. The diffractograms were obtained using a low crystallinity program, where the measurement of 2θ was conducted from 5° to 80°, with a fixed angle of 0.1°, and a duration of 120 minutes.

3.3.5 Inductively Coupled Plasma Mass Spectrometry

The elemental analysis was carried out using ICP-MS by a third-party analytical service provider (SINTEF). The methodology employed involves decomposition with HNO_3 in a Milestone UltraWAVE and analyzed with an Agilent 8900 Triple Quadropole ICP-MS (ICP-QQQ) with SPS 4 Autosamplers. The samples were quantified against standards from Inorganic Ventures ad with 115In as an internal standard.

3.3.6 Scanning Electron Microscopy and Energy Dispersive X-ray Spectroscopy

Prior to conducting surface analysis using S(T)EM and EDS, the samples were subjected to a preparation procedure involving drop-casting onto silicon wafers. The silicon wafers were cleaned using oxygen plasma for 30 seconds to eliminate contaminants. The catalyst samples used in the syngas conditioning experiments with the tar model were dispersed in 96% ethanol and flushed with a pipette during sonication to ensure complete dissolution. The sample dispersions were then drop-casted onto the silicon wafers and dried on a hot-plate at 50 °C with three drops of samples added to obtain a sufficient number of particles. Prior to analysis in the SU9000 and the attached Oxford Ultim Extreme EDX-system, the samples hovered over with a magnet to avoid any bigger magnetic particles damaging the equipment. The equipment is located in an electromagnetic field-free room on a vibration-isolated ground to minimize any disturbances and contamination during analysis.

3.4 Catalyst Testing

To assess the activity, selectivity, and stability of the catalysts, activity tests for steam methane reforming and water gas shift were conducted. To examine the impact of tar on the system, a tar model compound was introduced to compare the performance of the catalysts in the pure syngas system and the syngas plus tar system. The experiments were performed at a constant temperature of 700 °C and a steam-to-carbon ratio of 3. The stability tests were carried out for the unpromoted Ni-Co catalyst and the platinum, palladium, and rhodium-promoted catalysts.

3.4.1 Catalytic Steam Reforming Setup

In the steam reforming experiments, a tubular fixed bed quartz reactor with an inner diameter of 6 mm was employed. A detailed illustration of the reactor used in the tar model experiments, including measurements, is presented in figure 3.1, obtained from Øxnevad Madsen [41]. The same reactor dimensions were used for the syngas experiments but without the tar inlet. Movable K-type thermocouples were strategically positioned inside and along the outside of the reactor in contact with the reactor wall. The gas distribution was precisely controlled using Bronkhorst Mass-Flow-Controllers (MFC), while the reactor furnace and evaporator were accurately programmed via Eurotherm temperature controllers.

In the experimental setup, the syngas used in the tests was provided by Linde from a 50 L gas cylinder, with a composition of 10 mol% CH_4, 25 mol% CO_2, 25 mol% CO, 35 mol% H_2, and N_2 as the balance gas. To avoid variations in the steam flow, argon was used as a carrier gas and injected prior to the evaporator. The syngas was directed into the reactor along with the argon and water, which emerges from the evaporator. To maintain a stable temperature of 700°C and avoid steam condensation, the reactor was placed inside an electric furnace, and the lines connecting the reactor to the evaporator and condenser were affixed with heating tape and isolated. A schematic illustration of the simplified flow

sheet of the setup is presented in figure 3.2. and a complete flow sheet illustrated by Ask Lysne can be found in Appendix C. The product gases were analyzed using an Agilent 490 Micro-GC equipped with a CP-COx column and a TCD. At fixed intervals, samples were injected with argon as a carrier gas and analyzed for CH_4, CO_2, CO, H_2, and N_2 as a reference gas.
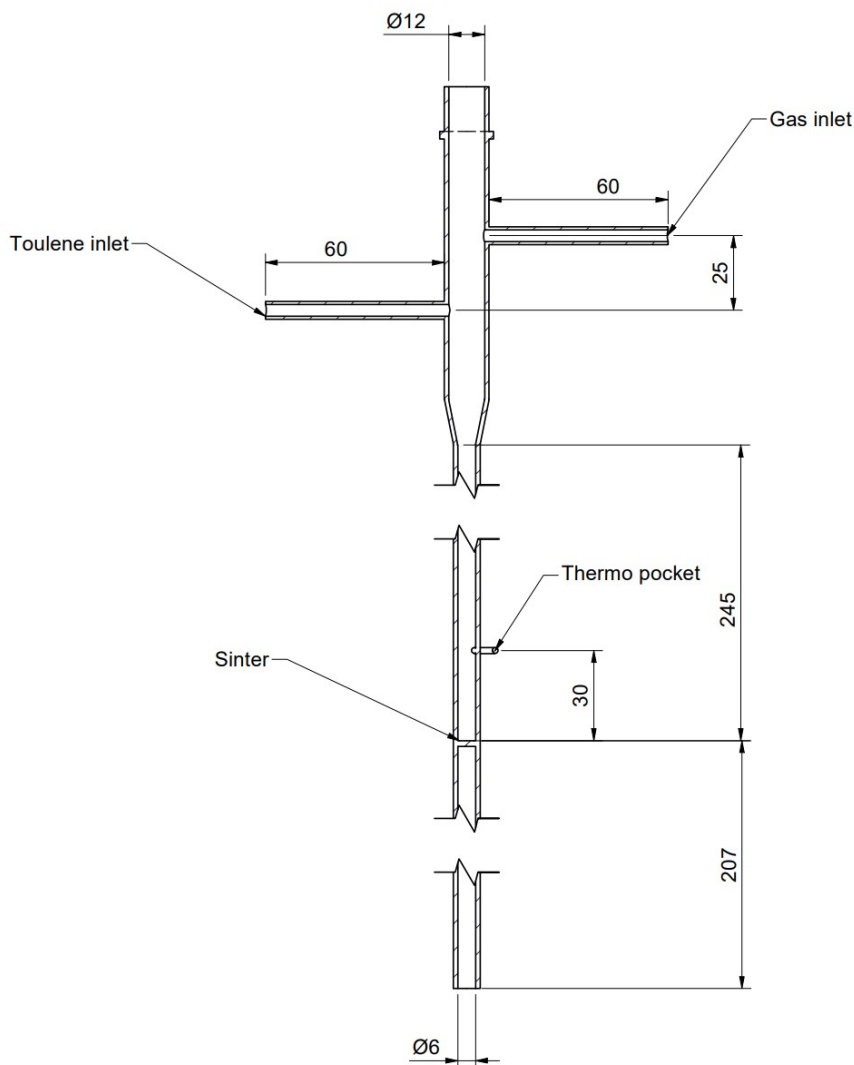
Figure 3.1: Schematic diagram of the quartz tubular fixed-bed reactor, with measurements given in [mm] obtained by Øxnevad Madsen [41].
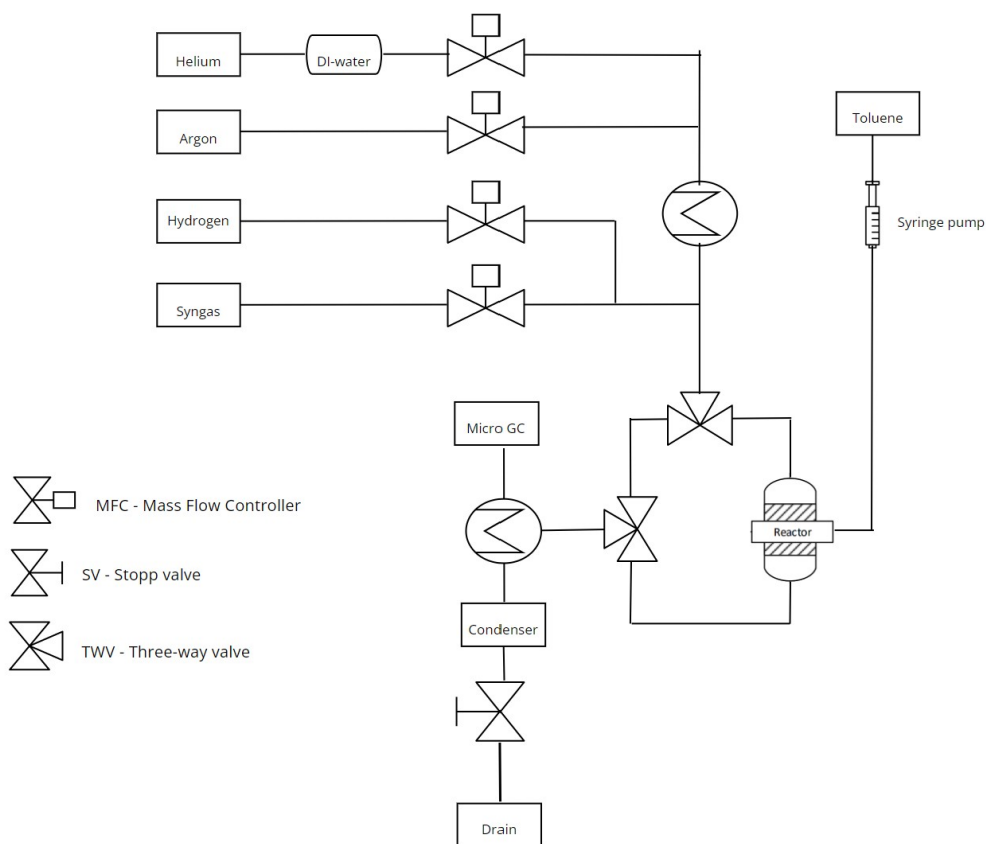
Figure 3.2: Simplified flow sheet of the experimental rig used for steam reforming.

3.4.2   Experiment Procedure

The reactor bed was loaded with 10 mg catalyst in the size range 75-150 μm diluted with 400 mg α-alumina in the size range 300-700 μm, which was previously determined to be optimal by co-supervisor Ask Lysne. The addition of α-alumina resulted in an improved temperature distribution in the reactor bed. The mixture was loaded onto a piece of alumina wool supported on the sinter inside the reactor and topped with another wool piece to keep the catalyst bed stable. The reactor was sealed with a thermo-pocked and placed in the reactor center in contact with the top of the bed.

Prior to the experiments, start-up leak tests were performed. Argon was initially used to obtain a two bar absolute pressure, and the reactor's valves and fittings were checked for gas leaks using leak detection spray. If the test indicated no signs of leaks and constant pressure was maintained, hydrogen was introduced to the system at a flow rate of 132.4 NmL/min, and the valves and fittings were checked with a flammable gas detector. The experimental parameters were held constant throughout the experiments, and a summary

of these parameters is provided in the table below.

Table 3.2: Fixed parameters for synthetic gas conversion experiments.

Parameter	Value	Unit	Symbol
Volumetric flow	850	NmL/min	$F_{V,total}$
Syngas flow	400	NmL/min	$F_{V,syngas}$
Gas Hourly Space Velocity	85000	NmL/g_{cat}min	GHsV
Mass catalyst	10	mg	m
Mass $\alpha - Al_2O_3$	400	mg	m
Height catalyst bed	8	mm	h

All mass flow controllers (MFC) utilized in the present experiment underwent calibration by the co-supervisor, Ask Lysne, prior to the experiments. The calibration curves obtained from the controllers can be found in Appendix D. The calibration of the Micro GC was also carried out, and its calibration curves can be found in Appendix D. These calibration procedures were performed to facilitate the conversion of registered peak areas in the analysis to molar fractions basis.

Activation

The activation process for each experiment involved in situ reduction of the catalyst with a mixture of 50 mol% hydrogen in argon. The flow rate of hydrogen and argon was maintained at 100 Nml/min each. The reduction process was initiated at ambient temperature and the temperature was ramped up gradually at a rate of 2 °C/min until it reached a final temperature of 670 °C, which was maintained for a duration of 16 hours.

Syngas Experiments

The steam reforming experiments were conducted at a constant temperature of 700 °C for a period of 6 hours, with continuous monitoring of the reactions via the Micro GC connected to the reactor outlet. The selection of this temperature was based on previous screening experiments [41] in order to obtain a kinetic regime suitable for studying deactivation. To maintain a steam-to-carbon ratio of 3, the flows of syngas, argon, and water were set to 400 NmL/min, 330.6 NmL/min, and 0.089 NmL/min, respectively, resulting in a total flow rate of 850 NmL/min.

Tar Model Experiments

To investigate the impact of tars on the catalyst, a tar model was introduced in the experiment consisting of 75 wt% toluene and 25 wt% methylnaphthalene, with a tar yield of 10 g/Nm^3 of syngas, based on typical fluidized bed values [43]. An electronic syringe pump was employed to add the tar model to the reactor while maintaining a steam-to-carbon ratio of 3, similar to the experiments without the tar model. The steam flow was increased, decreasing the argon flow to maintain a constant Gas Hourly Space Velocity (GHSV) compared to previous experiments. The syngas, argon, and water flows were set

at 400 NmL/min, 309.1 NmL/min, and 0.106 NmL/min, respectively, for the tar experiments. The temperature and duration of the tar experiments were kept constant at 700 °C and 6 hours, respectively.

Following the tar model experiments, the condenser was drained, and the liquid samples were collected. To identify any unreacted tar, the samples are planned to be analyzed using gas chromatography with a flame ionization detector (GC-FID) and mass spectrometry (GC-MS) by Ask Lysne, the co-supervisor at a later date.

Variations in Steam to Carbon Ratio and Temperatures

Co-supervisor Ask Lysne previously performed activity experiments of a 20-20 wt% Ni-Co catalyst synthesized using a methodology consistent with the one described earlier in this section. These experiments aimed to assess the catalyst's performance under varying steam-to-carbon ratios and temperatures, employing a tar model composed of 100% toluene. A concise summary of the experimental parameters used in Lysne's experiments is provided below to facilitate reproducibility.

In Lysne's experiments, a fixed amount of g/Nm^3 of toluene was added, aligning with the tar model experiments detailed earlier. Two of the aforementioned experiments investigated the impact of steam-to-carbon ratios, specifically ratios of 2 and 5 while maintaining a constant temperature of 700 °C. The second parameter experimented with the temperature points of 650 °C and 800 °C while maintaining a steam-to-carbon ratio of 3. The purpose of adding these activity-tested catalysts to the thesis is to analyze the catalyst's surface using S(T)EM and EDS.

4

Experimental Results and Discussion

4.1 Characterisation

The characterization techniques employed on the promoted 20-20 wt% Ni-Co catalysts were performed prior to the steam reforming experiments, with the exception of the S(T)EM and EDS surface analysis, which were performed after the steam reforming experiments. All of the reported results were obtained in the spring semester of 2023.

4.1.1 Physisorption

The surface area, pore diameter, and pore volume of the samples were determined by conducting nitrogen physisorption experiments, and their respective pore size distribution was also assessed. The obtained results, including the average surface area, pore diameter, and pore volume, are presented in table 4.1, while the adsorption-desorption isotherms can be found in Appendix B.

The addition of noble metal promoters to the 20-20 wt% Ni-Co catalyst resulted in a substantial increase in surface area. In addition, there has been a decrease in pore diameter and an increase in pore volume, as determined by BJH theory. These properties caused by the addition of noble metals result in an increase in the number of available active sites compared to the unpromoted catalyst, thereby enhancing the catalytic activity of the material.

Table 4.1: Structural data obtained from N_2 physisorption.

Catalyst	Surface Area[a] $[m^2/g]$	Pore Diameter[b] [nm]	Pore Volume[c] $[cm^3/g]$
Unpromoted	166	11.0	0.51
1.0 wt% Pt	197	9.0	0.52
1.0 wt% Pd	201	8.9	0.52
1.0 wt% Rh	197	9.2	0.52

[a] The standard deviation for the surface area was determined by the BET method to be 0.0755 using two parallel experiments of the unpromoted catalyst.

[b] The standard deviation for the pore diameter was determined by the BJH method to be 0.0128 using two parallel experiments of the unpromoted catalyst.

[c] The standard deviation for the pore volume was determined by the BJH method to be 0.001317 using two parallel experiments of the unpromoted catalyst.
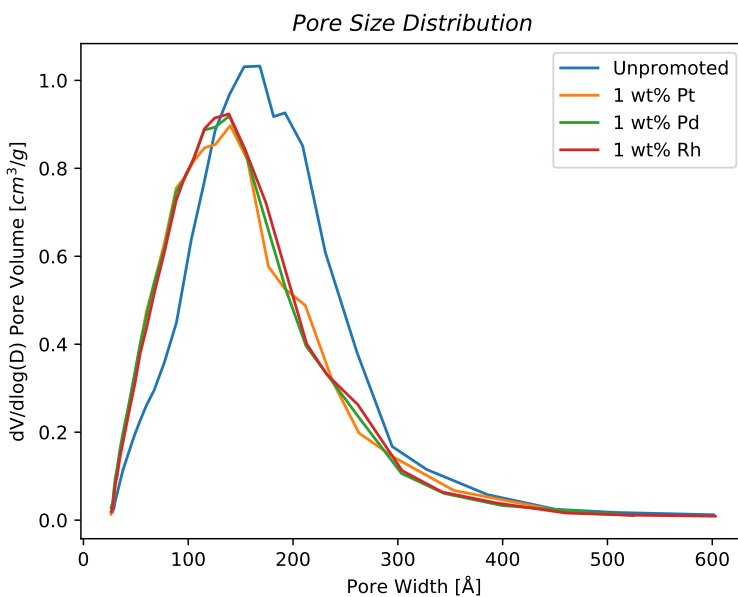
Figure 4.1: Pore size distribution of the three promoted catalysts and the unpromoted 20-20 wt% Ni-Co catalyst.

As depicted in figure 4.1, all of the pores present in the catalyst exhibit a pore size range falling within the 2-50 nm range, a characteristic indicative of mesopores [64]. This observation is further corroborated by the hysteresis loops observed in the isotherm plots for each catalyst, as provided in Appendix B. These loops correspond to a narrow distribution of mesopores, which is identified as the H1 hysteresis loop [64]. Although all catalysts exhibit a monomodal pore size distribution, the promoted catalysts display a peak pore size at 14 nm, compared to the unpromoted catalyst, which has a peak at 16 nm.

4.1.2   Chemisorption

The determination of surface metal dispersion and particle size of the catalysts were obtained using hydrogen chemisorption on the catalyst in their reduced form. table 4.2 depicts the results from the chemisorption analysis. The dispersion was determined using the total hydrogen uptake from the adsorption isotherm, and the particle size was calculated from the dispersion based on the assumptions mentioned in 2.5.2. The adsorption isotherm and repeated isotherm can be found in Appendix B.

Table 4.2: Structural data from H_2 Chemisorption.

Catalyst	Hydrogen-adsorption $[cm^3/STP]$	Dispersion [%]	Particle Size [nm]
Unpromoted	6.13 ± 0.0154	8.0	12.5
1.0 wt% Pt	7.50 ± 0.0308	9.9	10.2
1.0 wt% Pd	7.54 ± 0.0181	9.9	10.2
1.0 wt% Rh	6.37 ± 0.0222	8.3	12.1

All of the promoted catalysts show an increased dispersion and a correlating decrease in particle size. The rhodium-promoted catalyst shows almost negligible effect on the surface active metal dispersion, while platinum and palladium have similar effects. The increased hydrogen adsorption for the promoted catalysts results from noble metals' ability to increase the dispersion of transition metals. It should be noted that the particle size in table 4.2 is an average of the particle sizes found in the sample, including elemental Ni and Co particles, Ni-Co particles, and noble metal particles.

4.1.3   Temperature Programmed Reduction

In the TPR experiment, the temperature was maintained at 670 °C for a duration of 5 hours, approximately recreating the reduction process carried out in the syngas conditioning experiment setup. Followed by an increase of temperature to 900 °C for 30 minutes. The reduction reaches its peak at a bed temperature of 690 °C, which corresponds to the setpoint of 670 °C, as observed in figure 4.2. A minor reduction curve was observed for all catalysts at around 800 °C, indicating incomplete reduction at 690 °C. However, as the peak is in the lower size range, the reduction of the catalysts prior to the activity experiments was deemed sufficient.

All the catalysts exhibited two significant reduction peaks, the larger one at 690 °C, and the significantly smaller peak at 385 °C, representing nickel, cobalt and noble metal oxides present in the samples. The TPR profile for supported cobalt exhibited two reduction peaks, representing the two-stage reduction of cobalt oxide. In contrast, the second peak represented the reduction of divalent mixed metal oxide phases [34]. The reduction of spinel Co_3O_4 to CoO occurs in the temperature range of 200-400 °C, as well as the reduction of CoO to Co^0 [34]. Li and Chen showed that the TPR profile for unsupported nickel oxide exhibited a single peak at 220 °C [37]. However, adding support material resulted in the peak shift towards higher temperatures due to decreased reducibility, a

common effect observed when support structures are introduced. Due to the high shift towards higher temperature, it is theorized that nickel is present in divalent mixed metal oxide phases such as $MgNiO_2$, leading to an increased temperature peak [46].
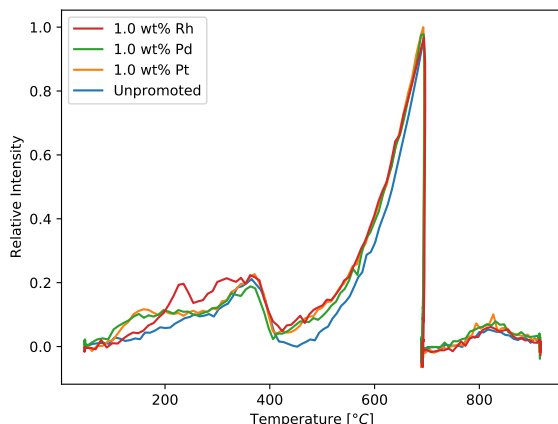
Figure 4.2: TPR profiles for the catalysts.

For hydrotalcite-derived support, the interaction of Ni and Co with the support explains the higher temperature peak leading to two separate reduction peaks. The amount of active metal substituted into the hydrotalcite lattice structure during the catalyst synthesis affects the reducibility of nickel and cobalt [28]. The strong interaction forces between the support and the Ni and Co atoms result in a higher temperature reduction peak, which entails the extraction of the atoms to the catalyst's surface. Previous studies on a similar catalyst have reported that Co^{2+} ions are more challenging to substitute into hydrotalcite structures than Ni^{2+} ions if the cobalt loading is over 10 wt% [28]. This results in more cobalt particles on the surface of the catalyst, which necessitates lower temperature for parts of the cobalt reduction, leading to the formation of two reduction peak areas [28].

The TPR profiles of the platinum-, palladium-, and rhodium-promoted catalysts exhibit a leftward shift compared to the unpromoted catalyst, with all noble metals displaying a low-temperature shoulder. Notably, Pt and Pd exhibit a more slender peak compared to Rh. This trend towards lower reduction temperatures can be attributed to the ability of noble metals to promote active metal reduction through the mechanism of hydrogen spillover. This phenomenon has been documented in previous studies on noble metal-promoted catalysts [68], [3]. Furthermore, the increase in reduction can be attributed to the enhanced surface area and active metal dispersion observed in the noble metal-promoted catalysts, leading to a greater number of active sites available for reduction.

4.1.4   X-Ray Diffraction

X-ray diffraction analysis was employed to verify the presence of hydrotalcite structure in the catalyst synthesis prior to sample calcination, as well as to compare the diffraction pattern of the calcined 20-20 wt% Ni-Co catalyst with that of the noble metal promoted catalyst, in order to discern any alterations in the crystal structure.

The X-ray diffractogram depicted in figure 4.3 exhibits the characteristic pattern of hydrotalcite, which provides evidence for the formation of the hydrotalcite structure in the catalyst synthesis. The diffractogram shows intense symmetric peaks marked with a "o" at 11 and 22, and 35° in the low range of 2θ, corresponding to the crystal planes (003), (006), and (009), respectively [28]. Additionally, less intense asymmetric peaks at 39, 46, and 62° in the higher range of 2θ represent the crystal planes (012), (015), and (018). These observed peaks are consistent with previous studies that have analyzed hydrotalcite structure [28], [46], [19], providing further confirmation for the formation of hydrotalcite in the sample. The X-ray diffractogram reveals that the primary component present is the hydrotalcite precursor without significant contamination from other materials.
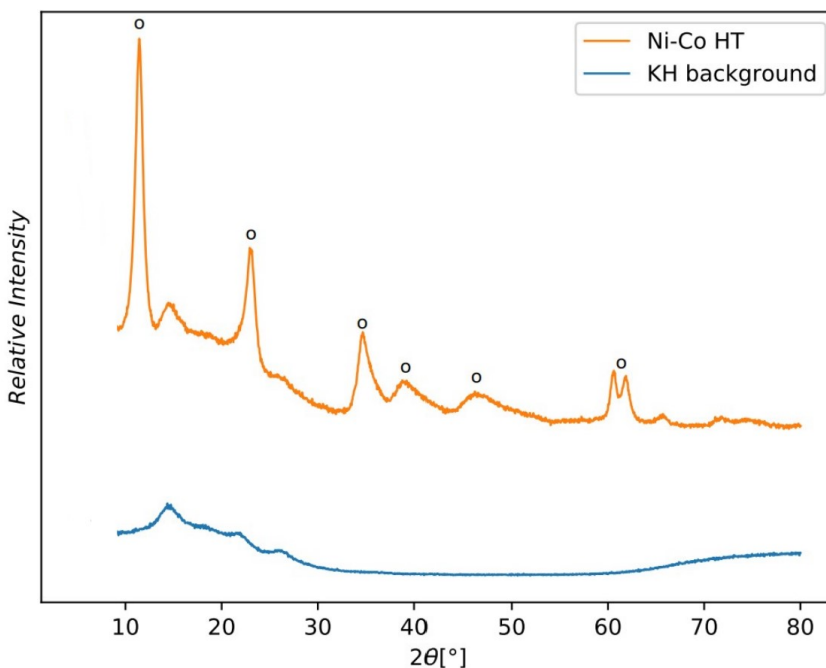
Figure 4.3: X-ray diffractogram of hydrotalcite precursor and background.

The x-ray diffractograms of the catalyst and promoted versions are presented in figure 4.4. The characteristic peaks of hydrotalcite are no longer discernible, indicating the collapse of the HT structure. The overlap in peaks arising from some of the metal oxides makes it difficult to identify the peaks. The presence of NiO, MgO, and $MgNiO_2$ is detected
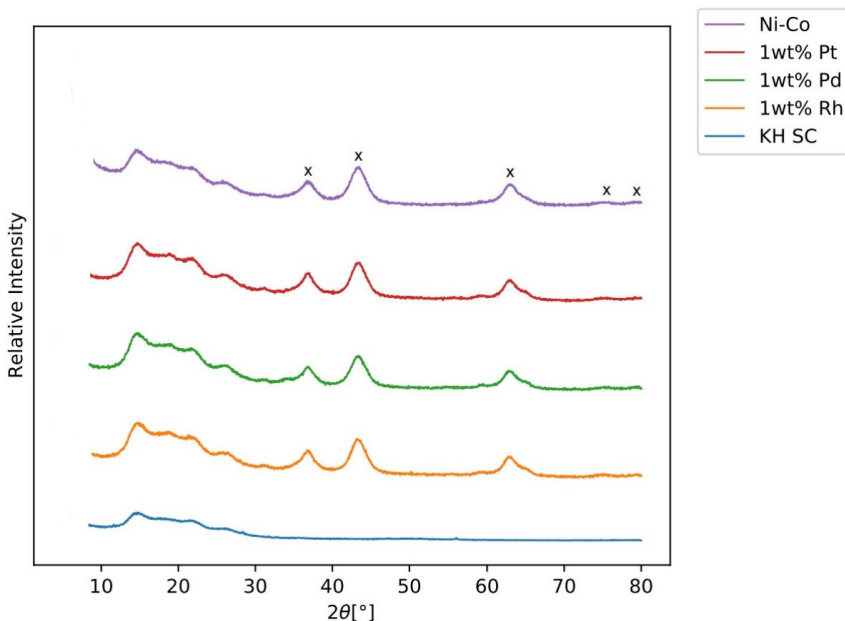
Figure 4.4: X-ray diffractogram of metal oxide catalyst and background.

in all samples, marked with "X" in figure 4.4. For the cobalt present in the samples, the cobalt oxides CoO and Co_2O_3 are not identifiable in the diffractogram. While $CoAl_2O_4$, Co_2AlO_4, $MgCo_2O_4$, $NiCo_2O_4$, and Co_3O_4 are identifiable but not distinctly visible due to the broad nickel and magnesium peaks in the same 2θ range. It is challenging to distinguish them from one another due to the similarity in XRD patterns [28]. The intensity of the peaks varies between different structures and can not be used to identify the relative intensities of the different materials.

The X-ray diffraction (XRD) pattern of the 1.0wt% Pt, 1.0wt% Pd, and 1.0wt% Rh promoted samples did not reveal any significant differences from the unpromoted Ni-Co catalyst. The noble metal additives did not produce any observable changes in the XRD patterns. This finding is consistent with the surface area measurements, which indicated similar values for the noble metal-promoted and unpromoted catalysts.

4.1.5 Inductively Coupled Plasma - Mass Spectrometry

Elemental analysis was conducted on the catalyst samples using inductively coupled plasma mass spectrometry (ICP-MS) to confirm the successful synthesis of the catalysts and ensure that the ratios used in the calculations were accurate. The analysis was carried out by an external third-party organization, SINTEF, and the results are presented in table 4.3. The first column shows the expected noble metal promotions in the 20-20 wt% Ni-Co catalysts, while the second column displays the total metal loading of nickel and cobalt in the

catalyst. The third to fifth rows provide information on the presence of noble metals in the samples. The last two columns show the nickel-cobalt ratio and the molar ratio of M^{2+} to M^{3+}.

Table 4.3: Elemental composition of the catalysts.

Catalyst	Ni-Co [wt%]	Pt [wt%]	Pd [wt%]	Rh [wt%]	Ni/Co	M^{2+}/M^{3+}
Unpromoted	44.16	-	-	-	1.11	2.94
1.0 wt% Pt	43.12	0.936	-	-	1.08	2.93
1.0 wt% Pd	43.37	-	0.893	-	1.10	2.93
1.0 wt% Rh	43.54	-	-	1.033	1.07	2.93

[a] The metals loading compositions calculations include the assumption that magnesium and aluminum are present as MgO and Al_2O_3.

[b] The molar relationship refers to the relationship in the following equation $\frac{Ni^{2+}+Co^{2+}+Mg^{2+}}{Al^{3+}}$

Based on the ICP-MS analysis results presented in table 4.3, it was observed that the total metal loading in all the catalysts exceeded the prepared synthesis amount. By comparing the metal loading and molar ion ratio it is concluded that there is a slightly deficient of magnesium. Furthermore, it was observed that all the samples had a higher percentage of nickel than cobalt, resulting in a Ni/Co ratio slightly greater than 1. Noble metals, platinum, and palladium were marginally below the target of 1.0 wt%, while rhodium was slightly above. These results suggest that the catalyst synthesis was successful, albeit with minor deviations from the intended goals.

The co-precipitation and impregnation synthesis methods are highly dependent on various parameters, such as supersaturation, temperature, and pH, which can significantly affect the resulting catalyst composition. It is possible that optimal saturation levels were not achieved during the synthesis, leading to a magnesium deficit in the samples. Sequential precipitation, where the precipitation of one metal ion occurs before the other, can also contribute to changes in the catalyst composition, leading to magnesium deficiency.

4.2   Activity Tests

The catalysts' activity for synthesis gas conditioning screening was conducted under controlled conditions at a temperature of 700 °C and with a steam-to-carbon ratio of 3. Previous experiments using a similar catalyst demonstrated that the 20-20 wt% Ni-Co catalyst derived from hydrotalcite-like precursors exhibits a linear temperature-dependency up to 700 °C [41]. This linear relationship confirms that the system operates within the kinetic regime, where mass or heat transfer limitations do not hinder the reaction rate. To assess the impact of promoter compositions on the catalyst's activity, selectivity, and stability, the obtained experimental outcomes are compared to those of the unpromoted catalyst.

To evaluate the influence of the noble metal promotors on the catalyst's activity, the methane conversion is examined as a function of time on steam. The methane conversion is determined using equation (2.22). Additionally, for selectivity measurements, the

CO selectivity and H_2/CO ratio are plotted as functions of time on steam. These values are determined by utilizing equations (2.23) and (2.24). Furthermore, the catalysts' deactivation is assessed using equation (2.25).

A tar model compound composed of 75% toluene and 25% 1-methylnaphthalene is introduced to the steam reforming system in a different set of experiments. This was done in order to determine the effect of the tar model on the catalyst and to compare them to the system without tar. A comprehensive numerical summary of the experimental data is provided in table 4.4 for the syngas experiment and table 4.5 for the tar model experiment. Each table's measurement includes an average starting value and an average ending value based on the first five and last five data points, respectively. Values denoted with a 0 notation correspond to the starting values. X represents the catalyst's activity by methane conversion, while S represents their CO selectivity. At the end of the table, D marks the deactivation observed in each catalyst.

Table 4.4: Summary of activity, selectivity, and stability parameters for the catalysts in the syngas system without tar model compound.

Catalyst	$X_{CH_4,0}{}^a$ [%]	$X_{CH_4}{}^b$ [%]	$S_{CO,0}{}^a$	$S_{CO}{}^b$	$H_2/CO,0^a$	$H_2/CO,0^b$	D^c [%]
Unpromoted	37	35	0.49	0.49	1.85	1.86	5.24
1.0 wt% Pt	39	37	0.50	0.49	1.86	1.86	5.45
1.0 wt% Pd	38	37	0.49	0.48	1.87	1.89	4.04
1.0 wt% Rh	45	42	0.51	0.49	1.83	1.90	5.24

^{a} Average of the five first data point of the measurements
^{b} Average of the five last data point of the measurements
^{c} The deactivation calculated from the five first and last data points of the activity measurements

Table 4.5: Summary of activity, selectivity, and stability parameters for the catalysts in the syngas system with tar model compound.

Catalyst	$X_{CH_4,0}{}^a$ [%]	$X_{CH_4}{}^b$ [%]	$S_{CO,0}{}^a$	$S_{CO}{}^b$	$H_2/CO,0^a$	$H_2/CO,0^b$	D^c [%]
Unpromoted	38	29	0.47	0.50	1.96	1.82	24.48
1.0 wt% Pt	40	30	0.47	0.48	1.95	1.85	25.70
1.0 wt% Pd	38	26	0.46	0.48	1.97	1.78	32.40
1.0 wt% Rh	47	30	0.48	0.49	2.04	1.87	35.57

^{a} Average of the five first data point of the measurements
^{b} Average of the five last data point of the measurments
^{c} The deactivation calculated from the five first and last data points of the activity measurements

Figure 4.5 depicts the methane conversion profiles of the catalysts in the syngas system in the left figure (a), while the right figure (b) demonstrates the impact of the tar model compound, consisting of 75% toluene and 25% 1-methylnaphthalene. To maintain a steam-to-carbon ratio of 3 during experiments involving the tar model compound, additional steam

was introduced. Consequently, the presence of less argon in the system was necessary to uphold a constant gas hourly space velocity (GHSV). However, this adjustment makes the system more susceptible to unstable flows due to argon serving as the carrier gas for steam. This makes the system more prone to abrupt spikes or drops in methane conversion or other measurements. These abrupt spikes or drops still occur without the tar model due to instabilities in the steam flow.

(a) Methane conversion in the syngas system   **(b)** Methane conversion in the tar system
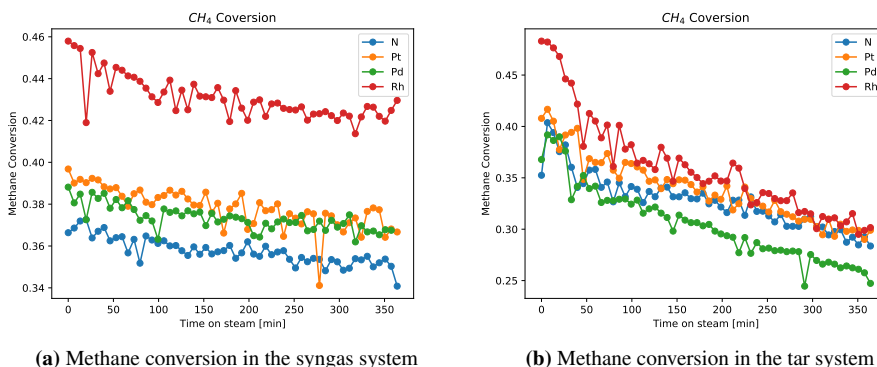
Figure 4.5: Activity measurement for steam reforming systems.

Upon analyzing the outcomes presented in figure 4.5 and the summarized data in tables 4.4 and 4.5, a notable influence of the tar model introduction to the system becomes evident. The notations on the y-axis make it evident that there are no major variations in the activity, and the graph focuses on the variations seen for the different catalysts. In the absence of the tar model, all catalysts exhibit relatively low levels of deactivation ranging from 4% to 5.5%. However, with the incorporation of the tar model, substantial changes are observed in the catalyst performance. The 1.0 wt% rhodium-promoted catalyst demonstrates significantly higher activity compared to the other catalysts. Palladium and platinum catalysts exhibit slightly higher conversions than the unpromoted 20-20 wt% catalyst while displaying similar performance in selectivity. Based on methane conversion in the tar free system, the catalysts can be ranked as follows: Rh > Pt > Pd > unpromoted.

Among the catalysts used in the system containing the tar model, palladium exhibits the lowest deactivation, with the amount of deactivation ranking as following: Pt > unpromoted > Rh > Pd. It should be noted that due to the low deactivation of these catalysts, the deactivation results are susceptible to instability in flow, leading to occasional spikes in methane conversion. Consequently, the catalytic deactivation is considered in the same range for all the catalysts.

The introduction of the tar model system leads to a pronounced catalyst deactivation when compared to the experiments conducted without the tar model. The presence of higher hydrocarbons in the tar model introduces a higher tendency for coke formation, which significantly contributes to the deactivation phenomenon. Other mechanisms, such as sintering

may also play a role in the observed deactivation, which can explain the deactivation observed in experiments conducted without the tar model. The unstable methane conversion observed in the initial phase of the tar model experiments provides further evidence for coke formation being the primary driver of catalyst deactivation. As the tar model enters the system, methane conversion experiences a rapid decline. Initially, rhodium exhibits the highest activity but eventually converges to the same activity level as the platinum and unpromoted samples. Notably, all three catalysts maintain higher activity levels than palladium.

Selectivity

The selectivity measurements encompass both CO selectivity and the H_2/CO ratio, which provide valuable insights into the catalytic system. Figure 4.6 illustrates the comparison of CO selectivity between the system with and without the tar model compound, while a similar analysis is conducted for the H_2/CO measurement, as depicted in figure 4.7. Each figure includes data for all the catalysts under investigation, allowing for an evaluation of the influence of promoters on the catalytic performance.

(a) CO selectivity in the syngas system   **(b)** CO selectivity in the tar system
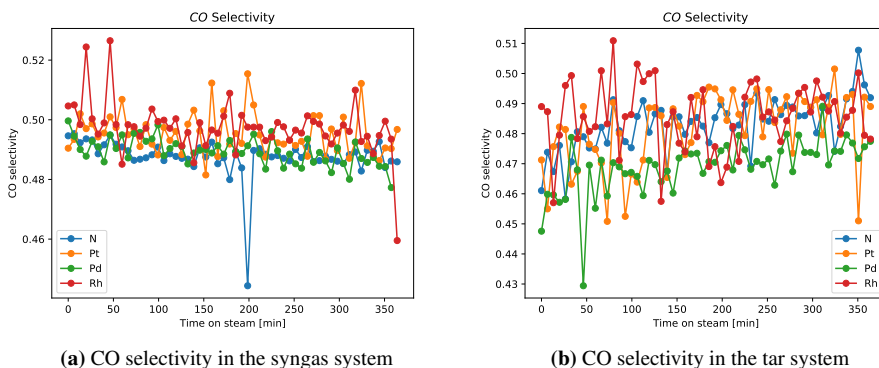
Figure 4.6: CO selectivity measurement for steam reforming systems.

In the system without the tar model, the selectivity measurements show no significant variations over time for both the CO selectivity and the H_2/CO ratio. Conversely, in experiments involving the tar model, an increase in CO selectivity and a decrease in the H_2/CO ratio are observed throughout the duration of the experiment. This behavior can be attributed to the initial absence of toluene in the system, resulting in a high steam-to-carbon ratio. However, water is consumed as the tar reforming reaction progresses, shifting the water-gas shift reaction towards the left. Consequently, the H_2/CO ratio, which initially starts at 2, gradually decreases and reaches approximately 1.8. This notable increase from the inlet ratio of 1.4 indicates that the H_2/CO ratio can be effectively adjusted during gas conditioning. This allows control over selectivity and yields for specific fuel production. An example is that a higher H_2/CO ratio favors the formation of higher hydrocarbons making it more desired for Fischer-Tropsch synthesis than methanol synthesis [47].

Comparative analysis of the noble metal-promoted catalysts and the unpromoted catalyst reveals no discernible effects of the promoters on the selectivity of the catalyst. The presence of any promoters does not result in any notable changes in the catalyst selectivity.

(a) H_2/CO ratio in the syngas system

(b) H_2/CO ratio in the tar system
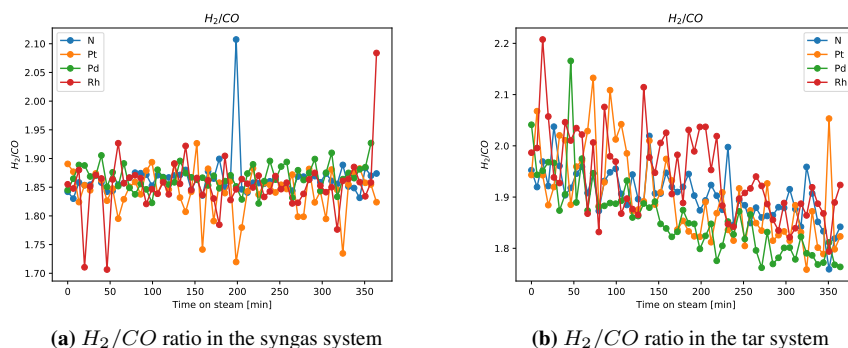
Figure 4.7: H_2/CO Selectivity measurement for steam reforming systems.

Steam to Carbon and Temperature Experiments

The activity results presented in this section were obtained from co-supervisor Ask Lysne. These experiments were conducted prior to the start of this master's thesis but are included in this report to provide relevant context, as the catalysts investigated in this work were subjected to analysis using scanning (transmission) electron microscopy (S(T)EM) and energy-dispersive X-ray spectroscopy (EDS) subsequent to the activity experiments. It is important to note that the tar models utilized in these experiments comprised 100% toluene, and this aspect should be considered when comparing the activity results with those of the promoted catalysts, along with the influence of the operating parameters.

(a) Operating conditions: S/C = 3, T = 650 and 800°C

(b) Operating conditions: S/C = 2 and 5, T = 700°C
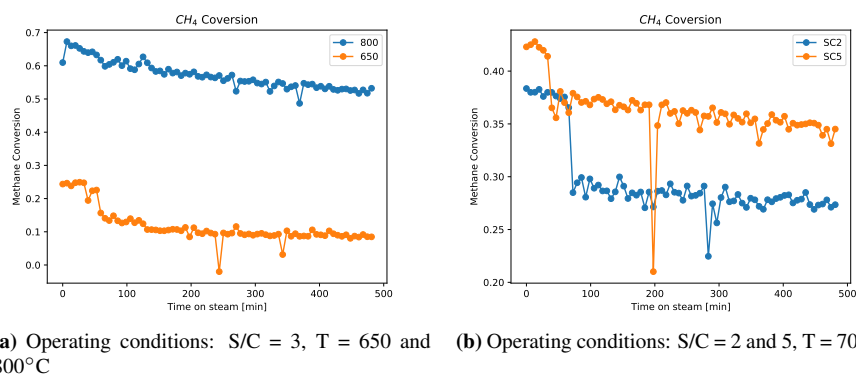
Figure 4.8: Activity measurement for steam reforming systems obtained by Lysne.

In this thesis, the activity measurements obtained from Lysne are not extensively discussed as they do not constitute the primary focus. Rather, they serve as a means to gain insights into the deactivation patterns exhibited by the catalyst under different experimental conditions. The catalyst surfaces were subjected to scanning electron microscopy (SEM) and energy-dispersive X-ray spectroscopy (EDS) analysis to elucidate the deactivation mechanisms under various operating conditions.

The observed conversions seen in figure 4.8 for different temperatures and steam to carbon align with the principles of Le Chatelier. The deactivation observed in the temperature experiments can be attributed to two primary mechanisms. At high temperatures, the catalyst is susceptible to sintering of the metal particles, resulting in a decrease in active sites and subsequent deactivation [69]. On the other hand, coke formation tends to occur at lower temperatures and lower steam-to-carbon ratios, making it the predominant deactivation mechanism for the two experiments with an S/C ratio of 2 and a temperature of 650 °C. However, no significant deactivation is observed after the initial reaction to the introduction of toluene for the catalyst experiment with the assumed coke deactivation. It is assumed that the catalyst operated at a steam-to-carbon ratio of 5 and a temperature of 700 °C exhibits minimal coke formation due to the high steam content. Hence, the predominant deactivation mechanism for this catalyst is presumed to be sintering, attributed to the abundance of steam, which has been reported to enhance particle sintering rates [18]. The catalyst demonstrating the high activity also suffers from significant deactivation, assumed to be the result of sintering. A combined SEM and EDS analysis will be conducted to ascertain the specific surface deactivation mechanisms with certainty.

4.2.1 Scanning Electron Microscopy and Energy Dispersive X-ray Spectroscopy

Post the steam reforming experiments, the catalysts underwent surface characterization using scanning (transmission) electron microscopy (S(T)EM), accompanied by element identification through energy-dispersive X-ray spectroscopy (EDS) analysis. To investigate the effects of the promoters and external parameters, such as the steam-to-carbon ratio, temperature, and tar model compounds, a catalyst solely subjected to activation was also subjected to analysis. The primary focus of this thesis is on the catalysts promoted with noble metals, operating under steam reforming conditions of a temperature of 700 °C, a steam-to-carbon ratio of 3, and a tar model compound composed of 75% toluene and 25% 1-methylnaphthalene. In collaboration with co-supervisor Ask Lysne, surface analyses of catalysts tested at varying steam-to-carbon ratios and temperatures were also conducted. It should be noted that the four catalysts synthesized and activity tested by Lysne employed a tar model consisting of 100% toluene.

Figure 4.9 illustrates the catalyst analyzed after activation, revealing a crumble-like surface structure caused by the support structure derived from the hydrotalcite-like structure of the catalyst. This structure comprises multiple layers without any discernible pattern of structural formation. Furthermore, there are no visible traces of coke on the sample since it had not been exposed to steam reforming experiments.

20.0kV x120k SE 02/06/2023   400nm
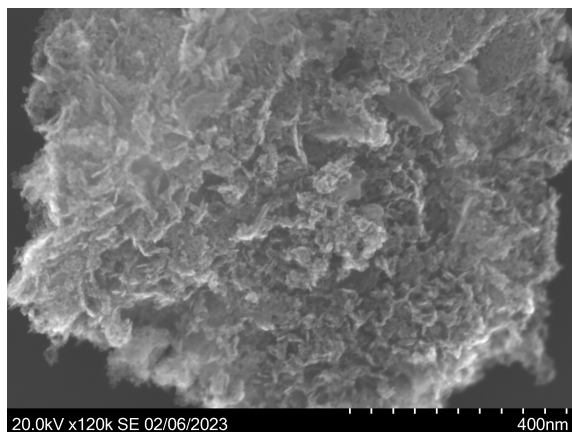
Figure 4.9: Representative picture of the surfaces of the activated catalyst.

In figure 4.10, the surface formations of each catalyst synthesized and activity tested with the tar model in this thesis are illustrated: the unpromoted catalyst (a), Pt-promoted catalyst (b), Pd-promoted catalyst (c), and Rh-promoted catalyst (d), as observed through SEM. Notably, all the catalyst surfaces exhibit crumble-like structures similar to the activated catalyst, albeit with variations in how prominent these crumbles are.

The unpromoted catalyst figure 4.10 (a) displays a less pronounced crumble structure characterized by bumps rather than the ridge-like flakes observed in figure 4.9. The underlying mechanisms responsible for this less prominent crumble structure, such as aggregation and agglomeration, cannot be definitively confirmed through SEM or EDS analysis alone. Nevertheless, EDS analysis confirms the presence of carbon but does not provide insight into the specific carbon mechanism. Encapsulating carbon and carbon filaments, also known as whiskers, are commonly encountered on catalysts used in steam reforming processes [69]. Notably, the absence of carbon filaments on the surface of the unpromoted catalyst in figure 4.10 (a) suggests that the carbon has likely taken the form of encapsulating carbon. Encapsulating carbon, a known issue associated with higher hydrocarbons such as the tar model used in this experiment [69], typically forms a carbon layer around larger metal particles. However, in this case, the characteristic structure of the carbon layer surrounding larger metal particles is not observed. This can be attributed to the absence of discernible metal particles separated from the catalyst surface, likely due to the small particle size of the catalyst and lack of sintered particles. Another explanation for the carbon is that the carbon detected in the EDS analysis is from carbon contamination, a known problem in EDS analysis of carbon. There is no way to discern the carbon mechanism. Therefore, it is suggested to perform another analysis to help identify the type of carbon present in the catalyst, such as TGA-TPO (Thermo Gravimetric Analysis - Temperature Programmed Oxidation. If the carbon detected is carbon contamination and not encapsulating carbon, the suggested reason for the catalyst deactivation would be oxidation since it has not reported any sintering of particles in the SEM analysis.

The three promoted catalysts exhibit a similar crumbling structure as observed in the activated catalyst, but they also display distinct surface characteristics, as depicted in figure 4.10. The platinum-promoted catalyst (b) reveals a higher abundance of filament carbon on the catalyst surface. However, this feature is observed to varying degrees in all the catalysts during SEM analysis. Similarly, metal particles are visible in the palladium-promoted catalyst (c); however, they are relatively rare in the sample and may potentially be located in higher quantities in the other promoted and unpromoted catalyst. While all four catalysts share a common overall surface structure, the formation of assumed encapsulating carbon is more pronounced in the unpromoted catalyst. This suggests that the presence of encapsulating carbon is less prevalent in the promoted catalysts.

(a) Unpromoted catalyst

(b) 1.0 wt% Pt promoted catalyst

(c) 1.0 wt% Pd promoted catalyst

(d) 1.0 wt% Rh promoted catalyst
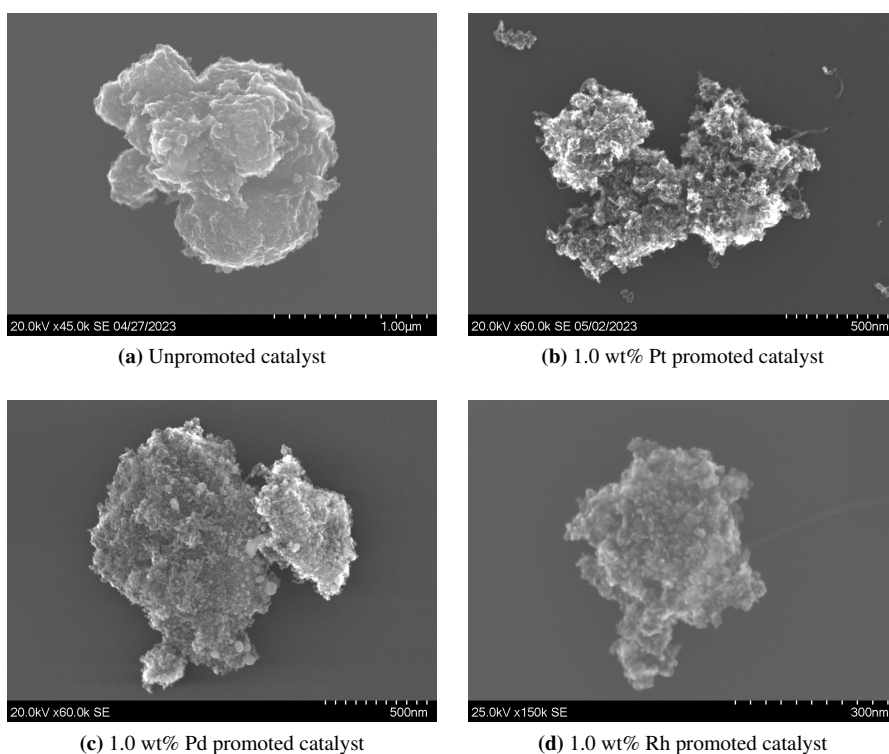
Figure 4.10: Representative picture of the surfaces of the catalysts.

By utilizing Energy Dispersive X-ray Spectroscopy, the presence of various elements within the catalyst samples was confirmed. Notably, clusters containing carbon and oxygen were detected separately from other elements throughout the samples. Carbon was found within all clusters, while the filament structures typically associated with carbon were not observed in all sample sections. The majority of the particles had a few carbon filaments when examined carefully but a lack major filament clusters. Again the carbon detected in the samples is assumed to be low amounts of encapsulating carbon or carbon

contamination.

Previous research by Chen et al. shed light on the accelerated deactivation of smaller particles, which can be attributed to a carbon bulk diffusion model. This model suggests the increased formation of encapsulating carbon, elevated carbon polymerization rates, and enhanced carbon coverage [17]. These factors contribute to the observed rapid deactivation of the catalysts. In addition to encapsulating carbon, filament clusters and individual strands of filament carbon were sporadically observed. Figure 4.11 presents an example of the filament clusters detected in the samples.

(a) Filament cluster observed in the Pd promoted catalyt

(b) A close up of the non fused carbon filaments seen in (a)

(c) Fused carbon filament found in the Pd promoted sample

(d) Carbon filament cluster fused with Pt promoted catalyst
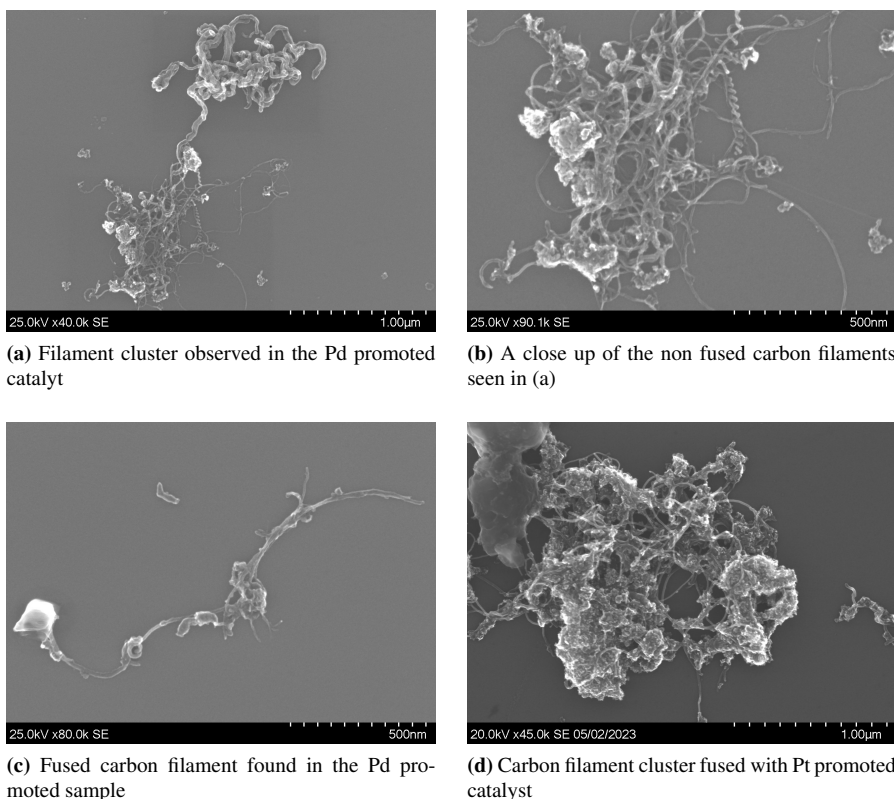
Figure 4.11: Types of filament clusters observed throughout the catalyst samples.

The formation of filaments, unlike encapsulating carbon, does not lead to the same level of deactivation as they grow without obstructing active sites. Notably, the diameter of the filaments observed in the current sample is smaller compared to previous literature on similar catalyst types [40]. It is crucial to highlight an important distinction between the experiments conducted by Lysne et al. and the experiments performed in this thesis, namely the implementation of the tar model and the duration of the steam reforming operation. While Lysne et al. employed a tar model consisting of 100% toluene and conducted

an 8-hour experiment, this thesis utilized a tar model comprising 75% toluene and 25% 1-methylnaphthalene, with a run time of 6 hours. These variations in the tar model composition and experimental duration may influence carbon formation and the size of metal particles observed in the catalysts. As filaments are known to grow from metal particles, the particle size is reflected in the filament diameter. In the experiments conducted by Lysne et al., metal particles were discerned within their samples, whereas no distinct particles are evident in the unpromoted or promoted catalysts of the present study. The normalized filament diameter distribution is presented in figure 4.12, providing insights into the filament sizes observed in the samples.

(a) Unpromoted catalyst

(b) 1.0 wt% Pt promoted catalyst

(c) 1.0 wt% Pd promoted catalyst

(d) 1.0 wt% Rh promoted catalyst
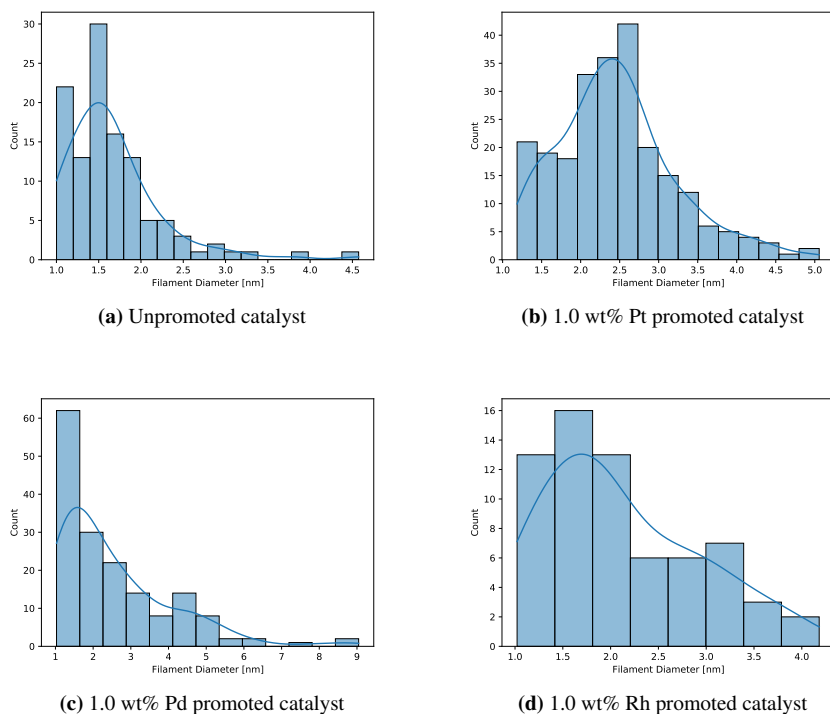
Figure 4.12: Filament diameter distributions for each of the catalysts.

Figure 4.11 (a) and (c) illustrate clusters of carbon filaments with a highly diverse range of filament diameters. While some sections of these clusters may appear as a single filament, their bulkiness and texture indicate the presence of multiple fused filaments. It is important to note that these fused filaments are not included in the filament diameter distribution analysis. Due to the limited occurrence of carbon filaments in the samples, the sample size used for the diameter distribution analysis is relatively small. The observed filament diameters range from 1 to 5 nm, seen in figure 4.12. Prominent peaks at 1.5 nm for all catalysts except the platinum-promoted catalyst, which exhibits a slightly higher filament diameter peak at 2.5 nm. The presence of these small filament diameters can be attributed

to the presence of non-measurable metal particles in the samples, likely influenced by the steam reforming parameters. Notably, there is no significant impact of the noble metal promoters on the diameter of carbon filaments.

Operating Parameters Surface Analysis

SEM and EDS analysis were conducted on the spent steam reforming catalysts provided by Ask Lysne, focusing on extreme temperature and steam-to-carbon ratio conditions. The catalyst synthesized by Øxnevad Madsen and Ask Lysne for these experiments is of the same composition as the unpromoted catalyst examined in this thesis. [41]. Selected characterization results are summarized in table 4.6 to compare the catalyst surface characteristics to the catalyst analyzed above. It is important to note that the tar model employed in these experiments solely comprised pure toluene, as mentioned previously.

Table 4.6: Summary of the structural data obtained by Øxnevad Madsen [41].

Structural data	Obtained results
Surface Area [m^2/g]	162
Pore diameter [nm]	11
Dispersion [%]	6.1
Particle size [nm]	16.3

Figure 4.13 provides the operating temperature and steam-to-carbon ratios corresponding to each catalyst. With the exception of the catalyst operating at 800 °C, all catalysts exhibit a similar surface structure. Notably, the three catalysts operating at lower temperatures display a significant presence of carbon filaments. The catalyst particles are observed to be covered with varying degrees of filaments, fused filaments, and encapsulating carbon. These distinct carbon structures are depicted in figures (a), (c), and (d), respectively. It is important to note that all of these carbon structures were observed across all respective operating conditions. Additionally, extensive filament clusters were observed without any detected catalyst particles, suggesting that carbon filaments are the predominant carbon species in these samples.

The SEM analysis of the spent steam reforming catalyst operated at a temperature of 800 °C, as shown in figure 4.13 (b), reveals the presence of circular metal particles with a lighter tone dispersed throughout the catalyst particles. Through the use of energy-dispersive X-ray spectroscopy (EDS), as depicted in figure 4.14, it was confirmed that these particles consist of nickel and cobalt. These metal particles are observed in significant quantities throughout the entire sample, suggesting a prevalent mechanism of catalyst sintering.

Sintered particles were also expected to be present in the sample tested at an S/C ratio of 5. A speculated explanation of these results involved the preparation of the catalyst prior to the SEM analysis with a strong magnet to avoid possible damage to the instrument. The magnet may remove the sintered particles, giving the samples the appearance

(a) Operating conditions: S/C = 3, T = 650°C

(b) Operating conditions: S/C = 3, T = 800°C

(c) Operating conditions: S/C = 2, T = 700°C

(d) Operating conditions: S/C = 5, T = 700°C
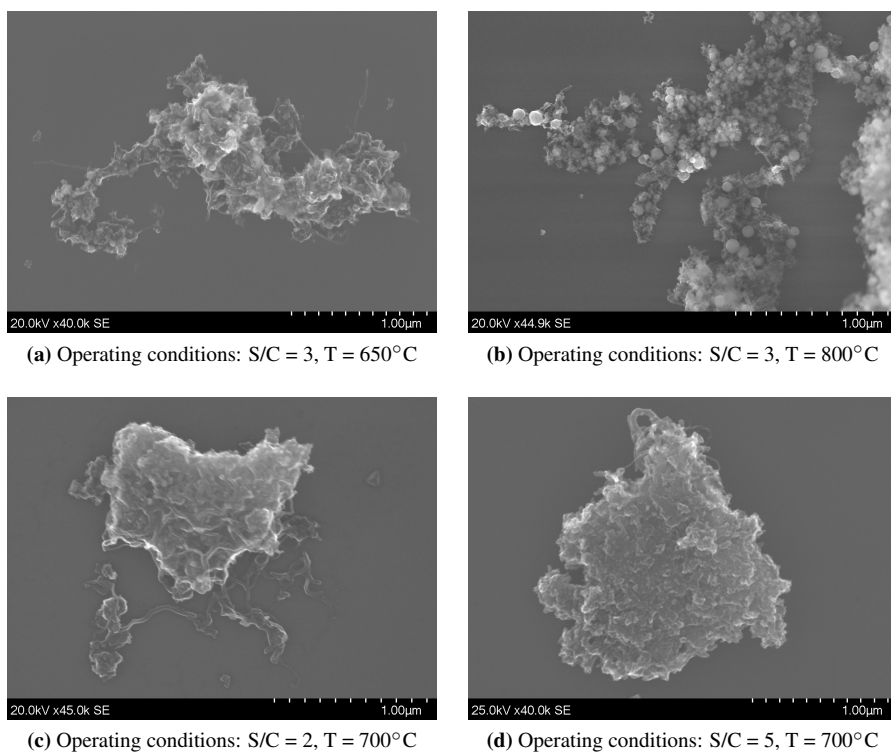
Figure 4.13: Representative picture of the surfaces of the catalyst.

of no sintered particles. The catalyst tested at 800 °C is assumed to have an abundance of sintered particles and, therefore, still exhibits these particles. This is however just speculation based on the deviation mechanisms expected for the catalysts. A proposition of reproduction of the experiments involves a weaker magnet for the catalyst preparation if the instrument responsible deems it safe for the instrument.

Ask Lysne conducted an analysis of the catalyst tested at 800 °C of 279 metal particles and determined the average diameter to be 51 nm with a standard deviation of 19 nm. In order to ascertain the Ni/Co ratio maintained from catalyst synthesis to particle sintering, point scans were performed on the metal particles. The scans revealed an average Ni/Co ratio of 1.2, indicating a slight deviation from the expected ratio of 1. This deviation is so low that it could be caused by overlapping of the EDS signals. Based on the presence of these metal particles, the limited detection of carbon filaments in the samples, and the absence of encapsulating carbon, the active material's sintering is considered the catalyst's primary deactivation mechanism.
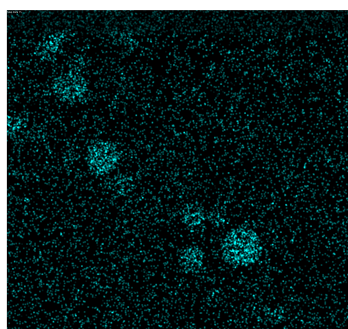
(a) Nickel detected using EDS
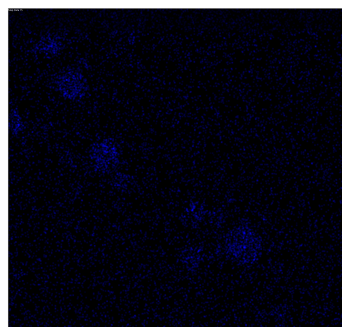
(b) Cobalt detected using EDS
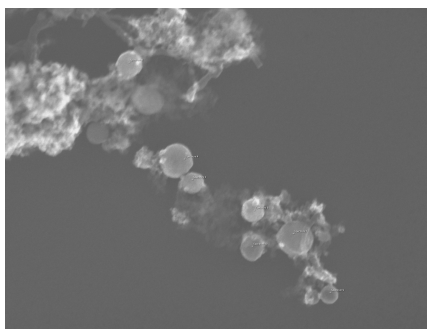
(c) Electron image of the EDS analysed particles

Figure 4.14: EDS results from the catalyst exposed to the operating conditions: S/C = 3, T = 800°C during steam reforming.

Table 4.7 provides a summary of the average carbon filament diameter observed in the

catalysts analyzed in the operating parameter study. It is noteworthy that the filament diameters fall within the same range across all the catalysts tested, indicating a consistent filament size selectivity irrespective of the variations in operating parameters.

Table 4.7: Summary of the average carbon filament diameter found in the samples obtained from co-supervisor Ask Lysne.

Temperature [°C]	S/C ratio	Carbon filament diameter $\pm$ std [nm] [a]
650	3	17 ± 5
800	3	20 ± 4
700	2	23 ± 6
700	5	19 ± 6

[a] Carbon filament diameter SEM analysis from the average of 254-299 particles. Standard deviation is indicated in the table

5

Conclusion and Further Work

One route to biofuel production is through the combination of gasification and Fischer-Tropsch synthesis. An important part of this process is intermediate gas conditioning, also known as steam reforming. In pursuit of advancing catalyst performance in steam reforming, an investigation was conducted employing a 20-20 wt% Ni-Co catalyst derived from a hydrotalcite-like precursor promoted with noble metals. Specifically, three catalyst formulations were prepared, featuring promotional loadings of 1.0 wt% platinum, 1.0 wt% palladium, and 1.0 wt% rhodium.

Prior to commencing the steam reforming experiments, a comprehensive analysis of the catalyst's physiochemical properties was conducted to assess the impact of noble metal promotions on activity, selectivity, and stability. The noble metal promotion of the catalysts resulted in an increase in surface area, with similar outcomes observed for the Pt, Pd, and Rh-promoted catalysts. Furthermore, the Pt and Pd-promoted catalysts exhibited a slight enhancement in dispersion and a reduction in particle size compared to both the unpromoted and Rh-promoted catalysts, as confirmed through chemisorption analysis. Analysis of the reduction behavior revealed the presence of two distinct temperature reduction peaks for all catalysts, with a notable shift towards lower temperatures observed in the noble metal-promoted catalysts. This shift is attributed to the hydrogen spillover phenomenon induced by the noble metals, while the two reduction peaks correspond to the low-temperature reduction of spinel-phases and the high-temperature reduction of divalent mixed metal oxides. These mixed metal oxides are also observed after the decomposition of the hydrotalcite-like structure with XRD, and it was noted that the noble metals did not instigate any discernible changes in the crystalline structure. Elemental analysis was performed to validate the successful synthesis of the catalyst, albeit minor deviations from the intended objectives were observed. Specifically, a slightly higher weight percentage of active metals was reported alongside a slightly lower M^{2+}/M^{3+} ratio, indicating a marginal magnesium deficiency.

In the steam reforming experiments, the rhodium-promoted catalyst displayed the highest

level of methane conversion. In the absence of the tar model, minimal deactivation was observed for all the catalysts. However, when introducing the tar model, a rapid deactivation phenomenon was observed across all catalysts. Notably, in the presence of tar, the rhodium-promoted catalyst initially demonstrated the highest activity but experienced rapid deactivation, ultimately reaching the same activity level as the other catalysts after a duration of 6 hours on steam. Regarding selectivity measurements, all catalysts exhibited similar levels of CO selectivity and H_2/CO ratio in both tar and non-tar systems. However, the introduction of tar resulted in an increased CO selectivity and a decreased H_2/CO ratio.

The activity experiments conducted by Lysne revealed that elevating the temperature and increasing the steam-to-carbon ratio had a higher catalytic activity. However, it is worth noting that these catalysts exhibited a common challenge of rapid deactivation, which occurred after the initial drop in activity upon introducing the tar model.

The SEM and EDS surface analysis conducted after the steam reforming experiments involving the tar model revealed notable similarities among the promoted catalysts. The samples exhibited a layered crumbled structure accompanied by minor clusters of carbon filaments, while sintered Ni-Co particles were extremely rare. Comparatively, the unpromoted catalyst exhibited a less prominent layered crumble structure but displayed similarities to the promoted catalysts in other observed aspects. The measured filament diameters ranged from 1 to 5 nm, assuming that these filaments have minimal impact on deactivation. The EDS analysis detected the presence of carbon, suspected to be either encapsulated carbon or carbon contamination. It is important to note that carbon contamination poses a known challenge in EDS analysis. Depending on the specific type of carbon present, either encapsulated carbon or oxidation is presumed to be the primary deactivation form. To ascertain the precise carbon mechanisms operating on the catalyst, a TGA-TPO analysis is recommended.

The catalysts subjected to various steam reforming parameters exhibited comparable surface structures, except for the high-temperature experiment. In the case of the high-temperature experiment, the sample exhibited a coating of sintered Ni-Co particles, as determined by EDS analysis, with an average particle diameter of 51 nm. Conversely, the remaining catalysts were characterized by the presence of carbon filaments, and no sintered particles were observed. These filaments displayed a consistent diameter range of 15-25 nm across all catalyst samples.

The results obtained from this investigation establish that the rhodium-promoted catalyst exhibited the highest initial activity. However, when exposed to the tar model, a rapid deactivation process ensued, leading to an activity level equivalent to that of the unpromoted catalyst by the end of the experiment. Consequently, in the absence of a catalyst regeneration system, the promotion conferred no advantage.

5.1   Further Work

An important consideration in this study is the identification of the specific coke mecha-
nisms responsible for catalyst deactivation, warranting further investigation to determine
these deactivation mechanisms. One approach is to employ Thermogravimetric Analy-
sis (TGA) coupled with Temperature-Programmed Oxidation (TPO) to ascertain weight
changes and types of carbon species present, thus complementing the SEM and EDS anal-
yses. Furthermore, it is advisable to explore the possibility of mitigating potential errors
of removed sintered particles during sample preparation using a powerful magnet.

Regarding the rapid deactivation observed in the tar system, it is plausible that the deacti-
vation process may reach a state of equilibrium over time, wherein a balance between coke
reforming reactions and coke removal reactions is established. Therefore, conducting ex-
tended activity experiments is recommended to investigate whether deactivation stabilizes
after a certain duration or persists due to ongoing coke formation.

Further experimentation is possible, examining the impact of noble metals on in situ re-
forming of the catalyst. The high activity demonstrated by the rhodium-promoted catalyst
might be sustained through in situ catalyst regeneration, potentially yielding even higher
catalytic performance compared to the non-promoted catalysts. If the in situ regeneration
yields discouraging results it is advised to explore promotion via other elements which
potentially could yield higher activity.

Bibliography

[1] , 2013. Chapter 7 - hydrogen from bioethanol, in: Gandía, L.M., Arzamendi, G., Diéguez, P.M. (Eds.), Renewable Hydrogen Technologies. Elsevier, Amsterdam, pp. 135–169. URL: *https://www.sciencedirect.com/science/article/pii/B9780444563521000076*, doi:*https://doi.org/10.1016/B978-0-444-56352-1.00007-6*.

[2] Adams, P., Bridgwater, T., Lea-Langton, A., Ross, A., Watson, I., 2018. Chapter 8 - biomass conversion technologies, in: Thornley, P., Adams, P. (Eds.), Greenhouse Gas Balances of Bioenergy Systems. Academic Press, pp. 107–139. URL: *https://www.sciencedirect.com/science/article/pii/B9780081010365000082*, doi:*https://doi.org/10.1016/B978-0-08-101036-5.00008-2*.

[3] Al-Saleh, M., Hossain, M., Shalabi, M., Kimura, T., Inui, T., 2003. Hydrogen spillover effects on pt–rh modified co–clay catalyst for heavy oil upgrading. Applied Catalysis A: General 253, 453–459. doi:*10.1016/j.apcata.2003.06.001*.

[4] Ali, A., Chiang, Y.W., Santos, R.M., 2022. X-ray diffraction techniques for mineral characterization: A review for engineers of the fundamentals, applications, and research directions. Minerals 12. URL: *https://www.mdpi.com/2075-163X/12/2/205*, doi:*10.3390/min12020205*.

[5] Ashik, U., Kudo, S., ichiro Hayashi, J., 2018. Chapter 2 - an overview of metal oxide nanostructures, in: Mohan Bhagyaraj, S., Oluwafemi, O.S., Kalarikkal, N., Thomas, S. (Eds.), Synthesis of Inorganic Nanomaterials. Woodhead Publishing. Micro and Nano Technologies, pp. 19–57. URL: *https://www.sciencedirect.com/science/article/pii/B9780081019757000026*, doi:*https://doi.org/10.1016/B978-0-08-101975-7.00002-6*.

[6] Athar, T., 2015. Chapter 17 - smart precursors for smart nanoparticles, in: Ahmed, W., Jackson, M.J. (Eds.), Emerging Nanotechnologies for Manufacturing (Second Edition). second edition ed.. William Andrew Publishing, Boston. Micro and Nano Technologies, pp. 444–538.

URL: *https://www.sciencedirect.com/science/article/pii/B9780323289900000178*, doi:*https://doi.org/10.1016/B978-0-323-28990-0.00017-8*.

[7] Barrett, E.P., Joyner, L.G., Halenda, P.P., 1951. The determination of pore volume and area distributions in porous substances. i. computations from nitrogen isotherms. Journal of the American Chemical Society 73, 373–380. URL: *https://doi.org/10.1021/ja01145a126*, doi:*10.1021/ja01145a126*.

[8] Basu, P., 2018a. Chapter 6 - tar production and destruction, in: Basu, P. (Ed.), Biomass Gasification, Pyrolysis and Torrefaction (Third Edition). third edition ed.. Academic Press, pp. 189–210. URL: *https://www.sciencedirect.com/science/article/pii/B9780128129920000066*, doi:*https://doi.org/10.1016/B978-0-12-812992-0.00006-6*.

[9] Basu, P., 2018b. Chapter 7 - gasification theory, in: Basu, P. (Ed.), Biomass Gasification, Pyrolysis and Torrefaction (Third Edition). third edition ed.. Academic Press, pp. 211–262. URL: *https://www.sciencedirect.com/science/article/pii/B9780128129920000078*, doi:*https://doi.org/10.1016/B978-0-12-812992-0.00007-8*.

[10] Basu, P., 2018c. Chapter 8 - design of biomass gasifiers, in: Basu, P. (Ed.), Biomass Gasification, Pyrolysis and Torrefaction (Third Edition). third edition ed.. Academic Press, pp. 263–329. URL: *https://www.sciencedirect.com/science/article/pii/B978012812992000008X*, doi:*https://doi.org/10.1016/B978-0-12-812992-0.00008-X*.

[11] Beauchemin, D., 2004. Inductively coupled plasma mass spectrometry. Analytical Chemistry 76, 3395–3416. URL: *https://doi.org/10.1021/ac040068n*, doi:*10.1021/ac040068n*, arXiv:https://doi.org/10.1021/ac040068n. pMID: 15193116.

[12] Bergeret, G., Gallezot, P., 2008. Particle Size and Dispersion Measurements. John Wiley & Sons, Ltd. chapter 3.1.2. pp. 738–765. URL: *https://onlinelibrary.wiley.com/doi/abs/10.1002/9783527610044.hetcat0038*, doi:*https://doi.org/10.1002/9783527610044.hetcat0038*.

[13] Blumberg, L.M., 2012. Chapter 2 - theory of gas chromatography, in: Poole, C.F. (Ed.), Gas Chromatography. Elsevier, Amsterdam, pp. 19–78. URL: *https://www.sciencedirect.com/science/article/pii/B978012385540400002X*, doi:*https://doi.org/10.1016/B978-0-12-385540-4.00002-X*.

[14] Brunauer, S., Emmett, P.H., Teller, E., 1938. Adsorption of gases in multimolecular layers. Journal of the American Chemical Society 60, 309–319. URL: *https://doi.org/10.1021/ja01269a023*, doi:*10.1021/ja01269a023*.

[15] Cavani, F., Trifirò, F., Vaccari, A., 1991. Hydrotalcite-type anionic clays: Preparation, properties and applications. Catalysis Today 11, 173–301. URL: *https://www.sciencedirect.com/science/article/pii/092058619180068K*, doi:*https://doi.org/10.1016/0920-5861(91)80068-K*.

[16] Cheah, K.W., Taylor, M.J., Evans, G., Samson, A., Skoulou, V., 2022. Chapter 1 - overview of biomass conversion to biofuels, in: Yusup, S., Rashidi, N.A. (Eds.), Value-Chain of Biofuels. Elsevier, pp. 1–48. URL: *https://www.sciencedirect.com/science/article/pii/B9780128243886000075*, doi:*https://doi.org/10.1016/B978-0-12-824388-6.00007-5*.

[17] Chen, D., Christensen, K.O., Ochoa-Fernández, E., Yu, Z., Tøtdal, B., Latorre, N., Monzón, A., Holmen, A., 2005. Synthesis of carbon nanofibers: effects of ni crystal size during methane decomposition. Journal of Catalysis 229, 82–96. URL: *https://www.sciencedirect.com/science/article/pii/S002195170400507X*, doi:*https://doi.org/10.1016/j.jcat.2004.10.017*.

[18] Christensen, K., Chen, D., Lødeng, R., Holmen, A., 2006. Effect of supports and ni crystal size on carbon formation and sintering during steam methane reforming. Applied Catalysis A: General 314, 9–22. URL: *https://www.sciencedirect.com/science/article/pii/S0926860X06005813*, doi:*https://doi.org/10.1016/j.apcata.2006.07.028*.

[19] Contreras, J., Figueroa, A., Zeifert, B., Salmones, J., Fuentes, G., Vazquez, T., Angeles, D., Nuño, L., 2020. Production of hydrogen by ethanol steam reforming using ni–co-ex-hydrotalcite catalysts stabilized with tungsten oxides. International Journal of Hydrogen Energy 46. doi:*10.1016/j.ijhydene.2020.11.143*.

[20] Cruz, I.F., Freire, C., Araújo, J.P., Pereira, C., Pereira, A.M., 2018. Chapter 3 - multifunctional ferrite nanoparticles: From current trends toward the future, in: El-Gendy, A.A., Barandiarán, J.M., Hadimani, R.L. (Eds.), Magnetic Nanostructured Materials. Elsevier. Micro and Nano Technologies, pp. 59–116. URL: *https://www.sciencedirect.com/science/article/pii/B9780128139042000036*, doi:*https://doi.org/10.1016/B978-0-12-813904-2.00003-6*.

[21] Dam, A.H., . Bimetallic catalyst system for steam reforming URL: *http://hdl.handle.net/11250/2372764*.

[22] Fahim, M.A., Alsahhaf, T.A., Elkilani, A., 2010. Chapter 11 - hydrogen production, in: Fahim, M.A., Alsahhaf, T.A., Elkilani, A. (Eds.), Fundamentals of Petroleum Refining. Elsevier, Amsterdam, pp. 285–302. URL: *https://www.sciencedirect.com/science/article/pii/B9780444527851000115*, doi:*https://doi.org/10.1016/B978-0-444-52785-1.00011-5*.

[23] Font Palma, C., 2013. Model for biomass gasification including tar formation and evolution. Energy & Fuels 27, 2693–2702. URL: *https://doi.org/10.1021/ef4004297*, doi:*10.1021/ef4004297*.

[24] Furusawa, T., Tsutsumi, A., 2005. Comparison of co/mgo and ni/mgo catalysts for the steam reforming of naphthalene as a model compound of tar derived from biomass gasification. Applied Catalysis A: General 278, 207–212. URL: *https://www.sciencedirect.com/science/article/pii/S0926860X04008099*, doi:*https://doi.org/10.1016/j.apcata.2004.09.035*.

[25] Gao, N., Salisu, J., Quan, C., Williams, P., 2021. Modified nickel-based catalysts for improved steam reforming of biomass tar: A critical review. Renewable and Sustainable Energy Reviews 145, 111023. URL: *https://www.sciencedirect.com/science/article/pii/S1364032121003130*, doi:*https://doi.org/10.1016/j.rser.2021.111023*.

[26] Grenoble, D., Estadt, M., Ollis, D., 1981. The chemistry and catalysis of the water gas shift reaction: 1. the kinetics over supported metal catalysts. Journal of Catalysis 67, 90–102. URL: *https://www.sciencedirect.com/science/article/pii/0021951781902633*, doi:*https://doi.org/10.1016/0021-9517(81)90263-3*.

[27] Guan, G., Kaewpanha, M., Hao, X., Abudula, A., 2016. Catalytic steam reforming of biomass tar: Prospects and challenges. Renewable and Sustainable Energy Reviews 58, 450–461. URL: *https://www.sciencedirect.com/science/article/pii/S1364032115016998*, doi:*https://doi.org/10.1016/j.rser.2015.12.316*.

[28] He, L., Berntsen, H., Ochoa-Fernández, E., Walmsley, J., Blekkan, E., Chen, D., 2009. Co–ni catalysts derived from hydrotalcite-like materials for hydrogen production by ethanol steam reforming. Topics in Catalysis 52, 206–217. doi:*10.1007/s11244-008-9157-1*.

[29] He, L., Yang, J., Chen, D., 2013. Chapter 6 - hydrogen from biomass: Advances in thermochemical processes, in: Gandía, L.M., Arzamendi, G., Diéguez, P.M. (Eds.), Renewable Hydrogen Technologies. Elsevier, Amsterdam, pp. 111–133. URL: *https://www.sciencedirect.com/science/article/pii/B9780444563521000064*, doi:*https://doi.org/10.1016/B978-0-444-56352-1.00006-4*.

[30] Hirst, D., 2020. The history of global climate change negotiations. House of commons Library URL: *https://commonslibrary.parliament.uk/the-history-of-global-climate-change-negotiations/*.

[31] Huber, G.W., Iborra, S., Corma, A., 2006. Synthesis of transportation fuels from biomass: Chemistry, catalysts, and engineering. Chemical Reviews 106, 4044–4098. URL: *https://doi.org/10.1021/cr068360d*, doi:*10.1021/cr068360d*. pMID: 16967928.

[32] J.A Moulijn, M.M., 2014. Chemical process technology, second edition. Organic Process Research & Development 18, 1153–1153. URL: *https://doi.org/10.1021/op500256y*, doi:*10.1021/op500256y*.

[33] Jacobs, G., Das, T.K., Li, J., Luo, M., Patterson, P.M., Davis, B.H., 2007. Fischer-tropsch synthesis: Influence of support on the impact of co-fed water for cobalt-based catalysts, in: Davis, B., Occelli, M. (Eds.), Fischer-Tropsch Synthesis, Catalyst and Catalysis. Elsevier. volume 163 of *Studies in Surface Science and Catalysis*, pp. 217–253. URL: *https://www.sciencedirect.com/science/article/pii/S0167299107804812*, doi:*https://doi.org/10.1016/S0167-2991(07)80481-2*.

[34] James, O., Maity, S., 2016. Temperature programme reduction (tpr) studies of cobalt phases in -alumina supported cobalt catalysts. Journal of Petroleum Technology and Alternative Fuels 7, 1–12. doi:*10.5897/JPTAF2015.0122*.

[35] Koehle, M., Mhadeshwar, A., 2013. Chapter 3 - nanoparticle catalysis for reforming of biomass-derived fuels, in: Suib, S.L. (Ed.), New and Future Developments in Catalysis. Elsevier, Amsterdam, pp. 63–93. URL: *https://www.sciencedirect.com/science/article/pii/B9780444538741000032*, doi:*https://doi.org/10.1016/B978-0-444-53874-1.00003-2*.

[36] Krumeich, F., 2023. Characterization of catalysts and surfaces, characterization techniques in heterogeneous catalysis. Eidgenössische Technische Hochschule Zürich .

[37] Li, C., Chen, Y.W., 1995. Temperature-programmed-reduction studies of nickel oxide/alumina catalysts: effects of the preparation method. Thermochimica Acta 256, 457–465. URL: *https://www.sciencedirect.com/science/article/pii/004060319402177P*, doi:*https://doi.org/10.1016/0040-6031(94)02177-P*.

[38] Linnerud, M., 2022. Ntnu nanolab s(t)em introduction course. NTNU Nanolab .

[39] Liska, M., Wilson, A., Bensted, J., 2019. 13 - special cements, in: Hewlett, P.C., Liska, M. (Eds.), Lea's Chemistry of Cement and Concrete (Fifth Edition). fifth edition ed.. Butterworth-Heinemann, pp. 585–640. URL: *https://www.sciencedirect.com/science/article/pii/B9780081007730000137*, doi:*https://doi.org/10.1016/B978-0-08-100773-0.00013-7*.

[40] Lysne, A., Madsen, K.O., Antony, J., Rout, K.R., Blekkan, E.A., 2022. Effects of ni-co ratio on deactivation and coke formation in steam reforming of hydrocarbon impurities from biomass gasification with ni-co/mg(al)o catalysts. Chemical Engineering Transactions 92, 37–42. URL: *https://www.cetjournal.it/index.php/cet/article/view/CET2292007*, doi:*10.3303/CET2292007*.

[41] Øxnevad Madsen, K., 2021. Catalytic steam reforming of hydrocarbon impurities from biomass gasification. NTNU .

[42] Meloni, E., Martino, M., Palma, V., 2020. A short review on ni based catalysts and related engineering issues for methane steam reforming. Catalysts 10. URL: *https://www.mdpi.com/2073-4344/10/3/352*, doi:*10.3390/catal10030352*.

[43] Milne, T.A., Evans, R.J., Abatzaglou, N., 1998. Biomass gasifier "tars": Their nature, formation, and conversion URL: *https://www.osti.gov/biblio/3726*, doi:*10.2172/3726*.

[44] Moulijn, J., van Leeuwen, P., van Santen, R., 1993. Chapter 11 temperature programmed reduction and sulphiding, in: Catalysis. Elsevier. volume 79 of *Studies in Surface Science and Catalysis*, pp. 401–417. URL: *https://www.sciencedirect.com/science/article/pii/S016729910863815X*, doi:*https://doi.org/10.1016/S0167-2991(08)63815-X*.

[45] Munasinghe, P.C., Khanal, S.K., 2011. Chapter 4 - biomass-derived syngas fermentation into biofuels, in: Pandey, A., Larroche, C., Ricke, S.C., Dussap, C.G., Gnansounou, E. (Eds.), Biofuels. Academic Press, Amsterdam, pp. 79–98. URL: *https://www.sciencedirect.com/science/article/pii/B9780123850997000048*, doi:*https://doi.org/10.1016/B978-0-12-385099-7.00004-8*.

[46] Ochoa-Fernández, E., Lacalle-Vilà, C., Christensen, K., Walmsley, J., Rønning, M., Holmen, A., Chen, D., 2007. Ni catalysts for sorption enhanced steam methane reforming. Topics in Catalysis 45, 3–8. doi:*10.1007/s11244-007-0231-x*.

[47] Ostadi, M., Rytter, E., Hillestad, M., 2019. Boosting carbon efficiency of the biomass to liquid process with hydrogen from power: The effect of h2/co ratio to the fischer-tropsch reactors on the production and power consumption. Biomass and Bioenergy 127, 105282. URL: *https://www.sciencedirect.com/science/article/pii/S0961953419302314*, doi:*https://doi.org/10.1016/j.biombioe.2019.105282*.

[48] Phung, T.K., Pham, T.L.M., Nguyen, A.N.T., Vu, K.B., Giang, H.N., Nguyen, T.A., Huynh, T.C., Pham, H.D., . Effect of supports and promoters on the performance of ni-based catalysts in ethanol steam reforming. Chemical Engineering & Technology 43, 672–688. URL: *https://onlinelibrary.wiley.com/doi/abs/10.1002/ceat.201900445*, doi:*https://doi.org/10.1002/ceat.201900445*.

[49] Profeti, L.P., Dias, J.A., Assaf, J.M., Assaf, E.M., 2009. Hydrogen production by steam reforming of ethanol over ni-based catalysts promoted with noble metals. Journal of Power Sources 190, 525–533. URL: *https://www.sciencedirect.com/science/article/pii/S0378775308025019*, doi:*https://doi.org/10.1016/j.jpowsour.2008.12.104*.

[50] Qi, Y., Cheng, Z., Zhou, Z., 2015. Steam reforming of methane over ni catalysts prepared from hydrotalcite-type precursors: Catalytic activity and reaction kinetics. Chinese Journal of Chemical Engineering 23, 76–85. URL: *https://www.sciencedirect.com/science/article/pii/S1004954114002146*, doi:*https://doi.org/10.1016/j.cjche.2013.11.002*.

[51] Rostrup-Nielsen, J., Hansen, J.B., 2011. Chapter 4 - steam reforming for fuel cells, in: Shekhawat, D., Spivey, J.J., Berry, D.A. (Eds.), Fuel Cells: Technologies for Fuel Processing. Elsevier, Amsterdam, pp. 49–71. URL: *https://www.sciencedirect.com/science/article/pii/B9780444535634100045*, doi:*https://doi.org/10.1016/B978-0-444-53563-4.10004-5*.

[52] Salomão, R., Milena, L., Wakamatsu, M., Pandolfelli, V., 2011. Hydrotalcite synthesis via co-precipitation reactions using mgo and al(oh) 3 precursors. Ceramics International - CERAM INT 37, 3063–3070. doi:*10.1016/j.ceramint.2011.05.034*.

[53] Saxrud, I., 2022. Catalysts for syngas conditioning for advanced biofuels. NTNU, Specialisation project URL: *https://eprints.soton.ac.uk/352803/*.

[54] Schwarz, J.A., Contescu, C., Contescu, A., 1995. Methods for preparation of catalytic materials. Chemical Reviews 95, 477–510. URL: *https://doi.org/10.1021/cr00035a002*, doi:*10.1021/cr00035a002*.

[55] Seemann, M., Thunman, H., 2019. 9 - methane synthesis, in: Materazzi, M., Foscolo, P.U. (Eds.), Substitute Natural Gas from Waste. Academic Press, pp. 221–243. URL: *https://www.sciencedirect.com/science/article/pii/B978012815554700009X*, doi:*https://doi.org/10.1016/B978-0-12-815554-7.00009-X*.

[56] Sehested, J., 2006. Four challenges for nickel steam-reforming catalysts. Catalysis Today 111, 103–110. URL: *https://www.sciencedirect.com/science/article/pii/S092058610500708X*, doi:*https://doi.org/10.1016/j.cattod.2005.10.002*. frontiers in Catalysis: A Molecular View of Industrial Catalysis.

[57] Sietsma, J.R., Jos van Dillen, A., de Jongh, P.E., de Jong, K.P., 2006. Application of ordered mesoporous materials as model supports to study catalyst preparation by impregnation and drying, in: Gaigneaux, E., Devillers, M., De Vos, D., Hermans, S., Jacobs, P., Martens, J., Ruiz, P. (Eds.), Scientific Bases for the Preparation of Heterogeneous Catalysts. Elsevier. volume 162 of *Studies in Surface Science and Catalysis*, pp. 95–102. URL: *https://www.sciencedirect.com/science/article/pii/S0167299106808955*, doi:*https://doi.org/10.1016/S0167-2991(06)80895-5*.

[58] Sikander, U., Sufian, S., Salam, M., 2017. A review of hydrotalcite based catalysts for hydrogen production systems. International Journal of Hydrogen Energy 42, 19851–19868. URL: *https://www.sciencedirect.com/science/article/pii/S0360319917324011*, doi:*https://doi.org/10.1016/j.ijhydene.2017.06.089*.

[59] Sing, K.S.W., 1985. Reporting physisorption data for gas/solid systems with special reference to the determination of surface area and porosity (recommendations 1984). Pure and Applied Chemistry 57, 603–619. URL: *https://doi.org/10.1351/pac198557040603*, doi:*doi:10.1351/pac198557040603*.

[60] Speight, J.G., 2011. Chapter 3 - refining chemistry, in: Speight, J.G. (Ed.), The Refinery of the Future. William Andrew Publishing, Boston, pp. 81–116. URL: *https://www.sciencedirect.com/science/article/pii/B9780815520412100037*, doi:*https://doi.org/10.1016/B978-0-8155-2041-2.10003-7*.

[61] Takeguchi, T., Watanabe, H., Murayama, T., Takahashi, H., Ueda, W., 2013. Quantitative analysis of coke formation during steam reforming of methane on a nickel–hydrotalcite catalyst under practical operation conditions. Chemistry Letters 42, 124–126. URL: *https://doi.org/10.1246/cl.2013.124*, doi:*10.1246/cl.2013.124*.

[62] Tarka, A., Zybert, M., Ronduda, H., Patkowski, W., Mierzwa, B., Kępiński, L., Raróg-Pilecka, W., 2022. On optimal barium promoter content in a cobalt catalyst for ammonia synthesis. Catalysts 12. URL: *https://www.mdpi.com/2073-4344/12/2/199*, doi:*10.3390/catal12020199*.

[63] Teter, J., 2022. Transport improving the sustainability of passenger and freight transport, Paris. URL: *https://www.iea.org/topics/transport*.

[64] Thommes, M., Kaneko, K., Neimark, A.V., Olivier, J.P., Rodriguez-Reinoso, F., Rouquerol, J., Sing, K.S., 2015. Physisorption of gases, with special reference to the evaluation of surface area and pore size distribution (iupac technical report). Pure and Applied Chemistry 87, 1051–1069. URL: *https://doi.org/10.1515/pac-2014-1117*, doi:*doi:10.1515/pac-2014-1117*.

[65] Torres, W., Pansare, S.S., Jr., J.G.G., 2007. Hot gas removal of tars, ammonia, and hydrogen sulfide from biomass gasification gas. Catalysis Reviews 49, 407–456. URL: *https://doi.org/10.1080/01614940701375134*, doi:*10.1080/01614940701375134*.

[66] Ulejczyk, B., Jozwik, P., Mlotek, M., Krawczyk, K., 2022. A promising cobalt catalyst for hydrogen production. Catalysts 12. URL: *https://www.mdpi.com/2073-4344/12/3/278*, doi:*10.3390/catal12030278*.

[67] Wu, H., La Parola, V., Pantaleo, G., Puleo, F., Venezia, A.M., Liotta, L.F., 2013. Ni-based catalysts for low temperature methane steam reforming: Recent results on ni-au and comparison with other bi-metallic systems. Catalysts 3, 563–583. URL: *https://www.mdpi.com/2073-4344/3/2/563*, doi:*10.3390/catal3020563*.

[68] Xu, D., Li, W., Duan, H., Ge, Q., Xu, H., 2005. Reaction performance and characterization of co/al2o3 fischer–tropsch catalysts promoted with pt, pd and ru. Catalysis Letters 102, 229–235. doi:*10.1007/s10562-005-5861-7*.

[69] York, A., Xiao, T., Green, M., Claridge, J., 2007. Methane oxyforming for synthesis gas production. Catalysis Reviews - Science and Engineering 49, 511–560. doi:*10.1080/01614940701583315*.

[70] Yousaf, B., 2016. Hydrotalcite based ni-co bi-metallic catalysts for steam reforming of methane. NTNU URL: *http://hdl.handle.net/11250/2419913*.

[71] Zhang, Y., 2020. Preparation of heterogeneous catalysts based on cwao technology. Journal of Physics: Conference Series 1549, 032052. doi:*10.1088/1742-6596/1549/3/032052*.

Appendix

A Catalyst Synthesis

Table 5.1: Details on the materials used for the synthesis.

Material	Chemical formula	Molar mass [g/mol]	Purity [%]	Producer
Nickel nitrate hexahydrate	$Ni(NO_3)_2 \cdot 6H_2O$	290.79	99.99	Sigma Aldrich
Cobalt nitrate hexahydrate	$Co(NO_3)_2 \cdot 6H_2O$	291.03	≥ 98.00	Sigma Aldrich
Magnesium nitrate hexahydrate	$Mg(NO_3)_2 \cdot 6H_2O$	256.41	99.99	Sigma Aldrich
Aluminum nitrate nonahydrate	$Al(NO_3)_3 \cdot 9H_2O$	375.13	≥ 98.00	Sigma Aldrich
Sodium hydroxide	$NaOH$	40.00	≥ 98.00	Sigma Aldrich
Sodium carbonate	$NaCO_3$	105.99	≥ 99.99	Sigma Aldrich

4.3 mL of nitric acid (HNO_3) was used for pH adjustment in the synthesis of the 20-20 wt% Ni-Co catalyst.

An Excel solver was used to calculate the amount of reactants needed for the synthesis of the catalysts. All of the catalysts share the same catalyst basis with different promotions. The criteria below are used to make the catalyst prior to promotion.

$$\frac{Ni + Co}{Ni + Co + MgO + Al_2O_3} = 40[wt\%] \tag{5.1}$$

$$\frac{Mg^{2+} + Co^{2+} + Ni^{2+}}{Al^{3+}} = 3 \tag{5.2}$$

$$\frac{Ni}{Co} = 1 \tag{5.3}$$

Table 5.2: Details on the materials used for catalyst co-precipitation.

Component	Stoichiometric amount [mol]	Calculated amount [g]	Amount added [g]
$Ni(NO_3)_2 \cdot 6H_2O$	0.050	14.6115	14.6119
$Co(NO_3)_2 \cdot 6H_2O$	0.050	14.5640	14.5641
$Mg(NO_3)_2 \cdot 6H_2O$	0.125	31.9670	31.9672
$Al(NO_3)_3 \cdot 9H_2O$	0.075	28.1300	28.1303
$NaOH$	0.600	24.0000	24.0001
$NaCO_3$	0.056	5.9600	5.9597

Table 5.3: Details on the component used in catalyst impregnation.

Component	Purity[a] [%]	Producer
Platinum(IV) nitrate solution	15	Thermo Fisher (Kandel) GmbH
Palladium(II) nitrate dihydrate	40	Merck KGaA
Rhodium(III) nitrate hydrate	36	Sigma Aldrich

[a] Approximate purity of the noble metals in the material [mg]

To obtain a noble metal promotion of 1.0 wt% for the catalysts, an Excel solver was used to calculate the reactants needed for the synthesis. In the context of the impregnation of the catalyst, the pore volume was determined to be 0.5 mL/g. 1.5 grams of 1.0 wt% Pt, Pd, and Rh promoted catalysts were prepared by dissolving the components in DI-water in the quantities given in table (5.4).

Table 5.4: Details on the materials used in catalyst impregnation.

Component	Calculated amount [mg/g]	Concentration[a] [mg/mL]
Platinum(IV) nitrate solution	60.7310	121.4620
Palladium(II) nitrate dihydrate	22.7741	45.5483
Rhodium(III) nitrate hydrate	25.3046	50.6092

[a] Amount of the materials added per mL of DI-water

B Characterisation

Physisorption
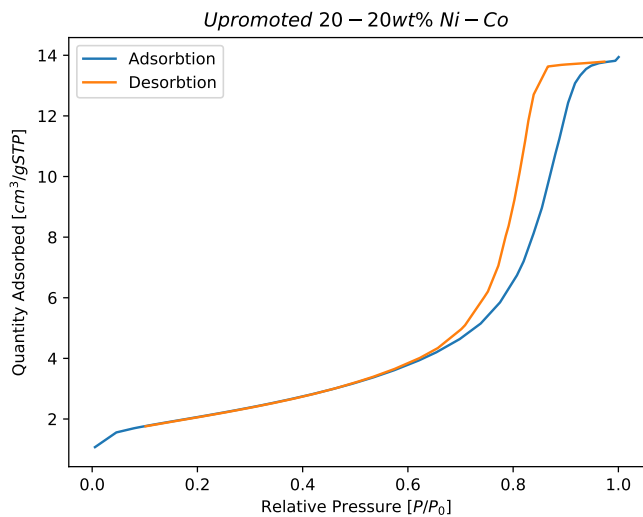
Figure 5.1: N_2 adsorption isotherm obtained from N_2 physisorption for the 20-20 wt% Ni-Co catalyst.
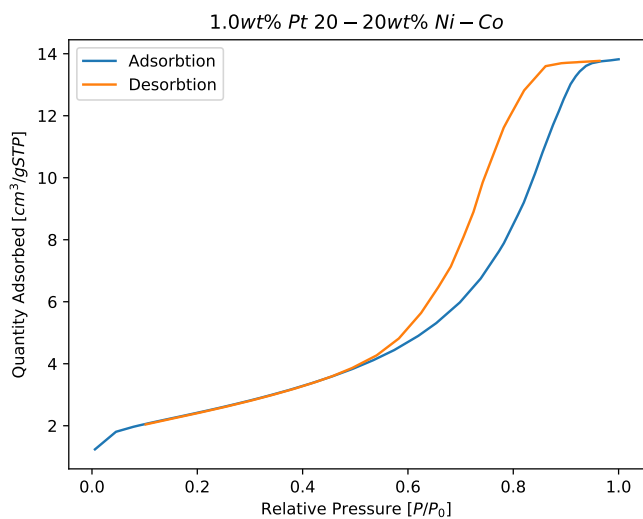
Figure 5.2: N_2 adsorption isotherm obtained from N_2 physisorption for the 1.0wt% Pt/ 20-20 wt% Ni-Co catalyst.
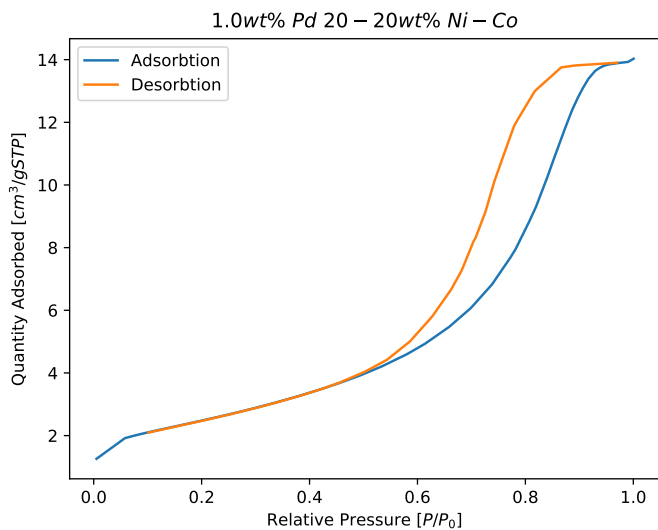
Figure 5.3: N_2 adsorption isotherm obtained from N_2 physisorption for the 1.0wt% Pd/ 20-20 wt% Ni-Co catalyst.
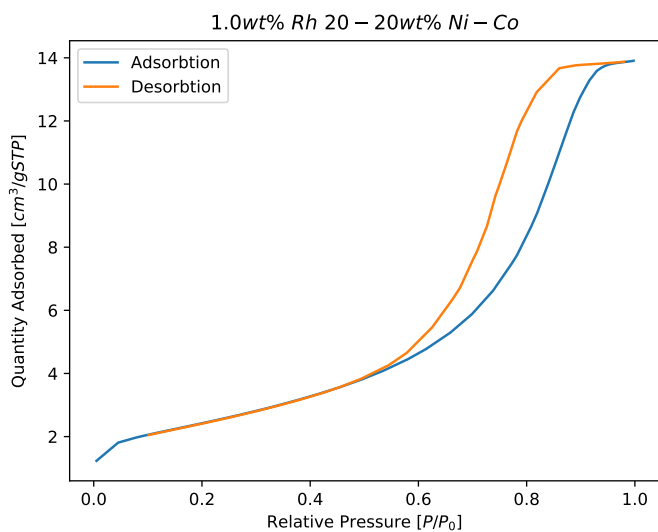
Figure 5.4: N_2 adsorption isotherm obtained from N_2 physisorption for the 1.0wt% Rh/ 20-20 wt% Ni-Co catalyst.

Chemisorption
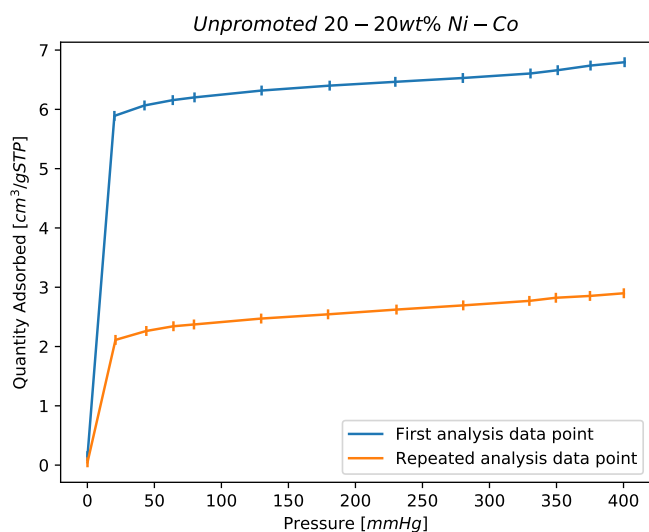
Figure 5.5: H_2 Chemisorption isotherm of the 20-20 wt% Ni-Co catalyst.
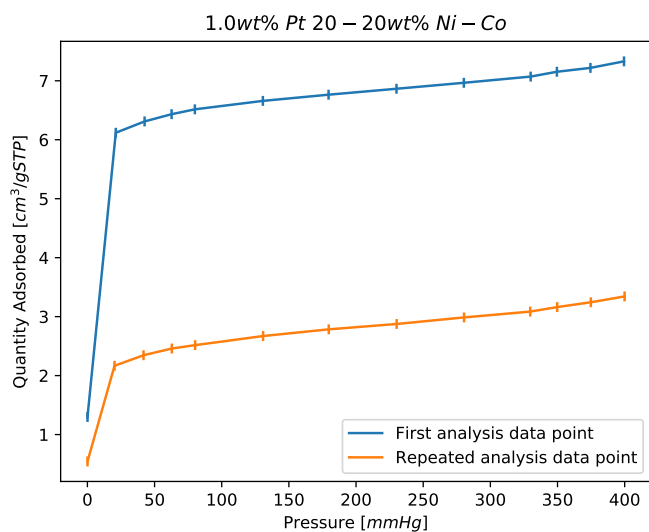
Figure 5.6: H_2 Chemisorption isotherm of the 1.0wt% Pt/ 20-20 wt% Ni-Co catalyst.
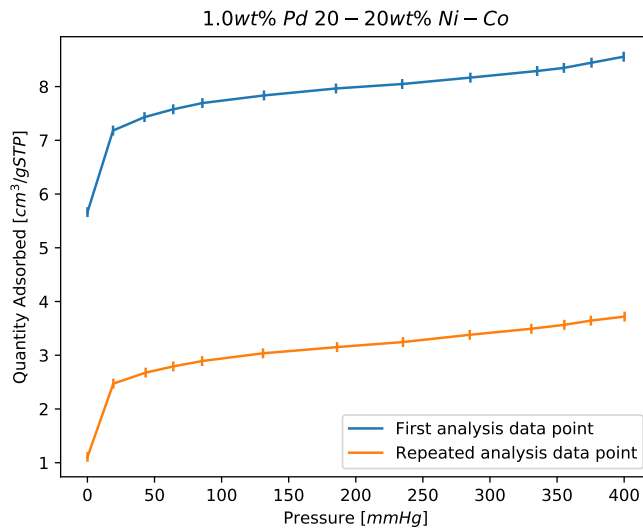
Figure 5.7: H_2 Chemisorption isotherm of the 1.0wt% Pd/ 20-20 wt% Ni-Co catalyst.
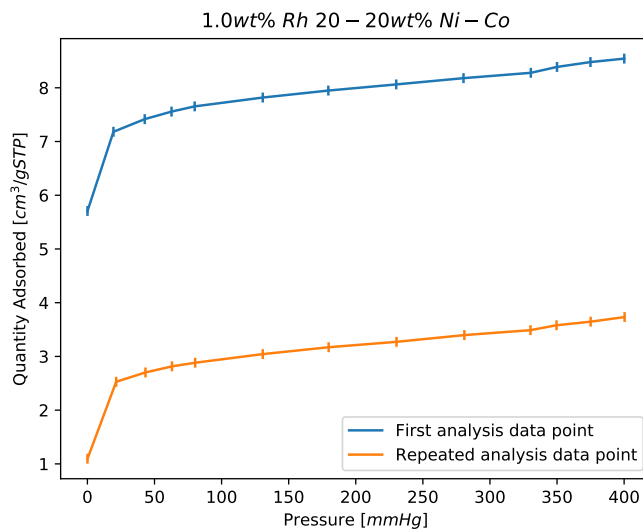
Figure 5.8: H_2 Chemisorption isotherm of the 1.0wt% Rh/ 20-20 wt% Ni-Co catalyst.
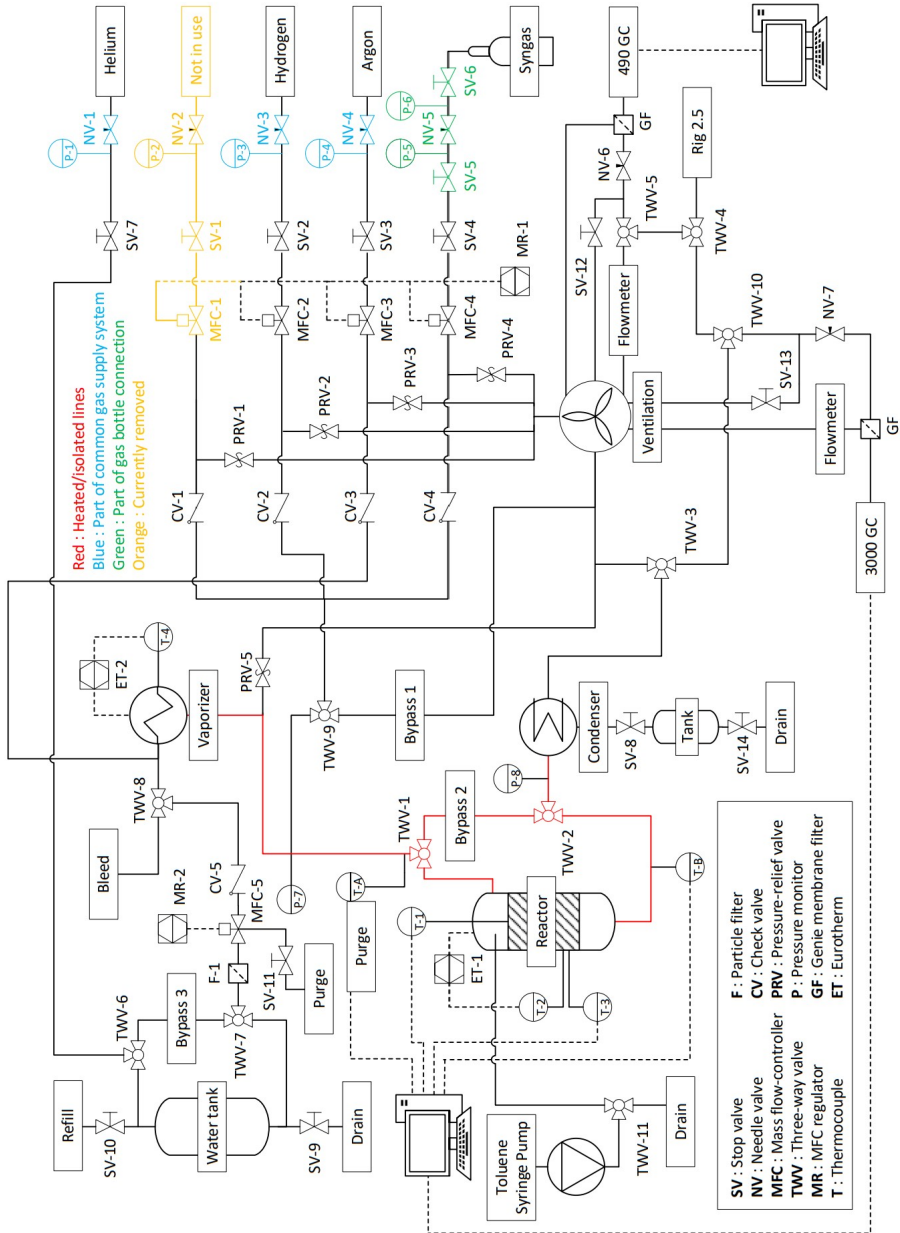
Figure 5.9: Flow sheet of the rig set-up produced by co-supervisor Ask Lysne.

D Activity Experiments

MFC
The mass flow controllers were calibrated by co-supervisor Ask Lysne. The MFC-setpoints corresponding to desired volume flows were determined using the linear functions for the corresponding calibration curves found in figure 5.11.

Micro GC
In order to translate the acquired peak areas obtained from the Micro GC integrations to molar factions the quadratic calibration curves were utilized.

$$A_i = Ax_i^2 + Bx + C$$

(5.4)

A_i is the area for the component from the Micro GC and x_i is the unknown molar fraction. The calibration curves from the Micro GC integration are found in figure 5.10

$$x_i = \frac{-b + \sqrt{b^2 - 4a(c - A_i)}}{2a}$$

(5.5)
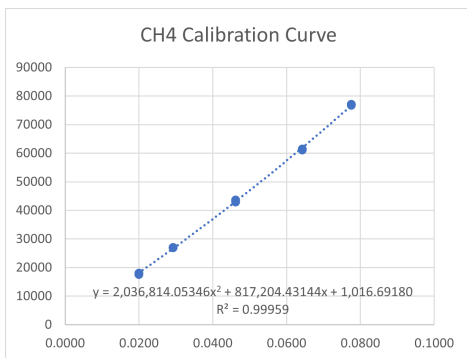
(a)
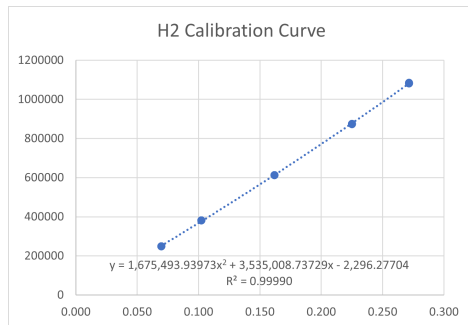
(b)
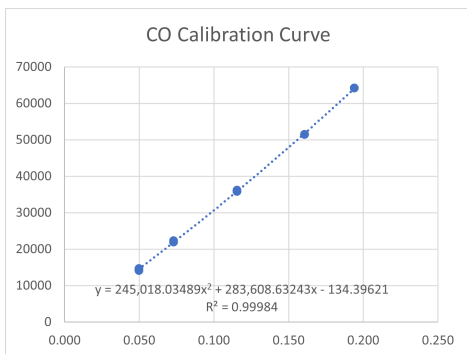
(c)
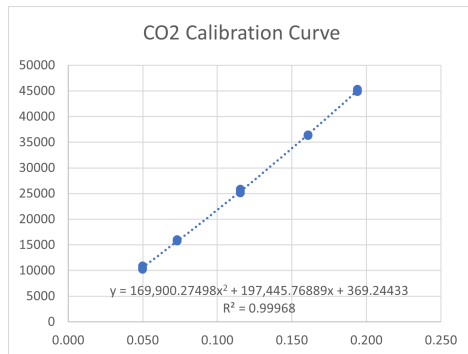
(d)
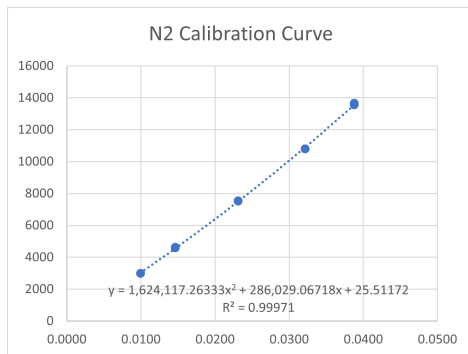
(e)

Figure 5.10: Calibration curves of Micro GC integration.

Calibration curve H2 mass flow controller (MFC-2)

$y = 13.902x - 6.5984$
$R^2 = 0.9996$

(a)

Calibration curve Ar mass flow controller (MFC-3)

$y = 16.14x - 24.432$
$R^2 = 0.9994$

(b)

Calibration curve Syngas mass flow controller (MFC-4)

$y = 27.064x - 14.73$
$R^2 = 1$

(c)

Calibration curve H2O mass flow controller (MFC-5)

$y = 0.0048x + 0.0007$
$R^2 = 1$
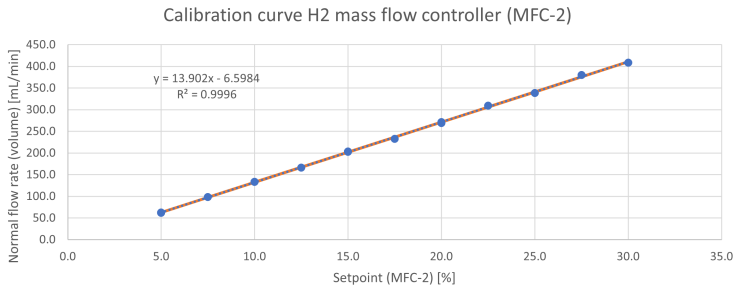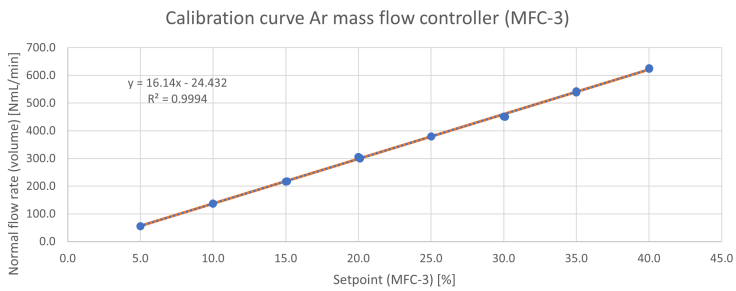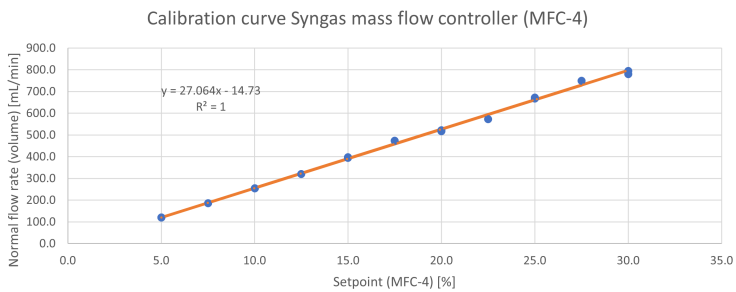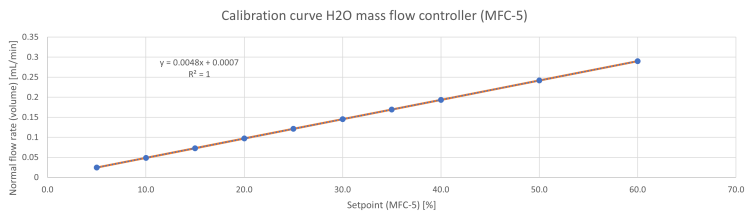
(d)

Figure 5.11: MFC calibration curves.

Molar and volumetric flow rates calculations

After the molar fractions are calculated from the calibration curves from the Micro GC the flowrates can be calculated with the following equation.

$$F_{v,i} = \frac{x_i}{x_{N_2}} \cdot x_{N_2,0} \cdot F_{v,syngas,0} \quad [NmL/min] \tag{5.6}$$

$$\tag{5.7}$$

Nitrogen is used as a reference gas and the equation is based on the molar nitrogen fraction from the GC and the molar fraction from the inlet synthesis gas. $F_{v,i}$ denores the volumertic flow rate out of the reactor and x_i is the molar faction from the GC. A '0' behind these symbols indicates inlet flows.

Using ideal gas law the molar flow rates can be calculated:

$$F_{n,i} = \frac{F_{v,i} \cdot P}{R \cdot T} \quad [mol/min] \tag{5.8}$$

P is 1.013 bar, and T is 293.15 K at standard conditions, and R is the gas constant.

Calculation Example

A calculation example from the attained areas from the Micro GC analysis to the methane conversion is illustrated in this section. The calculation included is for the un-promoted catalyst experiment without the tar model. The methane calculation acquirer the methane molar flow inlet and outlet. The inlet flow is known from the molar concentration in the inlet syngas and the molar outlet flow is calculated from the GC area. For the first analysis point this GC area for methane equals to 29093. The molar faction was obtained with constants from the methane calibration curve and equation (5.5).

$$x_{CH_4} = \frac{-817204.43144 + \sqrt{817204.43144^2 - 4 \cdot 2036814.05346(1016.69180 - 29093)}}{2 \cdot 2036814.05346}$$

(5.9)

The molar fraction of methane was calculated to be 0.0318. The volumetric flow rate is determined by equation (5.7), and therefor the outlet molar fraction of N_2 was also calculated using equation (5.5) and the nitrogen GC calibration curve to be 0.0252. The inlet flow of nitrogen is known from the molar consentration of nitrogen in the inlet syngas and the total inlet flow.

$$F_{v,CH_4} = \frac{0.0318}{0.0252} \cdot 0.0501 \cdot 399.34 = 25.237 \quad [NmL/min]$$

(5.10)

(5.11)

The molar flow rate of methane was then calculated using equation (5.8):

$$F_{n,CH_4} = \frac{1.1013 \cdot 25.237}{83.1446 \cdot 293.15} = 0.00114 \quad [mol/min]$$

(5.12)

The inlet methane flow flow was then calculated using the molar methane concentration in the syngas and the inlet flow rate of syngas.

$$F_{v,CH_4,0} = 0.0999 \cdot 399.34 = 39.894 \quad [NmL/min]$$

(5.13)

(5.14)

The inlet molar flow rate of methane was then calculated:

$$F_{n,CH_4,0} = \frac{1.1013 \cdot 39.894}{83.1446 \cdot 293.15} = 0.00180 \quad [mol/min]$$

(5.15)

The information need for the methane conversion in the first analysis point is now known and can be calculated using equation 2.22.

$$x_{CH_4} = \frac{0.00180 - 0.00114}{0.00180} = 0.367 \quad [mol/min]$$

(5.16)

The first incjected sample in the stream reforming experiment to the GC gave a methane conversion of 36.7%, and the other calculated parameters in the activation analysis can be found the same calculation method.

E Risk Assessment

ID	49826		**Status**	**Dato**
Risikoområde	Risikovurdering: Helse, miljø og sikkerhet (HMS)		Opprettet	19.08.2022
Opprettet av	Ida Saxrud		Vurdering startet	23.08.2022
Ansvarlig	Ida Saxrud		Tiltak besluttet	
			Avsluttet	

Risikovurdering:
CAT, Student, 2022, Ida Saxrud

Gyldig i perioden:
8/19/2022 - 8/19/2025

Sted:
IKP, K5-317, Kjemihallen D 1.- 2. etasje

Mål / hensikt
Risk assessment for task related to master project fall 2022 and spring 2023.

Bakgrunn
Catalysts for Syngas Conditioning for Advanced Biofuels with supervisors Edd A. Blekkan, Kumar R. Rout and Ask Lysne. The task may include synthesis of Ni-Co/Mg(Al)O catalysts, promotion with Pt, Pd and Rh, characterization of fresh catalysts, and characterization of coke formation in spent catalyst samples.

The following materials may be applied:
$Co(NO_3)_2.6H_2O$, $Ni(NO_3)_2.6H_2O$, $Mg(NO_3)_2.6H_2O$, $Al(NO_3)_2.9H_2O$, Palladium(II) nitrate dihydrate (40% Pd basis), Rhodium(III) nitrate hydrate (36% Rh basis), Platinum(IV) nitrate solution (15% Pt basis), NaOH, Na_2CO_3, HNO_3, toluene, 1-methylnaphthalene and phenol.

Synthesis methods/tools:
Co-precipitation, incipient-wetness-impregnation, drying and calcination.

Characterization techniques:
N_2-physisorption, H_2-chemisorption and TPR will be applied for fresh catalyst characterization.
XRD, XRF and/or ICP-MS may be applied for fresh catalyst characterization.
MP-AES for element analysis.
STEM/EDS (HSE training in NanoLab), TGA-TPO and/or Raman spectroscopy may be applied for coke characterization.

Catalyst activity and stability tests:
Activity and stability measurements will be performed in rig 2.4 in Chemistry Hall D2 (training will be provided by PhD student Ask Lysne).
Catalyst performance will be test with and without tar model (toluene, 1-methylnaphthalene and/or phenol) presence.
Key operating conditions are listed below.

Beskrivelse og avgrensninger

Catalyst synthesis risk parameters:
Chemicals: H350i found in both Co(NO3)2.6H2O and Ni(NO3)2.6H2O. Will register in Eco Exposure, as well as take precautions when handling these materials.
Calcination furnace: High temperature - skin burns
Co-precipitation: Heating - exposed to high temp - skin burns

Characterisation method risk parameters:
XRD/XRF: May be exposed to X-ray radiation.
N2-physisorption: Low temp -196 degrees C. Samples outgassed overnight at 100 degrees C.
TPR: Gas-phase quarts reactor. Use of H2/Ar = 7/93 at flow rate 50mL/min and heating from 10 up to 900 degrees C.
H2-chemisorption: Sample reduced in a 5% H2/He flow at 670 degrees C.
MP-AES: Use of acids (HCl, HNO3) to dissolve the sample. Vaporized acid.

Ris 2.4 experiment risk parameters:
Temperatures: 650-800 degrees C
Pressure: Atmospheric
Gases: Model syngas (CH4, H2, CO, CO2 and N2), He, H2 and Ar
Tar model: Toluene, Phenol and/or 1-Methylnaphthalene

Forutsetninger, antakelser og forenklinger

Assume that analysis is approved and risk assessed separate. Same assumption for rig.

No specific risk related to magnesium(II) and aluminum(II) nitrate.

1) Switch off procedure for rig 2.4:
D.1) Experiment shut-down:
1. Stop the micro-GC data acquisition.
2. Stop PC reaction temperature logging.
3. Set MFC-4 (Syngas) to 0%.
4. Set MFC-5 (Water) to 0%.
5. Note the ending time for the experiment.
6. Close SV-6, SV-5 and SV-4 (Syngas) completely.
7. Set TWV-8 to direct the water flow to the bleed.
8. Set MFC-3 (Argon) to 50%.
9. Stop the reactor heating furnace temperature program.
10. Stop the vaporizer heating furnace temperature program.
11. Turn off the heat-tape controller.
12. Purge the system with argon for 10 min.
13. Set TWV-1 and TWV-2 to direct the flow through the reactor bypass.
14. Purge the system with argon for 5 min.
15. Set TWV-1 and TWV-2 to direct the flow through the reactor.
16. Set TWV-3 to direct the flow to ventilation.
17. Purge the system with argon for 10 min.
18. Set MFC-3 (Argon) to 0%.
19. Close SV-3 (Argon) completely.
20. Close SV-7 (Helium) completely.
21. Load the micro-GC resting method.
22. Shut down the heat furnace controllers.
23. Wait for the system to cool down overnight (leave the cooling water-bath running).
24. Set the rig status to no experiment running.

D.2) Post-shut-down measures (day 3):
1. Stop the cooling water-bath.
2. Close TWV-6 and TWV-7 and release the water tank pressure by opening SV-10.
3. Close SV-9 and SV-10 completely.
4. Drain the condenser through SV-8.
5. Note the amount of water collected.
6. Disconnect the reactor inlet and outlet from the system.
7. Keep the spent catalyst in a (well labeled) vial.
8. Clean the reactor with tap water.
9. Rinse the reactor with DI-water and acetone and leave to dry overnight.

E.1)
In case of small leakage, turn of syngas/H2 supply, stop syringe pump, purge system with Argon, shut down heating furnace x2, and leave cooling-water running.
In case of larger leakage, rig power may be cut by pressing red button.
In case of fire, act according to standard procedures.

Vedlegg

Aluminiumnitrat nonahydrat.pdf
NATRIUMHYDROKSID 0,1N NORMADOSE.pdf
Flow Sheet.pdf
Karbonmonoksid.pdf
Toluen.pdf
nikkel(II)nitrat heksahydrat.pdf
Magnesiumnitrat heksahydrat.pdf
Salpetersyre 4 M.pdf
Natriumkarbonat.pdf
KOBOLT(II)NITRAT 6-HYDRAT.pdf
Fenol.pdf
1-Methylnaphthalene.pdf
Palladium(II)nitrat dihydrat.pdf
Platinum(IV) nitrate, solution.pdf
Rhodium(III) nitrate hydrate.pdf
helium.pdf
Hydrogen.pdf
metan.pdf
oksygen.pdf
Nitrogen.pdf
Aceton.pdf
Argon.pdf
Salpetersyre 65%.pdf
HCl Acid 36%.pdf

Referanser

[Ingen registreringer]

Oppsummering, resultat og endelig vurdering

I oppsummeringen presenteres en oversikt over farer og uønskede hendelser, samt resultat for det enkelte konsekvensområdet.

Farekilde:	**Catalyst synthesis**

Uønsket hendelse: **Spill of nickel nitrate hexahydrate when weighting sample**

Konsekvensområde:	Helse	Risiko før tiltak: 🟡 Risiko etter tiltak: ⚪
	Ytre miljø	Risiko før tiltak: 🟢 Risiko etter tiltak: ⚪
	Materielle verdier	Risiko før tiltak: 🟢 Risiko etter tiltak: ⚪

Uønsket hendelse: **Spill of cobalt nitrate hexahydrate when weighting sample**

Konsekvensområde:	Helse	Risiko før tiltak: 🟡 Risiko etter tiltak: ⚪
	Ytre miljø	Risiko før tiltak: 🟡 Risiko etter tiltak: ⚪

Uønsket hendelse: **Spill of nitric acid (HNO3)**

Konsekvensområde:	Helse	Risiko før tiltak: 🟢 Risiko etter tiltak: ⚪
	Materielle verdier	Risiko før tiltak: 🟢 Risiko etter tiltak: ⚪

Uønsket hendelse: **Spill of sodium hydroxide (NaOH)**

Konsekvensområde:	Helse	Risiko før tiltak: 🟢 Risiko etter tiltak: ⚪
	Materielle verdier	Risiko før tiltak: 🟢 Risiko etter tiltak: ⚪

Uønsket hendelse: **Spill of sodium carbonate (Na2CO3)**

Konsekvensområde:	Helse	Risiko før tiltak: 🟢 Risiko etter tiltak: ⚪

Uønsket hendelse: **Spill of magnesium nitrate hexahydrate when weighting sample**

Konsekvensområde:	Helse	Risiko før tiltak: 🟢 Risiko etter tiltak: ⚪
	Materielle verdier	Risiko før tiltak: 🟢 Risiko etter tiltak: ⚪

Uønsket hendelse: **Spill of aluminium nitrate nonahydrate when weighting sample**

Konsekvensområde:	Helse	Risiko før tiltak: 🟢 Risiko etter tiltak: ⚪
	Materielle verdier	Risiko før tiltak: 🟢 Risiko etter tiltak: ⚪

Farekilde:	**Catalyst synthesis**

Uønsket hendelse:	**Spill of palladium(II) nitrate dihydrate when weighting sample**

Konsekvensområde: Helse   Risiko før tiltak: 🟢 Risiko etter tiltak: ⚪
Ytre miljø   Risiko før tiltak: 🟢 Risiko etter tiltak: ⚪
Materielle verdier   Risiko før tiltak: 🟢 Risiko etter tiltak: ⚪

Uønsket hendelse:	**Spill of rhodium(III) nitrate hydrate when weighting sample**

Konsekvensområde: Helse   Risiko før tiltak: 🟢 Risiko etter tiltak: ⚪
Materielle verdier   Risiko før tiltak: 🟢 Risiko etter tiltak: ⚪

Uønsket hendelse:	**Spill of platinum(IV) nitrate, solution**

Konsekvensområde: Helse   Risiko før tiltak: 🟡 Risiko etter tiltak: ⚪
Materielle verdier   Risiko før tiltak: 🟢 Risiko etter tiltak: ⚪

Farekilde:	**Waste handling and cleaning**

Uønsket hendelse:	**Acetone for cleaning - spillage**

Konsekvensområde: Helse   Risiko før tiltak: 🟢 Risiko etter tiltak: ⚪
Ytre miljø   Risiko før tiltak: 🟢 Risiko etter tiltak: ⚪
Materielle verdier   Risiko før tiltak: 🟢 Risiko etter tiltak: ⚪

Farekilde:	**Calcination furnace**

Uønsket hendelse:	**Skin burns**

Konsekvensområde: Helse   Risiko før tiltak: 🟢 Risiko etter tiltak: ⚪

Uønsket hendelse:	**Electric shock**

Konsekvensområde: Helse   Risiko før tiltak: 🟢 Risiko etter tiltak: ⚪
Ytre miljø   Risiko før tiltak: 🟢 Risiko etter tiltak: ⚪
Materielle verdier   Risiko før tiltak: 🟢 Risiko etter tiltak: ⚪

Uønsket hendelse:	**Uncontrolled heating**

Konsekvensområde: Helse   Risiko før tiltak: 🟢 Risiko etter tiltak: ⚪
Ytre miljø   Risiko før tiltak: 🟢 Risiko etter tiltak: ⚪

Farekilde:	**Calcination furnace**

Uønsket hendelse:	**Uncontrolled heating**

Materielle verdier   Risiko før tiltak: 🟢 Risiko etter tiltak: ⚪

Uønsket hendelse:	**Fire**

Konsekvensområde: Helse   Risiko før tiltak: 🟢 Risiko etter tiltak: ⚪
Ytre miljø   Risiko før tiltak: 🟢 Risiko etter tiltak: ⚪
Materielle verdier   Risiko før tiltak: 🟢 Risiko etter tiltak: ⚪

Farekilde:	**Use of compressed gases (He, Ar)**

Uønsket hendelse:	**Uncontrolled expansion and depletion of O2**

Konsekvensområde: Helse   Risiko før tiltak: 🟢 Risiko etter tiltak: ⚪
Ytre miljø   Risiko før tiltak: 🟢 Risiko etter tiltak: ⚪
Materielle verdier   Risiko før tiltak: 🟢 Risiko etter tiltak: ⚪

Uønsket hendelse:	**Gas leakage**

Konsekvensområde: Helse   Risiko før tiltak: 🟢 Risiko etter tiltak: ⚪
Ytre miljø   Risiko før tiltak: 🟡 Risiko etter tiltak: ⚪
Materielle verdier   Risiko før tiltak: 🟢 Risiko etter tiltak: ⚪

Farekilde:	**Use of flammable gases (CH4, H2, CO)**

Uønsket hendelse:	**Fire, explotion**

Konsekvensområde: Helse   Risiko før tiltak: 🟡 Risiko etter tiltak: ⚪
Ytre miljø   Risiko før tiltak: 🟢 Risiko etter tiltak: ⚪
Materielle verdier   Risiko før tiltak: 🟡 Risiko etter tiltak: ⚪
Omdømme   Risiko før tiltak: 🟡 Risiko etter tiltak: ⚪

Farekilde:	**N2 physisorption**

Uønsket hendelse:	**Liquid N2 spill**

Konsekvensområde: Helse   Risiko før tiltak: 🟡 Risiko etter tiltak: ⚪

Farekilde:	**H2 Chemisorption**

Uønsket hendelse:	**Gas leakage**

Konsekvensområde: Helse   Risiko før tiltak: 🟢 Risiko etter tiltak: ⚪
Materielle verdier   Risiko før tiltak: 🟢 Risiko etter tiltak: ⚪

Farekilde:	**TPR**

Uønsket hendelse:	**Gas leakage**

Konsekvensområde: Helse   Risiko før tiltak: 🟢 Risiko etter tiltak: ⚪

Farekilde:	**Use of toxic gases (CO)**

Uønsket hendelse:	**CO leakage**

Konsekvensområde: Helse   Risiko før tiltak: 🟡 Risiko etter tiltak: ⚪

Farekilde:	**Use of Toluene**

Uønsket hendelse:	**Spill of liquid toluene**

Konsekvensområde: Helse   Risiko før tiltak: 🟡 Risiko etter tiltak: ⚪

Farekilde:	**Use of Fenol**

Uønsket hendelse:	**Spill of Fenol**

Konsekvensområde: Helse   Risiko før tiltak: 🟡 Risiko etter tiltak: ⚪

Farekilde:	**Use of 1-Methylnaphthalene**

Uønsket hendelse:	**Spill of 1-Methylnaphthalene**

Konsekvensområde: Helse   Risiko før tiltak: 🟡 Risiko etter tiltak: ⚪
Ytre miljø   Risiko før tiltak: 🟡 Risiko etter tiltak: ⚪

Farekilde:	**MP-AES**

Uønsket hendelse:	**Spill of HNO3**

Konsekvensområde: Helse   Risiko før tiltak: 🟡 Risiko etter tiltak: ⚪
Materielle verdier   Risiko før tiltak: 🟢 Risiko etter tiltak: ⚪

Uønsket hendelse: **Spill of HCl**

Konsekvensområde: Helse   Risiko før tiltak: 🟡 Risiko etter tiltak: ⚪
Materielle verdier   Risiko før tiltak: 🟢 Risiko etter tiltak: ⚪

Endelig vurdering

Involverte enheter og personer

En risikovurdering kan gjelde for en, eller flere enheter i organisasjonen. Denne oversikten presenterer involverte enheter og personell for gjeldende risikovurdering.

Enhet /-er risikovurderingen omfatter

- Institutt for kjemisk prosessteknologi

Deltakere

Edd Anders Blekkan

Ask Lysne

Kumar Ranjan Rout

Lesere

Estelle Marie M. Vanhaecke

Björn Frederik Baumgarten

Mikael Hammer

Samuel K. Regli

Andre involverte/interessenter

[Ingen registreringer]

Følgende akseptkriterier er besluttet for risikoområdet Risikovurdering: Helse, miljø og sikkerhet (HMS):

Helse	Materielle verdier	Omdømme	Ytre miljø

Oversikt over eksisterende, relevante tiltak som er hensyntatt i risikovurderingen

I tabellen under presenteres eksisterende tiltak som er hensyntatt ved vurdering av sannsynlighet og konsekvens for aktuelle uønskede hendelser.

Farekilde	Uønsket hendelse	Tiltak hensyntatt ved vurdering
Catalyst synthesis	Spill of nickel nitrate hexahydrate when weighting sample	Personal measures
	Spill of nickel nitrate hexahydrate when weighting sample	Fume hood
	Spill of nickel nitrate hexahydrate when weighting sample	Sds
	Spill of nickel nitrate hexahydrate when weighting sample	Instrument/method training
	Spill of nickel nitrate hexahydrate when weighting sample	Register in Eco Exposure
	Spill of cobalt nitrate hexahydrate when weighting sample	Personal measures
	Spill of cobalt nitrate hexahydrate when weighting sample	Fume hood
	Spill of cobalt nitrate hexahydrate when weighting sample	Sds
	Spill of cobalt nitrate hexahydrate when weighting sample	Register in Eco Exposure
	Spill of nitric acid (HNO3)	Personal measures
	Spill of nitric acid (HNO3)	Fume hood
	Spill of nitric acid (HNO3)	Sds
	Spill of sodium hydroxide (NaOH)	Personal measures
	Spill of sodium hydroxide (NaOH)	Fume hood
	Spill of sodium hydroxide (NaOH)	Sds
	Spill of sodium carbonate (Na2CO3)	Personal measures
	Spill of sodium carbonate (Na2CO3)	Fume hood
	Spill of sodium carbonate (Na2CO3)	Sds
	Spill of magnesium nitrate hexahydrate when weighting sample	Personal measures
	Spill of magnesium nitrate hexahydrate when weighting sample	Fume hood
	Spill of magnesium nitrate hexahydrate when weighting sample	Sds
	Spill of aluminium nitrate nonahydrate when weighting sample	Personal measures
	Spill of aluminium nitrate nonahydrate when weighting sample	Fume hood
	Spill of aluminium nitrate nonahydrate when weighting sample	Sds
	Spill of palladium(II) nitrate dihydrate when weighting sample	Personal measures
	Spill of palladium(II) nitrate dihydrate when weighting sample	Fume hood

Catalyst synthesis	Spill of palladium(II) nitrate dihydrate when weighting sample	Sds
	Spill of rhodium(III) nitrate hydrate when weighting sample	Personal measures
	Spill of rhodium(III) nitrate hydrate when weighting sample	Fume hood
	Spill of rhodium(III) nitrate hydrate when weighting sample	Sds
	Spill of platinum(IV) nitrate, solution	Personal measures
	Spill of platinum(IV) nitrate, solution	Fume hood
	Spill of platinum(IV) nitrate, solution	Sds
Waste handling and cleaning	Acetone for cleaning - spillage	
Calcination furnace	Skin burns	Personal measures
	Electric shock	Personal measures
	Electric shock	Procedures
	Electric shock	Instrument/method training
	Electric shock	Gas detection
	Electric shock	Apparatus card
	Uncontrolled heating	Personal measures
	Uncontrolled heating	Procedures
	Uncontrolled heating	Instrument/method training
	Uncontrolled heating	Apparatus card
	Fire	Procedures
	Fire	Apparatus card
Use of compressed gases (He, Ar)	Uncontrolled expansion and depletion of O2	Personal measures
	Uncontrolled expansion and depletion of O2	Sds
	Uncontrolled expansion and depletion of O2	Procedures
	Uncontrolled expansion and depletion of O2	Instrument/method training
	Uncontrolled expansion and depletion of O2	Gas detection
	Uncontrolled expansion and depletion of O2	Apparatus card
	Uncontrolled expansion and depletion of O2	Gas leakage test
	Gas leakage	Personal measures
	Gas leakage	Fume hood
	Gas leakage	Sds
	Gas leakage	Procedures
	Gas leakage	Instrument/method training
	Gas leakage	Gas detection
	Gas leakage	Apparatus card
	Gas leakage	Gas leakage test

Use of flammable gases (CH4, H2, CO)	Fire, explotion	Personal measures
	Fire, explotion	Fume hood
	Fire, explotion	Procedures
	Fire, explotion	Instrument/method training
	Fire, explotion	Gas detection
	Fire, explotion	Apparatus card
N2 physisorption	Liquid N2 spill	Personal measures
	Liquid N2 spill	Instrument/method training
H2 Chemisorption	Gas leakage	Personal measures
	Gas leakage	Fume hood
	Gas leakage	Procedures
	Gas leakage	Instrument/method training
	Gas leakage	Gas detection
	Gas leakage	Apparatus card
TPR	Gas leakage	Personal measures
	Gas leakage	Fume hood
	Gas leakage	Procedures
	Gas leakage	Instrument/method training
	Gas leakage	Gas detection
	Gas leakage	Apparatus card
Use of toxic gases (CO)	CO leakage	Personal measures
	CO leakage	Fume hood
	CO leakage	Sds
	CO leakage	Procedures
	CO leakage	Instrument/method training
	CO leakage	Gas detection
	CO leakage	Apparatus card
	CO leakage	Gas leakage test
Use of Toluene	Spill of liquid toluene	Personal measures
	Spill of liquid toluene	Fume hood
	Spill of liquid toluene	Sds
Use of Fenol	Spill of Fenol	Personal measures
	Spill of Fenol	Fume hood
	Spill of Fenol	Sds
Use of 1-Methylnaphthalene	Spill of 1-Methylnaphthalene	Personal measures
	Spill of 1-Methylnaphthalene	Fume hood
	Spill of 1-Methylnaphthalene	Sds
MP-AES	Spill of HNO3	Personal measures
	Spill of HNO3	Fume hood

MP-AES	Spill of HNO3	Sds
	Spill of HCl	Personal measures
	Spill of HCl	Fume hood
	Spill of HCl	Sds

Eksisterende og relevante tiltak med beskrivelse:

Personal measures

Safety goggles mandatory in all laboratories
Lab coat
Gloves (read sds in order to choose the correct gloves)
Gas mask (read sds in order to choose the correct filters)
Filter mask (read sds in order to choose the correct type)

Fume hood

Work inside fume hood when preparing the catalyst.

Sds

[Ingen registreringer]

Procedures

Operation procedure
Instrument manual
Rig checklist

Local exhaust

[Ingen registreringer]

Instrument/method training

[Ingen registreringer]

Gas detection

When working in the rig, there are gas detectors installed, both locally as well as in the ceiling of the hall.
Use work alone gas detector when working alone. Check for gas leaks before starting, first with inert gas.

Previous risk assessment for instruments/methods

[Ingen registreringer]

Apparatus card

[Ingen registreringer]

Gas trolley

[Ingen registreringer]

PPE

[Ingen registreringer]

Ergonomic measures

[Ingen registreringer]

Register in Eco Exposure

Compounds marked with H340, H350 or H350i

Gas leakage test

Pressurizing rig 2.4 with N2 and use gas detection spray to check for leakage. Measuring with a handheld gas detection while N2/H2 runs through the system.

Risikoanalyse med vurdering av sannsynlighet og konsekvens

I denne delen av rapporten presenteres detaljer dokumentasjon av de farer, uønskede hendelser og årsaker som er vurdert. Innledningsvis oppsummeres farer med tilhørende uønskede hendelser som er tatt med i vurderingen.

Følgende farer og uønskede hendelser er vurdert i denne risikovurderingen:

- **Catalyst synthesis**
    - Spill of nickel nitrate hexahydrate when weighting sample
    - Spill of cobalt nitrate hexahydrate when weighting sample
    - Spill of nitric acid (HNO3)
    - Spill of sodium hydroxide (NaOH)
    - Spill of sodium carbonate (Na2CO3)
    - Spill of magnesium nitrate hexahydrate when weighting sample
    - Spill of aluminium nitrate nonahydrate when weighting sample
    - Spill of palladium(II) nitrate dihydrate when weighting sample
    - Spill of rhodium(III) nitrate hydrate when weighting sample
    - Spill of platinum(IV) nitrate, solution
- **Waste handling and cleaning**
    - Acetone for cleaning - spillage
- **Calcination furnace**
    - Skin burns
    - Electric shock
    - Uncontrolled heating
    - Fire
- **Use of compressed gases (He, Ar)**
    - Uncontrolled expansion and depletion of O2
    - Gas leakage
- **Use of flammable gases (CH4, H2, CO)**
    - Fire, explotion
- **N2 physisorption**
    - Liquid N2 spill
- **H2 Chemisorption**
    - Gas leakage
- **TPR**
    - Gas leakage
- **Use of toxic gases (CO)**
    - CO leakage
- **Use of Toluene**
    - Spill of liquid toluene
- **Use of Fenol**
    - Spill of Fenol
- **Use of 1-Methylnaphthalene**
    - Spill of 1-Methylnaphthalene

- **MP-AES**
    - Spill of HNO3
    - Spill of HCl

Detaljert oversikt over farekilder og uønskede hendelser:

Farekilde: Catalyst synthesis

Uønsket hendelse: Spill of nickel nitrate hexahydrate when weighting sample

Årsak: Insufficient ventilation in the fume hood

Årsak: Insufficient ventilation in the fume hood

Sannsynlighet for hendelsen (felles for alle konsekvensområder): **Lite sannsynlig (2)**

Kommentar:

Working inside fume hood with good ventilation, appropriate gloves, goggles and labcoat makes the incident not very likely to happen.

Konsekvensområde: Helse

Risiko:

Vurdert konsekvens: **Svært stor (4)**

Kommentar: H272 May intensify fire; oxidizing.
H302 + H332 Harmful if swallowed or inhaled.
H315 Irritating to skin.
H317 May cause an allergic skin reaction.
H318 Causes serious eye damage.
H334 May cause allergy or asthma symptoms or breathing difficulties inhalation.
H341 Suspected of causing genetic damage.
H350 May cause cancer.
H360 May damage fertility or cause birth defects.
H372 Causes damage to organs through prolonged or repeated exposure by inhalation.
H410 Very toxic, with long-term effects, to aquatic life.H272 May intensify fire; oxidizing.
H302 + H332 Harmful if swallowed or inhaled.
H315 Irritating to skin.
H317 May cause an allergic skin reaction.
H318 Causes serious eye damage.
H334 May cause allergy or asthma symptoms or breathing difficulties inhalation.
H341 Suspected of causing genetic damage.
H350 May cause cancer.
H360 May damage fertility or cause birth defects.
H372 Causes damage to organs through prolonged or repeated exposure by inhalation.
H410 Very toxic, with long-term effects, to aquatic life.

Norges teknisk-naturvitenskapelige universitet (NTNU)

Unntatt offentlighet jf. Offentlighetsloven § 14

Utskriftsdato:

24.05.2023

Utskrift foretatt av:

Ida Saxrud

Side:

18/44

Konsekvensområde: Ytre miljø   *Risiko:*

    Vurdert konsekvens: **Middels (2)**

        Kommentar: Strong oxidizer - may cause fire

Konsekvensområde: Materielle verdier   *Risiko:*

    Vurdert konsekvens: **Middels (2)**

        Kommentar: Oxidizing agent - can amplify fire

Uønsket hendelse: Spill of cobalt nitrate hexahydrate when weighting sample

- -

    Årsak: Insufficient ventilation in fume hood

    Årsak: Inappropriate gloves

Sannsynlighet for hendelsen (felles for alle konsekvensområder): **Lite sannsynlig (2)**

    Kommentar:

Working inside fume hood with good ventilation, nitrile gloves, goggles and labcoat makes the incident not very likely to happen.

Konsekvensområde: Helse   *Risiko:*

    Vurdert konsekvens: **Svært stor (4)**

        Kommentar: H272 May intensify fire; oxidiser
H302 Harmful if swallowed
H317 May cause an allergic skin reaction
H318 Causes serious eye damage
H334 May cause allergy or asthma symptoms or breathing difficulties if inhaled
H341 Suspected of causing genetic defects
H350i May cause cancer by inhalation
H360F May damage fertility
H410 Very toxic to aquatic life with long lasting effects

Konsekvensområde: Ytre miljø   *Risiko:*

    Vurdert konsekvens: **Stor (3)**

        Kommentar: Very harmful for the enviroment.

Uønsket hendelse: Spill of nitric acid (HNO3)

- -

Årsak: Insufficient ventilation in fume hood

Årsak: Inappropriate personal protection

Sannsynlighet for hendelsen (felles for alle konsekvensområder):   **Lite sannsynlig (2)**

> *Kommentar:*
> Use of personal protection such as goggles, neoprene or viton rubber gloves, lab coat and working under a fume hood makes the incident unlikely.

Konsekvensområde: Helse   ***Risiko:***

> *Vurdert konsekvens:* **Middels (2)**

> *Kommentar:* H314 Causes severe burns to skin and eyes.
> H290 May be corrosive to metals.

Konsekvensområde: Materielle verdier   ***Risiko:***

> *Vurdert konsekvens:* **Liten (1)**

> *Kommentar:* Can be corrosive to metals.

Uønsket hendelse: Spill of sodium hydroxide (NaOH)

Årsak: Inappropriate personal protection

Årsak: Insufficient ventilation

Sannsynlighet for hendelsen (felles for alle konsekvensområder): **Lite sannsynlig (2)**

Kommentar:
Working inside fume hood with good ventilation, nitrile gloves, goggles and labcoat makes the incident not very likely to happen.

Konsekvensområde: Helse   *Risiko:*

Vurdert konsekvens: **Middels (2)**

Kommentar: H314 Causes severe burns to skin and eyes.

Konsekvensområde: Materielle verdier   *Risiko:*

Vurdert konsekvens: **Liten (1)**

Kommentar: Can be corrosive for metals

Uønsket hendelse: Spill of sodium carbonate (Na2CO3)

Årsak: Not using safety goggles

Sannsynlighet for hendelsen (felles for alle konsekvensområder): **Svært lite sannsynlig (1)**

Kommentar:
Will always use necessary safety equipment such as goggles in lab so the incident is not very likely to happen

Konsekvensområde: Helse   *Risiko:*

Vurdert konsekvens: **Middels (2)**

Kommentar: H319 Causes serious eye irritation

Uønsket hendelse: Spill of magnesium nitrate hexahydrate when weighting sample
- -

Sannsynlighet for hendelsen (felles for alle konsekvensområder): **Lite sannsynlig (2)**

> *Kommentar:*
>
> Working inside fume hood with good ventilation, appropriate gloves, goggles and labcoat makes the incident not very likely to happen

Konsekvensområde: Helse   *Risiko:*

> *Vurdert konsekvens:* **Liten (1)**
>
> > *Kommentar:* H272 May intensify fire; oxidizing

Konsekvensområde: Materielle verdier   *Risiko:*

> *Vurdert konsekvens:* **Middels (2)**
>
> > *Kommentar:* H272 May intensify fire; oxidizing

Uønsket hendelse: Spill of aluminium nitrate nonahydrate when weighting sample
- -

Sannsynlighet for hendelsen (felles for alle konsekvensområder): **Lite sannsynlig (2)**

> *Kommentar:*
>
> Working inside fume hood with good ventilation, appropriate gloves, goggles and labcoat makes the incident not very likely to happen

Konsekvensområde: Helse   *Risiko:*

> *Vurdert konsekvens:* **Middels (2)**
>
> > *Kommentar:* H272 May intensify fire; Oxidizing.
> > H319 Causes serious eye irritation.
> > H315 Irritating to skin.

Konsekvensområde: Materielle verdier

Vurdert konsekvens: **Middels (2)**

Kommentar: [Ingen registreringer]

Risiko:

Uønsket hendelse: Spill of palladium(II) nitrate dihydrate when weighting sample

Sannsynlighet for hendelsen (felles for alle konsekvensområder): **Lite sannsynlig (2)**

Kommentar:
[Ingen registreringer]

Konsekvensområde: Helse

Vurdert konsekvens: **Middels (2)**

Kommentar: H272 May intensify fire; oxidizing.
H301 Toxic if swallowed.
H314 Causes severe burns to skin and eyes.
H410 Very toxic, with long-term effects, to aquatic life.

Risiko:

Konsekvensområde: Ytre miljø

Vurdert konsekvens: **Liten (1)**

Kommentar: [Ingen registreringer]

Risiko:

Konsekvensområde: Materielle verdier

Vurdert konsekvens: **Middels (2)**

Kommentar: Fire

Risiko:

Norges teknisk-naturvitenskapelige universitet (NTNU)

Unntatt offentlighet jf. Offentlighetsloven § 14

Utskriftsdato:
24.05.2023

Utskrift foretatt av:
Ida Saxrud

Side:
23/44

Uønsket hendelse: Spill of rhodium(III) nitrate hydrate when weighting sample

- -

Sannsynlighet for hendelsen (felles for alle konsekvensområder):   **Lite sannsynlig (2)**

> *Kommentar:*
> [Ingen registreringer]

Konsekvensområde: Helse   *Risiko:*

> *Vurdert konsekvens:* **Middels (2)**

>> *Kommentar:* H272 May intensify fire; oxidizing.
>> H314 Causes severe burns to skin and eyes

Konsekvensområde: Materielle verdier   *Risiko:*

> *Vurdert konsekvens:* **Middels (2)**

>> *Kommentar:* [Ingen registreringer]

Uønsket hendelse: Spill of platinum(IV) nitrate, solution

- -

Sannsynlighet for hendelsen (felles for alle konsekvensområder):   **Lite sannsynlig (2)**

> *Kommentar:*
> [Ingen registreringer]

Konsekvensområde: Helse   *Risiko:*

> *Vurdert konsekvens:* **Stor (3)**

>> *Kommentar:* H290 - May be corrosive to metals
>> H314 - Causes severe burns to skin and eyes
>> H332 - Harmful by inhalation

Konsekvensområde: Materielle verdier

Vurdert konsekvens: **Middels (2)**

Kommentar: [Ingen registreringer]

Risiko:

Farekilde: Waste handling and cleaning

Uønsket hendelse: Acetone for cleaning - spillage

Sannsynlighet for hendelsen (felles for alle konsekvensområder):   **Sannsynlig (3)**

    Kommentar:
    [Ingen registreringer]

Konsekvensområde: Helse   *Risiko:*

    Vurdert konsekvens: **Liten (1)**

        Kommentar: EUH 066 Repeated exposure may cause dry or cracked skin.
                       H225 Highly flammable liquid and vapour.
                       H319 Causes serious eye irritation.
                       H336 May cause drowsiness or dizziness

Konsekvensområde: Ytre miljø   *Risiko:*

    Vurdert konsekvens: **Liten (1)**

        Kommentar: [Ingen registreringer]

Konsekvensområde: Materielle verdier   *Risiko:*

    Vurdert konsekvens: **Liten (1)**

        Kommentar: [Ingen registreringer]

Farekilde: Calcination furnace

Uønsket hendelse: Skin burns
- -

Årsak: Not using heat protective gloves

Sannsynlighet for hendelsen (felles for alle konsekvensområder):   **Lite sannsynlig (2)**

     Kommentar:

     The use of appropriate gloves makes the incident unlikely to happen. Thermal gloves.

Konsekvensområde: Helse   *Risiko:*

   Vurdert konsekvens: **Liten (1)**

      Kommentar: [Ingen registreringer]

Uønsket hendelse: Electric shock
- -

Sannsynlighet for hendelsen (felles for alle konsekvensområder):   **Lite sannsynlig (2)**

     Kommentar:

     [Ingen registreringer]

Konsekvensområde: Helse   *Risiko:*

   Vurdert konsekvens: **Middels (2)**

      Kommentar: [Ingen registreringer]

Konsekvensområde: Ytre miljø   *Risiko:*

   Vurdert konsekvens: **Liten (1)**

      Kommentar: [Ingen registreringer]

Konsekvensområde: Materielle verdier

Risiko:

    Vurdert konsekvens: **Middels (2)**

        Kommentar: [Ingen registreringer]

Uønsket hendelse: Uncontrolled heating

Sannsynlighet for hendelsen (felles for alle konsekvensområder):   **Lite sannsynlig (2)**

    Kommentar:
[Ingen registreringer]

Konsekvensområde: Helse

Risiko:

    Vurdert konsekvens: **Liten (1)**

        Kommentar: [Ingen registreringer]

Konsekvensområde: Ytre miljø

Risiko:

    Vurdert konsekvens: **Liten (1)**

        Kommentar: [Ingen registreringer]

Konsekvensområde: Materielle verdier

Risiko:

    Vurdert konsekvens: **Liten (1)**

        Kommentar: [Ingen registreringer]

Uønsket hendelse: Fire

- -

Sannsynlighet for hendelsen (felles for alle konsekvensområder): **Svært lite sannsynlig (1)**

    Kommentar:
    [Ingen registreringer]

Konsekvensområde: Helse   *Risiko:*

    Vurdert konsekvens: **Middels (2)**

        Kommentar: [Ingen registreringer]

Konsekvensområde: Ytre miljø   *Risiko:*

    Vurdert konsekvens: **Liten (1)**

        Kommentar: [Ingen registreringer]

Konsekvensområde: Materielle verdier   *Risiko:*

    Vurdert konsekvens: **Middels (2)**

        Kommentar: [Ingen registreringer]

Farekilde: Use of compressed gases (He, Ar)

Uønsket hendelse: Uncontrolled expansion and depletion of O2

Sannsynlighet for hendelsen (felles for alle konsekvensområder):   **Lite sannsynlig (2)**

> *Kommentar:*
> [Ingen registreringer]

Konsekvensområde: Helse   *Risiko:*

> *Vurdert konsekvens:* **Middels (2)**
>
> > *Kommentar:* H270 - May cause or intensify fire; oxidizing.
> > H280 - Contains gas under pressure; may explode when heated

Konsekvensområde: Ytre miljø   *Risiko:*

> *Vurdert konsekvens:* **Liten (1)**
>
> > *Kommentar:* [Ingen registreringer]

Konsekvensområde: Materielle verdier   *Risiko:*

> *Vurdert konsekvens:* **Middels (2)**
>
> > *Kommentar:* [Ingen registreringer]

Norges teknisk-naturvitenskapelige universitet (NTNU)	**Utskriftsdato:**	**Utskrift foretatt av:**	**Side:**
Unntatt offentlighet jf. Offentlighetsloven § 14	24.05.2023	Ida Saxrud	30/44

Uønsket hendelse: Gas leakage

- -

Sannsynlighet for hendelsen (felles for alle konsekvensområder):   **Sannsynlig (3)**

   Kommentar:

Have good detection measures as well as good ventilation. Gas detector and leak detection spray will provide info about a possible leak. The ventilation system in the rig ensures low gas concentration if the rig has any leaks.

Konsekvensområde: Helse   *Risiko:*

  Vurdert konsekvens: **Liten (1)**

    Kommentar: H280 Contains gas under pressure; may explode when heated.

Konsekvensområde: Ytre miljø   *Risiko:*

  Vurdert konsekvens: **Middels (2)**

    Kommentar: [Ingen registreringer]

Konsekvensområde: Materielle verdier   *Risiko:*

  Vurdert konsekvens: **Liten (1)**

    Kommentar: [Ingen registreringer]

Farekilde: Use of flammable gases (CH4, H2, CO)

Uønsket hendelse: Fire, explotion

Sannsynlighet for hendelsen (felles for alle konsekvensområder):　　**Svært lite sannsynlig (1)**

　　　　　　Kommentar:

　　　　　　CH4, CO and H2 are all extremely flammable gases. However, there are many gas detection systems and alarms that makes this scenario unlikely. Doing manual leak tests as well as detectors being placed both locally at rig and globally in the lab reduces this risk.

Konsekvensområde: Helse　　　　　　　　　　　　　　　　　　　　　　　　　*Risiko:*

　　　Vurdert konsekvens: **Svært stor (4)**

　　　　　Kommentar: CH4:
　　　　　　　　　　　H220 - Extremely flammable gas.
　　　　　　　　　　　H280 - Contains gas under pressure; may explode when heated

　　　　　　　　　　　H2:
　　　　　　　　　　　H220: Extremely flammable gas.
　　　　　　　　　　　H280: Contains gas under pressure; may explode when heated.

　　　　　　　　　　　CO:
　　　　　　　　　　　H220 Extremely flammable gas.
　　　　　　　　　　　H280 Contains gas under pressure; may explode when heated.
　　　　　　　　　　　H331 Toxic by inhalation.
　　　　　　　　　　　H360D May harm the unborn child.
　　　　　　　　　　　H372 Causes damage to organs through prolonged or repeated exposure

Konsekvensområde: Ytre miljø　　　　　　　　　　　　　　　　　　　　　　*Risiko:*

　　　Vurdert konsekvens: **Middels (2)**

　　　　　Kommentar: [Ingen registreringer]

Konsekvensområde: Materielle verdier　　　　　　　　　　　　　　　　　　　*Risiko:*

　　　Vurdert konsekvens: **Svært stor (4)**

　　　　　Kommentar: [Ingen registreringer]

Konsekvensområde: Omdømme

Risiko:

Vurdert konsekvens: **Stor (3)**

Kommentar: [Ingen registreringer]

Farekilde: N2 physisorption

Uønsket hendelse: Liquid N2 spill

Sannsynlighet for hendelsen (felles for alle konsekvensområder):   **Svært lite sannsynlig (1)**

Kommentar:

Not likely because of personal measures.

Konsekvensområde: Helse   *Risiko:*

Vurdert konsekvens: **Stor (3)**

Kommentar: H281 - Contains refrigerated gas; can cause severe frostbite..

Farekilde: H2 Chemisorption

Uønsket hendelse: Gas leakage

Sannsynlighet for hendelsen (felles for alle konsekvensområder):   **Svært lite sannsynlig (1)**

    Kommentar:

    [Ingen registreringer]

Konsekvensområde: Helse   *Risiko:*

    Vurdert konsekvens: **Middels (2)**

        Kommentar: H220: Extremely flammable gas.
                      H280: Contains gas under pressure; may explode when heated.

Konsekvensområde: Materielle verdier   *Risiko:*

    Vurdert konsekvens: **Middels (2)**

        Kommentar: [Ingen registreringer]

Farekilde: TPR

Uønsket hendelse: Gas leakage

Sannsynlighet for hendelsen (felles for alle konsekvensområder):   **Svært lite sannsynlig (1)**

      Kommentar:

      Gas detectors will detect an eventual leak

Konsekvensområde: Helse   *Risiko:*

      Vurdert konsekvens: **Middels (2)**

        Kommentar: [Ingen registreringer]

Farekilde: Use of toxic gases (CO)

Uønsket hendelse: CO leakage

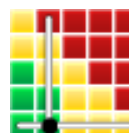*Sannsynlighet for hendelsen (felles for alle konsekvensområder):* **Svært lite sannsynlig (1)**

    Kommentar:

    Gas detectors will detect an eventual leak

Konsekvensområde: Helse   *Risiko:*

    Vurdert konsekvens: **Svært stor (4)**

           Kommentar: H220 Extremely flammable gas.
                            H280 Contains gas under pressure; may explode when heated.
                            H331 Toxic by inhalation.
                            H360D May harm the unborn child.
                            H372 Causes damage to organs through prolonged or repeated exposure

---

Farekilde: Use of Toluene

Uønsket hendelse: Spill of liquid toluene
- -

Sannsynlighet for hendelsen (felles for alle konsekvensområder): **Lite sannsynlig (2)**

      Kommentar:

      Use of labcoat, goggles, gloves and work inside a fumehood.

Konsekvensområde: Helse

Vurdert konsekvens: **Stor (3)**

Kommentar: H225 Highly flammable liquid and moist.
H361d Suspected of causing birth defects.
H304 May be fatal if swallowed if inhaled.
H373 May cause damage to organs through prolonged or repeated exposure.
H315 Irritating to skin.
H336 May cause drowsiness or dizziness.

Risiko:

Farekilde: Use of Fenol

Uønsket hendelse: Spill of Fenol

- -

Sannsynlighet for hendelsen (felles for alle konsekvensområder):　　**Lite sannsynlig (2)**

　　　　Kommentar:

　　　　Use of labcoat, goggles, gloves and work inside fumehood.

Konsekvensområde: Helse　　　　　　　　　　　　　　　　　　　　　　*Risiko:*

　　Vurdert konsekvens: **Svært stor (4)**

　　　Kommentar: H314 - Causes severe burns to skin and eyes
H341 - Suspected of causing genetic damage
H373 - May cause damage to organs through prolonged or repeated exposure
H301 + H311 + H331 - Toxic if swallowed, in contact with skin or if inhaled

---

Norges teknisk-naturvitenskapelige universitet (NTNU)　　　**Utskriftsdato:**　　**Utskrift foretatt av:**　　　　**Side:**

Unntatt offentlighet jf. Offentlighetsloven § 14　　24.05.2023　　Ida Saxrud　　　　39/44

Farekilde: Use of 1-Methylnaphthalene

Uønsket hendelse: Spill of 1-Methylnaphthalene

Sannsynlighet for hendelsen (felles for alle konsekvensområder):   **Lite sannsynlig (2)**

> *Kommentar:*
>
> Use of labcoat, goggles, gloves and work inside a fumehood.

Konsekvensområde: Helse   *Risiko:*

> *Vurdert konsekvens:* **Svært stor (4)**
>
> *Kommentar:* H302 Harmful if swallowed.
> H304 May be fatal if swallowed if inhaled.
> H411 Toxic, with long-term effects, to aquatic life.

Konsekvensområde: Ytre miljø   *Risiko:*

> *Vurdert konsekvens:* **Stor (3)**
>
> *Kommentar:* [Ingen registreringer]

Farekilde: MP-AES

Uønsket hendelse: Spill of HNO3

Sannsynlighet for hendelsen (felles for alle konsekvensområder):　　**Lite sannsynlig (2)**

　　　　Kommentar:
　　　　Use of labcoat, goggles, gloves and work inside a fumehood.

Konsekvensområde: Helse　　　　　　　　　　　　　　　　　*Risiko:*

　　　Vurdert konsekvens:　**Stor (3)**

　　　　　Kommentar:　[Ingen registreringer]

Konsekvensområde: Materielle verdier　　　　　　　　　　*Risiko:*

　　　Vurdert konsekvens:　**Middels (2)**

　　　　　Kommentar:　[Ingen registreringer]

Uønsket hendelse: Spill of HCl

Sannsynlighet for hendelsen (felles for alle konsekvensområder):　　**Lite sannsynlig (2)**

　　　　Kommentar:
　　　　Use of labcoat, goggles, gloves and work inside a fumehood.

Konsekvensområde: Helse　　　　　　　　　　　　　　　　　*Risiko:*

　　　Vurdert konsekvens:　**Stor (3)**

　　　　　Kommentar:　[Ingen registreringer]

Konsekvensområde: Materielle verdier

Vurdert konsekvens: **Middels (2)**

Kommentar: [Ingen registreringer]

Risiko:

Norges teknisk-naturvitenskapelige universitet (NTNU)

Unntatt offentlighet jf. Offentlighetsloven § 14

Utskriftsdato:

24.05.2023

Utskrift foretatt av:

Ida Saxrud

Side:

42/44

Oversikt over besluttede risikoreduserende tiltak:

Under presenteres en oversikt over risikoreduserende tiltak som skal bidra til å reduseres sannsynlighet og/eller konsekvens for uønskede hendelser.

Detaljert oversikt over besluttede risikoreduserende tiltak med beskrivelse:

Detaljert oversikt over vurdert risiko for hver farekilde/uønsket hendelse før og etter besluttede tiltak